U.S. Department of Transportation
National Highway Traffic Safety Administration

NHTSA

DOT HS 812 904

November 2020 (revised)

Occupant Safety in Vehicles Equipped With Automated Driving Systems, Part 1: Initial Evaluation of Usability, Stability, and Injury Prediction Capabilities

DISCLAIMER

This publication is distributed by the U.S. Department of Transportation, National Highway Traffic Safety Administration, in the interest of information exchange. The opinions, findings, and conclusions expressed in this publication are those of the authors and not necessarily those of the Department of Transportation or the National Highway Traffic Safety Administration. The United States Government assumes no liability for its contents or use thereof. If trade or manufacturers' names are mentioned, it is only because they are considered essential to the object of the publication and should not be construed as an endorsement. The United States Government does not endorse products or manufacturers.

NOTE: This report is published in the interest of advancing motor vehicle safety research. While the report may provide results from research or tests using specifically identified motor vehicle models, it is not intended to make conclusions about the safety performance or safety compliance of those motor vehicles, and no such conclusions should be drawn.

Suggested APA Format Citation:

Lin, H., Gepner, B., Wu, T., Forman, J., Shaw, G., & Panzer, M. B. (2020, November (revised)). *Occupant Safety in Vehicles Equipped With Automated Driving Systems, Part 1: Initial Evaluation of Usability, Stability, and Injury Prediction Capabilities* (Report No. DOT HS 812 904). National Highway Traffic Safety Administration.

This report is one of three deliverables under Contract DTNH2215D00004/0002 awarded to the Center for Applied Biomechanics at the University of Virginia, Charlottesville, Virginia. The three are reports are titled as follows.

Occupant Safety in Vehicles Equipped With Automated Driving Systems, Part 1: Initial Evaluation of Usability, Stability, and Injury Prediction Capabilities

Occupant Safety in Vehicles Equipped With Automated Driving Systems, Part 2: Crash Safety Considerations for Out-of-Position Occupant Posture in Vehicles With Automated Driving Systems - Field Data Investigation

Occupant Safety in Vehicles Equipped With Automated Driving Systems, Part 3: Biofidelity Evaluation of GHBMC M50-OS Against Laboratory Sled Tests

The NHTSA citations and DOT HS report numbers for these three reports are as follows.

Lin, H., Gepner, B., Wu, T., Forman, J., Shaw, G., & Panzer, M. B. (2020, November (revised)). *Occupant safety in vehicles equipped with automated driving systems, Part 1: Initial evaluation of usability, stability, and injury prediction capabilities* (Report No. DOT HS 812 904). National Highway Traffic Safety Administration.

Shaw, G., Poplin, J., McMurry, T., Kong, K., Lin, H., & Panzer, M. B. (2020, February). *Occupant safety in vehicles equipped with automated driving systems, Part 2: Crash safety considerations for out-of-position occupant posture in vehicles with automated driving systems - Field data investigation* (Report No. DOT HS 812 883). National Highway Traffic Safety Administration.

Poulard, D., Lin, H., & Panzer, M. B. (2020, July). *Occupant safety in vehicles equipped with automated driving systems, Part 3: Biofidelity evaluation of GHBMC M50-OS against laboratory sled tests* (Report No. DOT HS 812 905). National Highway Traffic Safety Administration.

Technical Report Documentation Page

1. Report No.	2. Government Accession No.	3. Recipient's Catalog No.
DOT HS 812 904		

4. Title and Subtitle	5. Report Date
Occupant Safety in Vehicles Equipped With Automated Driving Systems, Part 1: Initial Evaluation of Usability, Stability, and Injury Prediction Capabilities	November 2020 (revised)
	6. Performing Organization Code
7. Authors	8. Performing Organization Report No.
Hongnan Lin, Bronislaw Gepner, Taotao Wu, Jason Forman, Greg Shaw, Matthew B. Panzer	
9. Performing Organization Name and Address	10. Work Unit No. (TRAIS)
Center for Applied Biomechanics 4040 Lewis and Clark Drive Charlottesville, VA 22911	11. Contract or Grant No. DTNH2215D00004/0002
12. Sponsoring Agency Name and Address	13. Type of Report and Period Covered
National Highway Traffic Safety Administration 1200 New Jersey Avenue SE Washington, DC 20590	Final Report
	14. Sponsoring Agency Code

15. Supplementary Notes
James Saunders was the COR for this project.

16. Abstract
This project sought to perform an initial evaluation of the usability, stability, and potential injury prediction capabilities for two human body models (GHBMC-M50-O and GHBMC-M50-OS) and the NHTSA THOR FE anthropomorphic test device model in occupant postures that will become more possible with automated driving systems (ADS). Postures examined degrees of seat recline, degrees of inboard seat rotation, occupants turned in their seats, and occupants leaning against the belts in sleep-like posture. Collision scenarios included moving deformable barrier impacts at PDOFs around the vehicle. All simulations were performed with the occupant seated in the right front passenger position. Restraints included a front passenger air bag, a side curtain air bag, a side torso air bag, and a 3-point seat belt. Approximately 175 full vehicle simulations were performed and analyzed. The primary lessons learned are: The design of the THOR pelvis constrains the maximum degree effectively reclined; GHBMC M50-O and OS models are too stiff for natural gravity settling into reclined positions; the GHBMC M50-O model required substantial computational effort to position into a reclined posture; the GHBMC M50-OS model exhibited negative volume errors in the abdomen from the belt loading; the GHBMC M50-OS models lacks continuity constraints between superficial tissue, skeleton, and internal organs; the GHBMC M50-OS model tended to be more prone to submarining than the THOR FE model. The models also exhibited differences in pelvis rotation, lumbar spine flexion, interaction with the seat pan, and interaction with the lap belt.

17. Key Words	18. Distribution Statement
driver	Document is available to the public from the National Technical Information Service, www.ntis.gov.

19. Security Classif. (of this report)	20. Security Classif. (of this page)	21. No. of Pages	22. Price
Unclassified	Unclassified	116	

Form DOT F 1700.7 (8-72) Reproduction of completed page authorized

Table of Contents

Executive Summary

This project sought to perform an initial evaluation of the usability, stability, and potential injury prediction capabilities for two human body models (GHBMC-M50-O and GHBMC-M50-OS), also known as anthropomorphic test devices (ATDs), and the NHTSA Test device for Human Occupant Restraint (THOR) finite element (FE) model in occupant postures that will become more possible with automated driving systems (ADS). Postures examined included various degrees of seat recline, various degrees of inboard seat rotation, occupants turned in their seats, and occupants leaning against the belts in a sleep posture. Collision scenarios included 56 km/h moving deformable barrier impacts (with full engagement) at various principal directions of force (PDOFs) around the vehicle. All simulations were performed with the occupants seated in the right front passenger position. Restraints included a front passenger air bag, a side curtain air bag, a side torso air bag, and a 3-point seat belt (with a standard D-ring position, and with a D-ring integrated into the seat back). Outcomes of interest included any observations of the usability of these occupant models in these scenarios (ability to get into these positions, steps necessary to achieve those positions, etc.), observations on the stability of these models in these scenarios, and observations on the stock instrumentation outputs and potential injury prediction capabilities of these models and utility in these scenarios. Though not the specified goal of this project, some summary comparisons of the model responses were also performed to elucidate potential differences in predicted kinematics and restraint interactions.

Approximately 175 full vehicle simulations were performed and analyzed for this project. The primary lessons learned about the occupant models from this study are as follows:

- The design of the THOR pelvis constrains the maximum degree to which it can be effectively reclined (Figure 22).
- The GHBMC M50-O and OS models are generally too stiff to allow for natural gravity settling into reclined positions. They must be forced into those positions via force application in pre-simulation, or through use of a pre-processing positioning tool. The GHBMC M50-O model required a substantial computational effort to position into a reclined posture.
- The GHBMC M50-OS model exhibited negative volume errors in the abdomen from the belt loading. Once these were addressed with a modification of the model, the model exhibited reasonable stability.
- After the noted modifications, the GHBMC M50-OS tended to exhibit greater stability compared to the current version of the NHTSA THOR FE model. Both M50-OS and THOR FE models were more stable than the M50-O model.
- The GHBMC M50-OS models lacks continuity constraints between superficial tissue, skeleton, and internal organs. As a result, the superficial tissue layer can slide over the skeleton resulting in excessive displacement of soft tissue that we do not see in laboratory-controlled post-mortem human subject (PMHS) tests, affecting the interaction with restraint system.
- The GHBMC M50-OS model tended to be more prone to submarining than the THOR FE model. The models also exhibited differences in pelvis rotation, lumbar spine flexion, interaction with the seat pan, and interaction with the lap belt.

1 Introduction

1.1 Automated Driving Systems

One of the most attractive opportunities with automated driving systems is that they will likely substantially reduce the frequency and severity of crashes (Litman, 2016; Hayes, 2011; Fagnant & Kockelman, 2013; Levinson, 2015). As automated driving technology advances and more vehicles equipped with ADSs join the fleet, injury incidence will likely fall. One source projects 1100 lives saved, 200,000 fewer crashes, and a savings from reduced crashes of 18 billion dollars annually, once 10 percent of the fleet are vehicles with ADSs, and that a 90 percent market penetration will result in a 90 percent reduction in crashes and related costs (Fagnant & Kockelman, 2013). Ultimately the number of U.S. road fatalities could be reduced from 33,000 annually to hundreds with full ADS deployment (Levinson, 2015). This echoes Hayes (2011), who indicates that the per occupant mile fatality rate could be reduced by a factor of 100, which would be similar to the rate for air and rail travel.

While there is optimism as to the ultimate safety benefit associated with ADSs, there will likely be a transition period from human-driven to computer-driven vehicles that may bring new, and potentially increased, risks. The transition period toward a fully ADS-equipped vehicle fleet is estimated by one source to be at least 30 years with a 10– to 20 percent ADS-equipped vehicle fleet by 2040 (Litman, 2016).

Therefore, ensuring occupant safety in ADS-equipped vehicles during the transition period will still require investment in occupant protection countermeasures in addition to advances in crash avoidance. Moreover, enhanced occupant protection helps with public acceptance. Some believe that ADS may be held to a higher standard than current vehicles (Fagnant & Kockelman, 2013). Any crashes with ADS-equipped vehicles will likely be more scrutinized than non-ADS crashes. This would mean that even a very limited number of crashes and resulting injuries could slow the adoption of ADS.

1.2 Occupant Protection

Historically, occupant safety research has focused on full frontal impacts to define occupant response, assess injury risk, and develop countermeasures for occupant protection. Recently, research efforts have focused on oblique frontal collisions to better understand the occupant response and countermeasure efficacy for some of the most frequent real-world crash modes. To protect occupants in these types of crash modes, current restraint systems and safety evaluation tools have considered one primary factor that has remained consistent over nearly a 70-year developmental history and supported by decades of research – the general position of the occupants. ADSs have an opportunity to disrupt this trend by allowing occupant positions not constrained by the need to control the vehicle. A change in occupant position comes with uncertainty in the interaction between the occupant, the restraints, and vehicle interior.

ADS-equipped vehicle occupant protection considerations, while similar to those of current vehicles, will need to include safety countermeasures that accommodate occupants who are out-of-position (OOP) relative to the seat and/or occupant restraint systems due to ADS crash avoidance maneuvers (Battaglia et al., 2013) or due to alternative riding postures. Because the majority of current occupant restraint systems have been developed for occupants that assume

the in-position (IP) posture (Dissanaike et al. 2008), there is concern that current systems will be less effective for ADS occupants in OOP postures. As ADS-equipped vehicle riders become more confident in the safety provided by automated driving, they will be more likely to relax, read, interact with other occupants, and sleep - behavior currently enjoyed by passengers (Hayes, 2011).

1.3 Human Body Models

Human body models (HBM) offer some promising advantages as advanced injury prediction tools to investigate the biomechanical response of the human body in these crash conditions. However, current state-of-the-art HBMs, such as the Global Human Body Model Consortium (GHBMC) 50th percentile detailed male occupant model (M50-O) are limited to validation cases based on the existing set of post-mortem human surrogate (PMHS) whole-body sled or vehicle tests. The validation cases for occupant HBMs include laboratory sled tests in frontal, oblique, and side impact cases; They have not been validated in a reclined position, in a high-speed rear impact condition, or in any other innovative seating configuration proposed for ADS occupants.

Since HBMs were designed and developed primarily with the knowledge of occupant biomechanics in a frontal crash, it is uncertain how biofidelic or stable these models will be in non-standard seating configurations. Based on our field data analysis, reclined occupants have a higher risk of submarining in a frontal crash than an upright occupant, and it is uncertain how well HBMs will be able to model this phenomenon. Furthermore, altering the HBM posture and position continues to be a technical challenge, but will be a necessary step when attempting to use the current HBMs in a non-standard configuration.

1.4 Objective

This project accomplishes three goals: (1) an initial look at how restraint interactions may be affected by occupant and seat positions that may be possible with ADS; (2) an examination of injury patterns that may be expected to occur in ADS occupants in what would currently be considered OOP scenarios; and (3) an evaluation of the utility and limitations of current occupant injury prediction tools (dummy and human body models) in evaluating injury risk in non-standard seating positions. Objectives 1 and 2 were addressed in a previous report.

This report focuses on objective 3, and documents the development of a multi-modal crash study using the GHBMC detailed and simplified 50th percentile male models, and the NHTSA THOR finite element (FE) model. Nearly 200 full vehicle simulations were completed to study the GHBMC and THOR models in various configurations, including reclined seating, rotated seating, and standard or integrated seat belt. From this work, we determined (1) the technical limitations of the existing occupant models, and (2) the estimated occupant responses for ADS-equipped vehicle seating for future automotive safety research and restraint design.

2 Automated Driving Systems Restraints Evaluation Plan

Based on the observations made during the early phase of the project, an ADS Restraints Evaluation Plan was developed and designed to (1) investigate the potential utility and limitations of the chosen human body and ATD models in non-standard posture, restraint, and seat conditions that may be possible with ADS-equipped vehicles, over a range of collision conditions; and (2) to investigate potential occupant restraint and injury issues that may arise in these new restraint, posture, and seat conditions, compared to the typical contemporary vehicle environment. This plan outlined a simulation matrix for a parametric study that included occupant positions spanning those identified in the real-world analysis of OOP drivers, with the addition of additional postures and seat configurations expected to be possible with ADS. The plan was divided into five studies totaling 205 full vehicle simulations.

It was decided to use the 56 km/h impact with the research moving deformable barrier (RMDB) as a setup for the simulation matrix since the stability of the model was confirmed during the preliminary phase. Parameters that were investigated for the three models (THOR FE, M50-OS, and M50) included the following:

Seat Orientation Angle
- Forward-facing (0□), inward-facing (30□ and 135□), lateral-facing (90□), rear-facing (180□)
- Potential limitations: seat anchoring, restraint anchoring, occupant interference

Seat Recline Angle
- Standard position (25□), partially reclined (45□), fully reclined (60□)
- Potential limitations: seat interference, occupant positioning, restraint engagement

Occupant Posture
- Standard position, “Sleeping over the belt,” turned in conversation
- Potential limitations: occupant positioning, restraint engagement, mesh quality

Impact Crash Angle
- Forward (0□), Rear (180□), Lateral (90□, 270□), Oblique (30□, 150□, 210□, 330□)

Countermeasure Variations
- Integrated seat belt

The evaluation plan was designed to target specific research questions that were judged to be the most relevant for ADS-equipped vehicle occupants and associated research questions. The following sections describe the simulation matrix for the ADS restraints evaluation plan. Details on the methods are described in Section 4.

2.1 Study A: Effects of Reclining the Seat

This task is a multi-modal study primarily looking at seat back angle as a factor in occupant response. Occupant response between standard shoulder belt D-ring positions versus seat-integrated shoulder belt were also studied. Both the simplified GHBMC model (M50-0S) and the THOR FE model were run with all of the parameters. It was expected that the THOR model will not be able to run in the fully reclined posture. Additionally, the maximum level of seat recline achieved for the THOR FE model was 40°. The numbers listed below each heading indicate the number of parameter levels in the study. The detailed GHBMC (M50-0) was run at the end of the study using only the frontal impact condition to verify the simplified model results.

Table 1. Reclined seating simulation matrix

Models	Seat Reclined Angle	Seat Orientation	Crash Angle	Common Countermeasures	Variable Countermeasures	Number of Simulations
THOR	25□ 40□	Forward	0° 30° 90° 150° 180° 210° 270° 330°	Pre-tensioner/Load limiter Front passenger air bag Side air bag Curtain air bag	Standard D-Ring integrated shoulder belt	32
M50-OS	25° 45° 60°					48
M50-O	25° 45° 60°	Forward	0°	Pre-tensioner/Load limiter Front passenger air bag Side air bag Curtain air bag	Standard D-Ring integrated shoulder belt	6

Note: 25□ seatback recline is considered "normal" occupant posture.

2.2 Study B: Effects of Seat Orientation

This task is a multi-modal study primarily looking at seat orientation within the vehicle. The seat orientation considered were front-facing (standard), turned 30° inboard, turned 90° inboard (lateral), turned 135° inboard, and turned 180° inboard (rearward, or living-room seating). The integrated shoulder belt with the 25° seat back angle was used for all simulations. The detailed GHBMC was run at the end of the study using only the frontal impact condition to verify the simplified model results.

Table 2. Rotated seating simulation matrix

Models	Seat Reclined Angle	Seat Orientation	Crash Angle	Common Countermeasures	Number of Simulations
THOR M50-OS	25°	Forward 30° inboard Lateral 135° inboard Rearward	0° 30° 90° 150° 180° 210° 270° 330°	Pre-tensioner/Load limiter Integrated shoulder belt Front passenger air bag Side air bag Curtain air bag	80
M50-O	25°	Forward 30° inboard Lateral 135° inboard Rearward	0°	Pre-tensioner/Load limiter Integrated shoulder belt Front passenger air bag Side air bag Curtain air bag	5

2.3 Study C: Effects of a Turned Occupant

This task is a multi-modal study primarily looking at occupant response when the torso is turned inboard. This study assessed frontal and frontal-oblique crash conditions, with a 25° seatback recline seating posture.

Table 3. Turned occupant simulation matrix

Models	Seat Reclined Angle	Seat Orientation	Crash Angle	Common Countermeasures	Variable Postures	Number of Simulations
M50-OS	25°	Forward	0° 30° 330°	Pre-tensioner/Load limiter Standard D-Ring Front passenger air bag Side air bag Curtain air bag	Standard sitting Torso turned 30°	6

2.4 Study D: Effects of Having an Occupant Sleeping on the Belt Path

This task is a study primarily looking at the potential risk for an occupant who is sleeping in the seat and leaning outboard where the shoulder belt routes between the head and shoulder. Crash modes investigated in this study included frontal, near-side oblique, and near-side side impact. Seat back angles included all three reclined positions. The detailed GHBMC was run at the end of the study using only the 25^0 seatback recline angle configuration to verify the simplified model results.

Table 4. Leaning occupant seating simulation matrix

Models	Seat Reclined Angle	Seat Orientation	Crash Angle	Common Countermeasures	Variable Reclined Postures	Number of Simulations
M50-OS	25° 45° 60°	Forward	0° 270° 330°	Pre-tensioner/Load limiter Integrated belt Front passenger air bag Side air bag Curtain air bag	Standard Leaning outboard	18

2.5 Study E: Effects of Occupant Seated Far Back From the Instrument Panel

This task is a study primarily looking at the potential risk for an occupant who is seated far back from the instrument panel such that no frontal air bag is necessary for preventing occupant impact with the instrument panel. This was a scenario brought to our attention by an ADS-equipped vehicle manufacturer who said that passengers responded favorably to a large space between them and the IP. Crash modes investigated in this study included frontal, near-side, and far-side oblique. The seat back angle was 25^0, and no frontal air bag was used.

Table 5. Leaning seated back from instrument panel simulation matrix

Models	Seat Reclined Angle	Seat Orientation	Crash Angle	Common Countermeasures	Number of Simulations
THOR M50-OS M50-O	25°	Forward (set back)	0° 30° 330°	Pre-tensioner Load limiter Integrated belt Side air bag Curtain air bag	9

3 Model Descriptions

3.1 Vehicle

A recently developed FE model of a 2012 Toyota Camry was used as a vehicle platform for this study (Reicher et al., 2016). This is a publicly available model developed by the Center for Collision Safety and Analysis team at George Mason University. The model consists of 2.25M finite elements, and it has gone through a thorough validation process using test results of 10 different full vehicle crash tests.

The selected vehicle FE model was developed in the tons, mm, N and sec unit system (LS-Dyna unit set [b]). This unit system was used throughout the project and all other models used were transformed into this unit set using "*Include Transform" keyword.

3.1.1 Vehicle stability

First, stability runs were performed to identify any potential modeling issues (early termination, contact failure, element instability, etc.) related to the Toyota Camry 2012 FE model that may affect the execution of the parametric study. A stability run was performed using a 56 km/h full frontal impact into a rigid wall (Federal Motor Vehicle Safety Standard [FMVSS] No. 208, Occupant crash protection) (**Figure 1**). No human body model or dummy model was included. Simulation energy as well as added mass to the model resulting from mass scaling were monitored during the simulation. The simulation was hosted on 2 nodes on the UVA Center for Applied Biomechanics (CAB) computational cluster (Dual Opteron 6238, 12 cores/node, 64 GB/node). The simulation normally terminated at 120ms simulation time with an elapsed time of 19 hours on the cluster. Total hourglass energy in the model was smaller than 5 percent (**Figure 2**) of the maximum total energy for the model. No spikes in kinetic energy, internal energy, sliding interface energy, or hourglass energy were observed. Vehicle deformation after impact (**Figure 3**) was similar to what was previously published in the literature (Reicher et al., 2016).

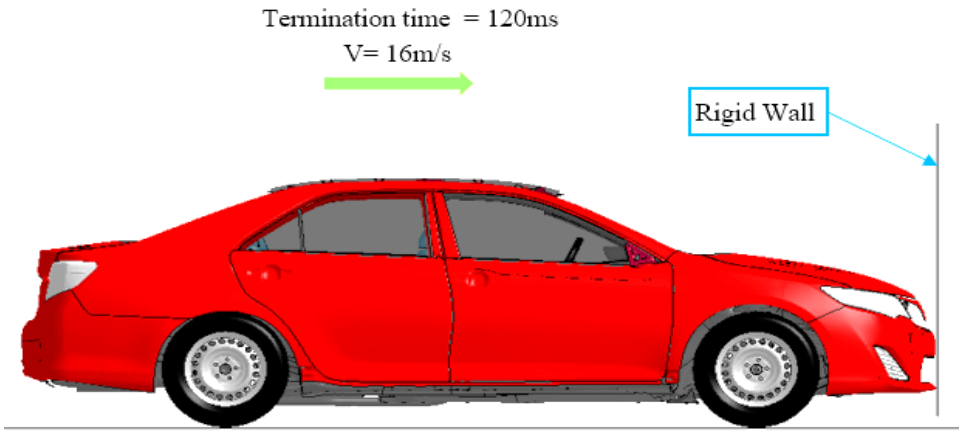

Figure 1. Stability run setup with 2012 Toyota Camry vehicle model.

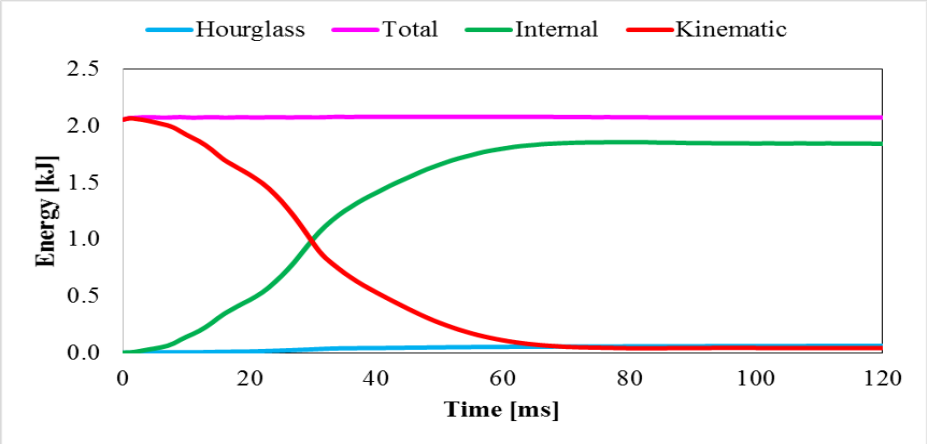

Figure 2. Simulation energies from stability runs.

a)

b)

Figure 3. 56 km/h NCAP deformation obtained in the stability run (a) compared to literature (b).

3.1.2 Vehicle modification

Several modifications were implemented in the Toyota Camry FE model to make it suitable for the proposed parametric study as an ADS. Both the driver seat and rear seats were removed from the model to accommodate variations in sitting posture and seat orientation outlined in the simulation matrix. The tunnel contour interfered with occupant lower extremities with several seat rotations. To maintain the original vehicle structural integrity, the center tunnel was not removed from the vehicle model. However, in several occupant positions, there was interference between the occupant and the center tunnel. To solve the issue, we removed the center tunnel from the part set that was used to define the vehicle-occupant contact. To fill the gap left by the eliminated tunnel contact, a flat panel of null shells was created for contact modeling. This newly implemented null part was added to the part set for the vehicle-occupant contact definition (**Figure 4**).

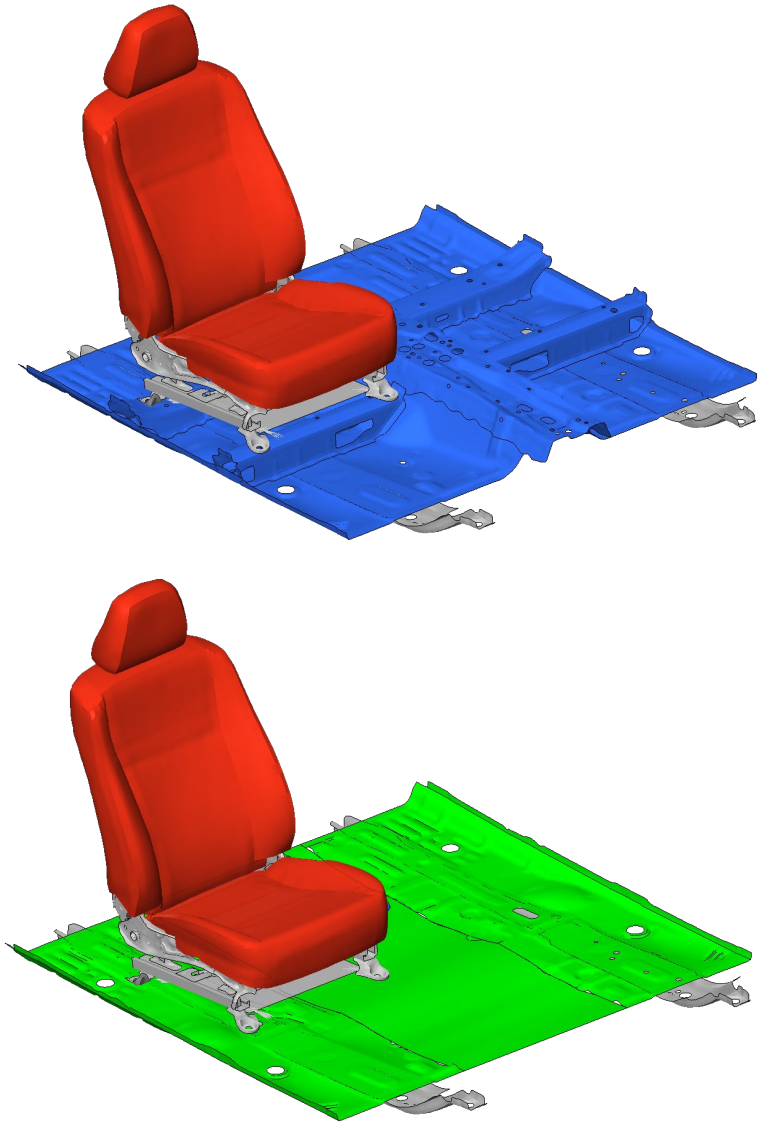

Figure 4. Vehicle floor before (top) and after (bottom) modification.

3.1.3 Development of a parametric seat

A methodology for seat recline was developed to investigate its effect. Reclining the seat was performed by rotating the seatback as described in Figure 5. Based on the results from the crash investigation review (**Figure 5**), we defined three reclined seating configurations: 25^0 (Upright), 45^0 (Semi-reclined) and 60^0 (Fully reclined). Stability runs without human surrogates confirmed that this modification didn't affect the stability.

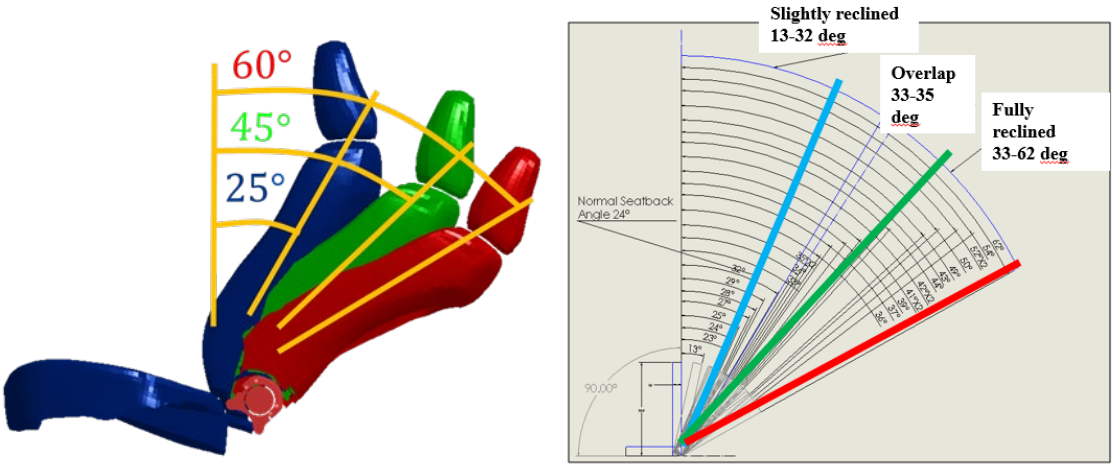

Figure 5. Seatback recline angles.

Seat orientation was one of the parameters proposed in the simulation matrix (Table 2). The seat rotation axis was created at the center position (Node ID: 4082277) on the seat cushion (**Figure 6**). Since the seat penetrated the vehicle structure when rotated clockwise 90°, for this orientation the seat was moved 200mm along the Y axis towards the center console (**Figure 7**). The center console was removed to prevent seat interference. Additionally, it was necessary to remove the driver seat, steering wheel, and rear seat.

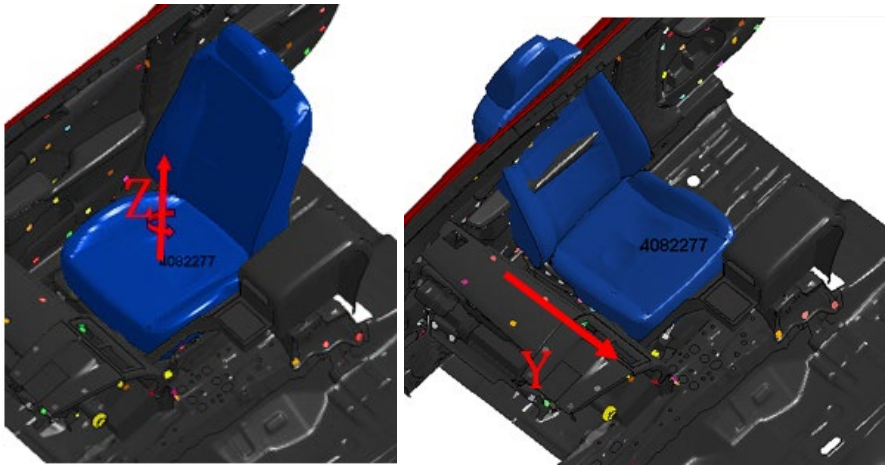

Figure 6. Rotation of the seat cushion (left) followed by translation in-board to avoid penetration with vehicle body (right).

Figure 7. Passenger seat in the 90-degree orientation after positioning.

Considering all of the proposed seat geometries and orientations, it was decided to develop a generic, easily adjustable model of the vehicle seat connection. To achieve it the seat was separated from the vehicle floor and connected through a set of embedded constrained rigid bodies. The "* INCLUDE_TRANSFORM" keyword was used to integrate the desired seat orientation with the vehicle.

3.2 Restraints

3.2.1 Air bags

Three air bag FE models were obtained from a restraint system supplier and were integrated into the Toyota Camry FE model. These air bag models were not associated with the 2012 Toyota Camry vehicle, but represented the restraint systems consistent with this class of vehicle. The air bag models included a passenger frontal air bag, passenger side air bag, and a passenger side curtain air bag, and were integrated into the vehicle model (**Figure 8**). Curtain and side air bags were set to deploy upon impact of the RMDB, and the passenger air bag was deployed 8ms after impact in all simulated crash scenarios.

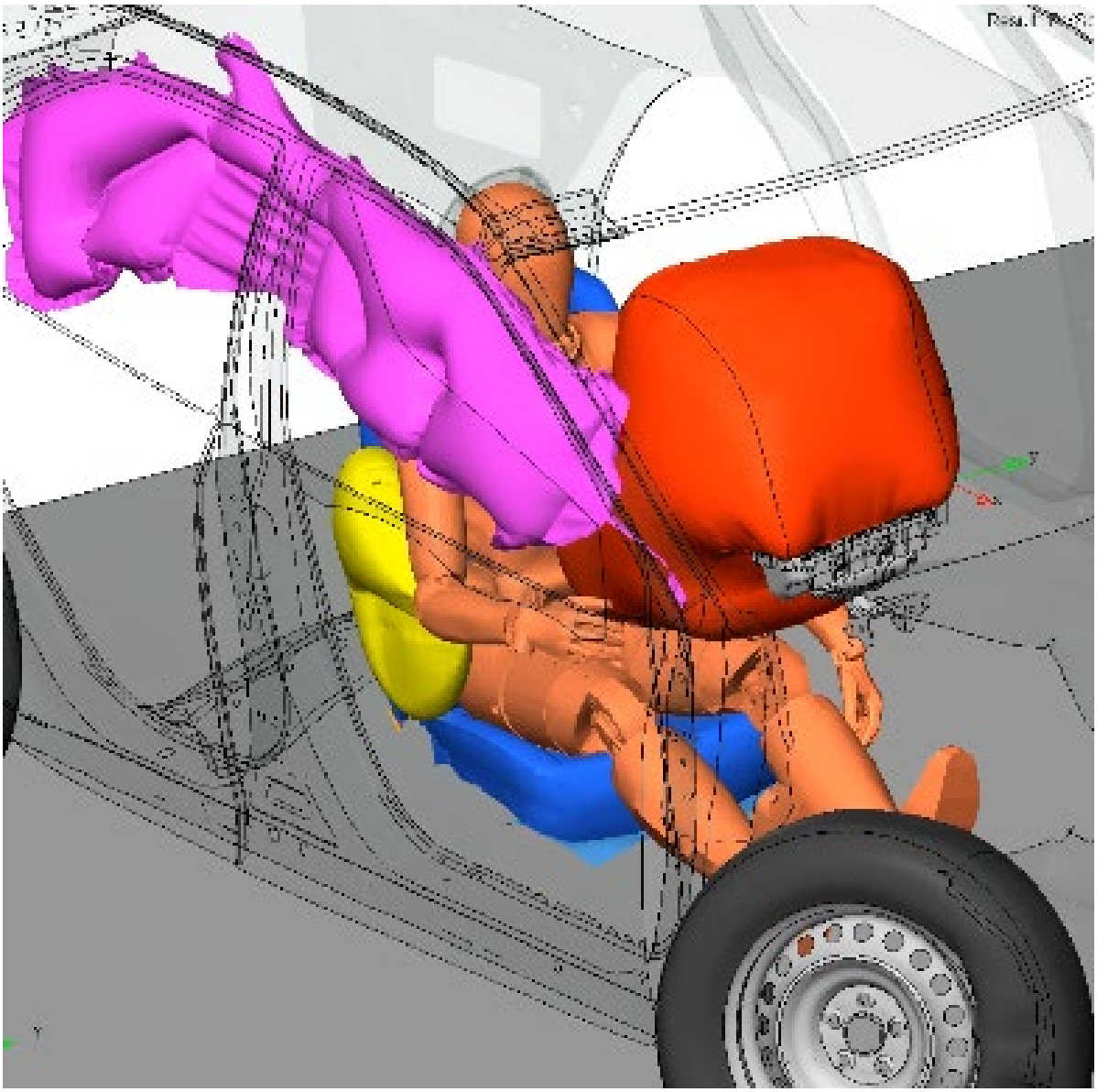

Figure 8. Air bags integration.

3.2.2 Standard seat belt

The standard seat belt restraint used in the Toyota Camry model was based on the belt provided in the NHTSA Toyota Yaris FE model. The belt model included shell belt webbing, a model of a retractor with pyrotechnical pretensioner (300mm stroke and 3 kN load limit), a 3 kN load limiter, and a D-ring in mid-track position.

3.2.3 Integrated seat belt

To accommodate all of the proposed seat positions, a seatback integrated seat belt was developed. The pretensioner, retractor and D-ring were attached to the seatback and moved with it during seatback recline and seat rotations. Since the integrated seat belt put a substantial load onto the seat, a seat reinforcement structure was introduced. To design a realistic reinforced seat,

the requirements of the FMVSS 210, Laboratory Test Procedure - Seat Belt Assembly Anchorages, were followed as a design guideline.

FMVSS 210 requires that both torso and pelvic portions of a type two seat belt assembly shall be loaded to 13.5kN (3,000 lbs) through separate shoulder and lap belt body blocks (**Figure 9**). Additionally, in the case of an integrated seat belt, an additional load is prescribed to the seat structure equal to the mass of the seat multiplied by a 20g acceleration pulse, as stipulated by FMVSS No. 207, Seating systems. The combined FMVSS 210 and 207 procedure also requires an addition of the bracing element between the seat base and the seat back for the tests. In this case this effort was omitted and the load application method loading levels defined in the referenced FMVSSs were used as a guideline for developing the seat model that didn't significantly deform under these loads.

Figure 10 shows the stock Toyota Camry seat with an integrated seat belt subjected to the FMVSS No. 210 loads (including additional 20g load). Load states of 0%, 25%, 50%, and 100% of the required regulatory loads as shown in a figure. Since the seat was never designed to support the occupant restraint system, the seat back exhibited a large amount of deformation. Consequently, a reinforcement structure was developed and integrated with the stock Toyota Camry seat. Beam elements were embedded into the shell structure of the seat frame to provide an additional support and alternative load path (**Figure 11**). Figure 12 shows the reinforced seat with an integrated seat belt subjected to the FMVSS 210 loads. Load states of 0%, 25%, 50%, and 100% of the required regulatory loads were applied as shown in **Figure 12**. The reinforced seat carried all of the required load with a very small deformation (less than 4 inches). The evaluated reinforcement beam structure was added to all of the test conditions with an integrated seat belt in the ADS evaluation plan.

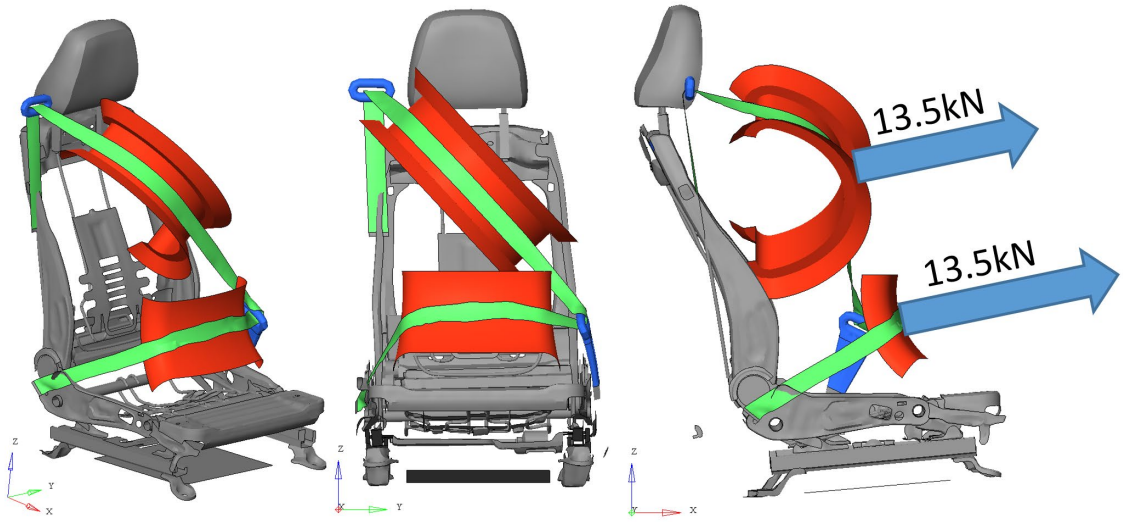

Figure 9. FMVSS 210 simulation test setup for integrated seat belt.

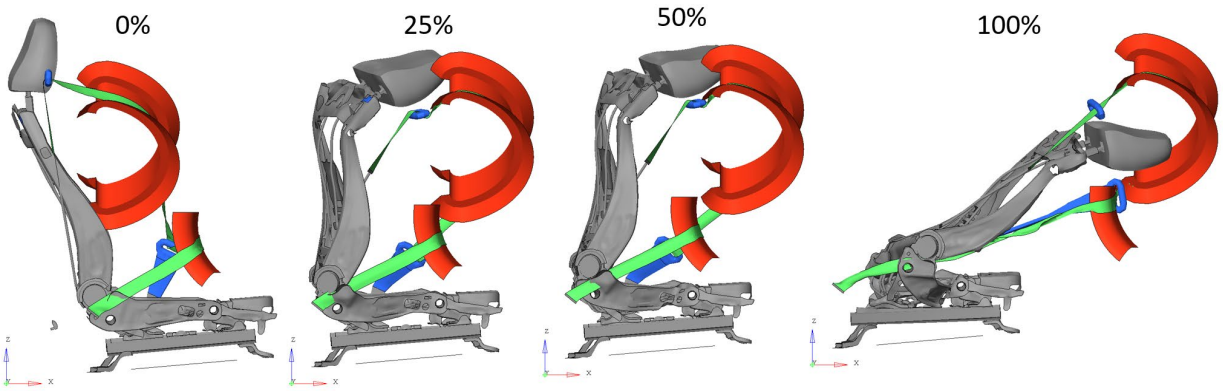

Figure 10. Stock seat with integrated seat belt. Load states of 0%, 25%, 50%, and 100% during the simulated FMVSS 210 test.

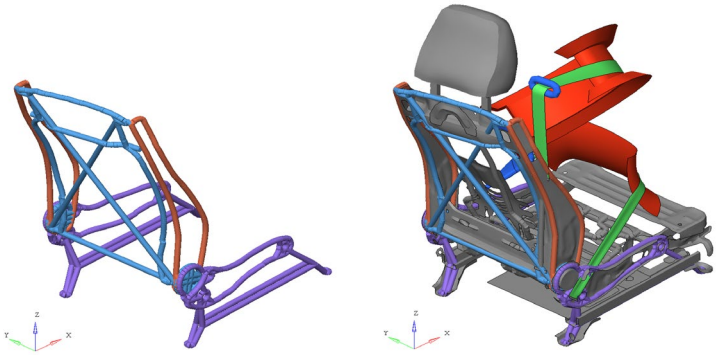

Figure 11. Beam reinforcement structure (left), stock seat with an integrated reinforcement structure (right).

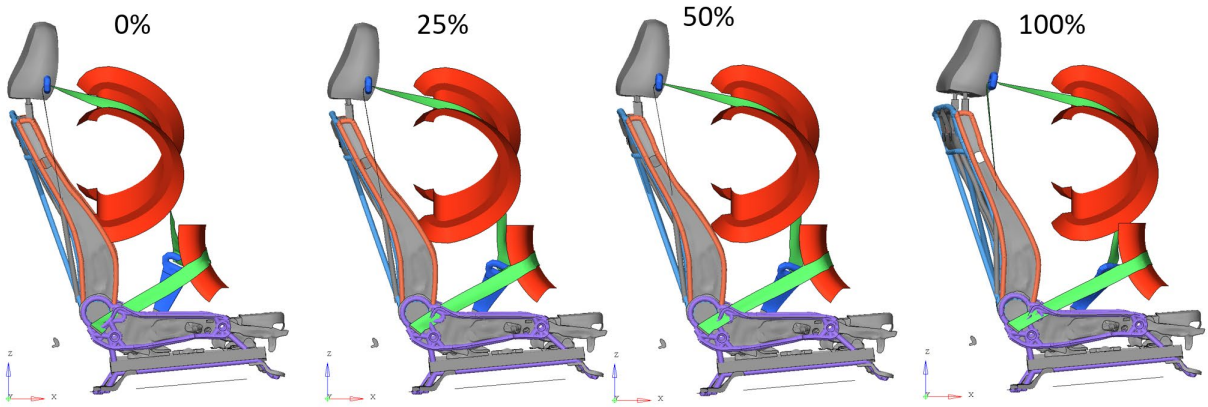

Figure 12. Reinforced seat with integrated seat belt. Load states of 0%, 25%, 50%, and 100% during the simulated FMVSS 210 test.

3.3 Simplified Vehicle Subsystem

Using the interior geometry of the Toyota Camry, a subsystem FE model was developed by rigidizing all components of the vehicle except those associated with the occupant compartment,

seat, and restraint system. A generic acceleration pulse was used to drive the subsystem and load the occupant restraints. The vehicle subsystem was developed to increase the efficiency of the initial development and stability check simulations for several different stages of the model development including implementation and interactions among occupant compartment, restraint system and passenger FE models **(Figure 13**). This approach allowed for a faster (46% speedup) turnaround time between intermediate development simulations when compared with the full vehicle model.

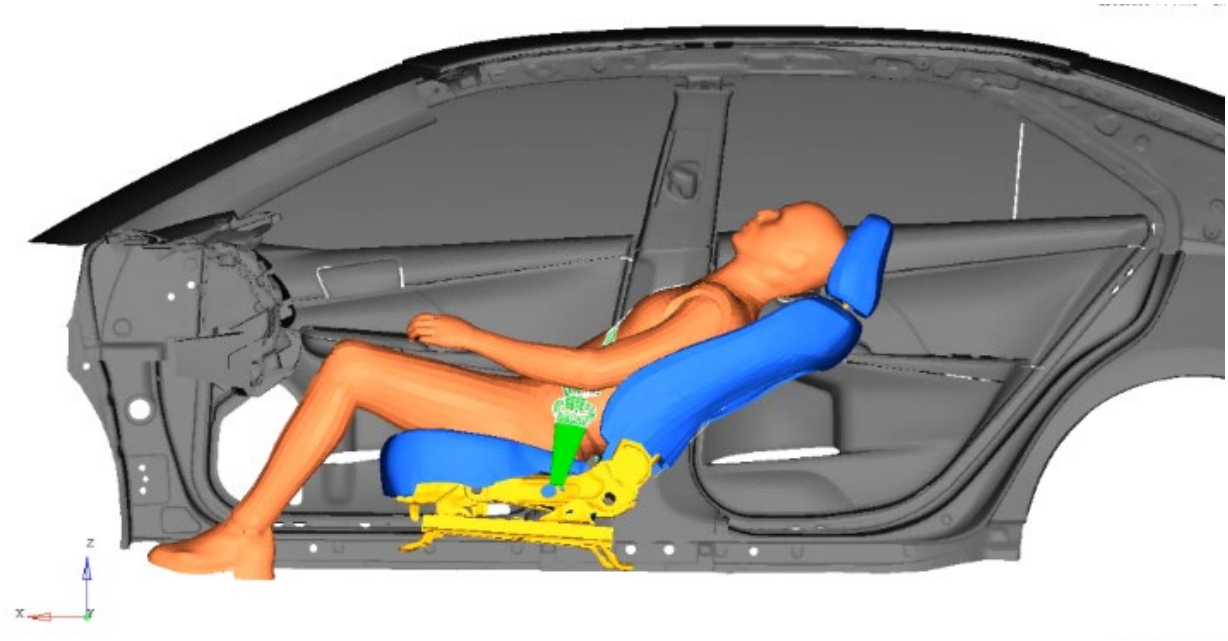

Figure 13. Simplified vehicle subsystem model. Grey components are rigid.

3.4 Research Moving Deformable Barrier

Crash simulations were performed using the Research RMDB model (**Figure 14**) originally designed for oblique and small overlap testing (Saunders et al., 2011). The RMDB was chosen because it was easy to parameterize for multiple impact scenarios to the Toyota Camry model. Although a stability simulation was successfully performed on the Toyota Camry model up to 100 ms for a 56 km/h full frontal impact into a rigid wall (**Figure 1**), we observed better simulation stability using the RMDB, with successul simulations up to 150 ms in the frontal conditon (**Figure 15**). Adding the RMDB resulted in an increase of simulation cost by 25 percent over the rigid wall condition.

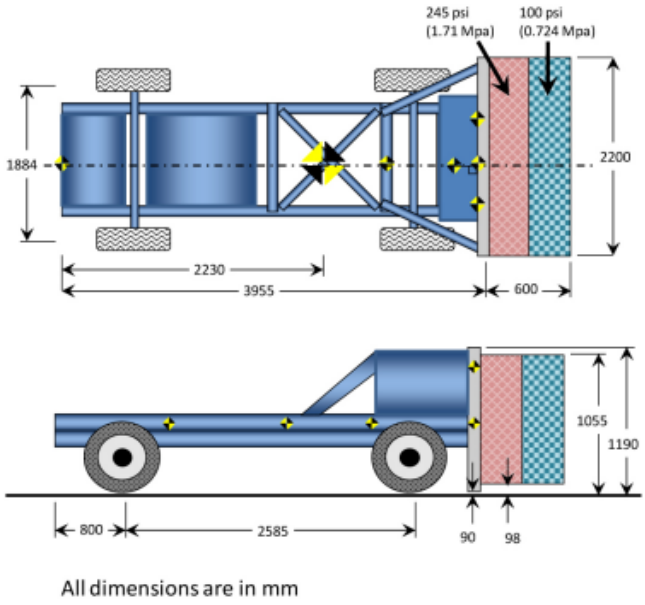

Figure 14. Dimensions of the research moving deformable barrier.

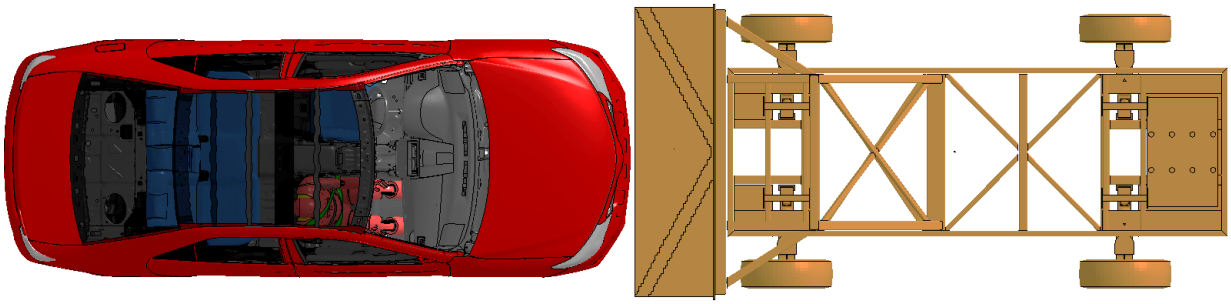

Figure 15. The 56 km/h stability simulation ran successully with THOR and the RMDB.

Finally, eight crash simulations were conducted to explore the response of the vehicle with the modified flat floor panel. All the simulations involved the RMDB impacting the Toyota Camry at 56km/h (**Figure 16**). The RMDB struck the Toyota Camry at 0°, 30°, 90°, 150°, 180°, 210°, 270°, and 330°. All the models were stable with normal termination at t =150ms except for cases of 0° and 330° impact. Modifications were made to the RMDB model to improve the stability in these crash modes such that all simulations without occupant terminated normally.

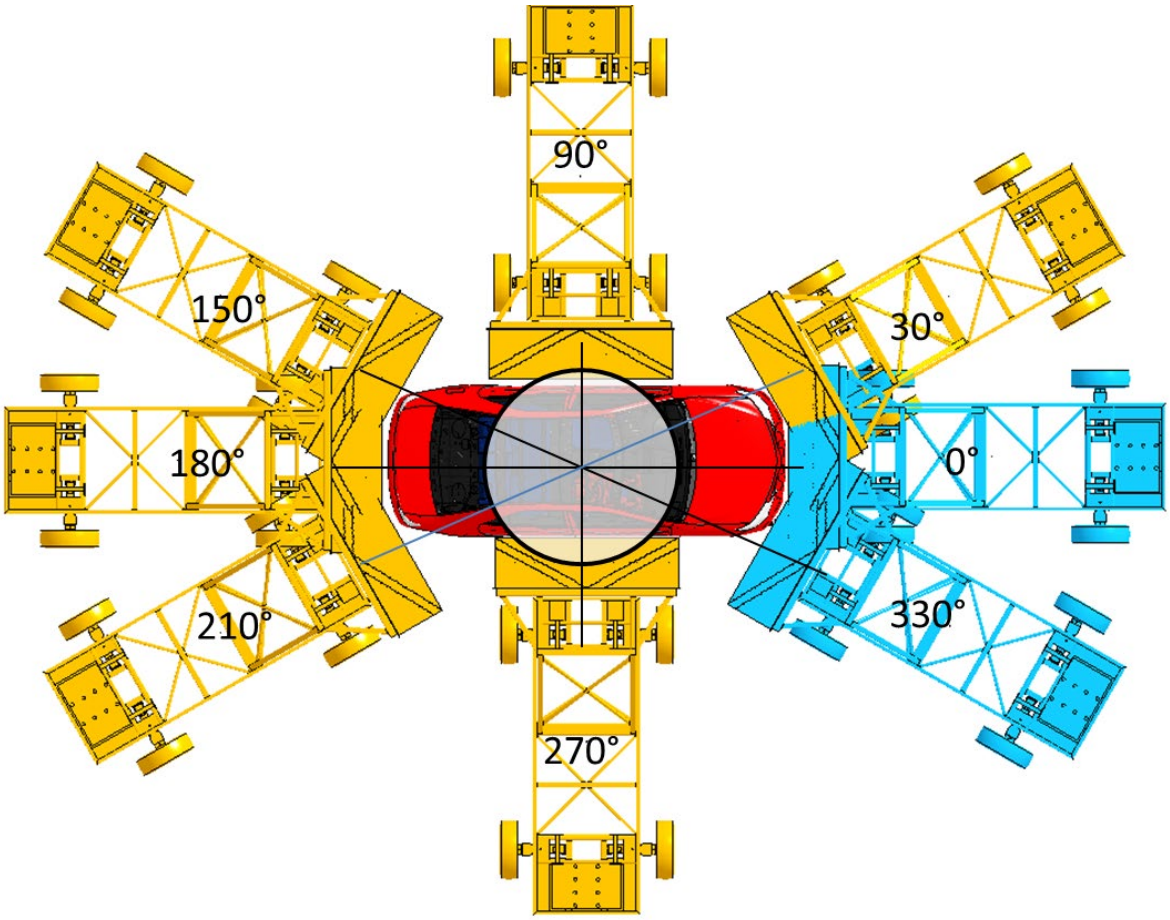

Figure 16. Impact angles with RMDB. Initial unstable simulations are indicated in blue.

3.5 Occupant Models

For each occupant model, there's a corresponding manual to provide the information necessary for a user to implement the FE model in crash simulations.

3.5.1 NHTSA 50th percentile male THOR FE model

The THOR is an advanced anthropomorphic test device considered to be the state-of-the-art for crash test dummies in frontal and oblique crash conditions. The current design of the THOR incorporates advanced sensors and instrumentation that output over 100 channels of data that allow for injury risk assessment. In congruence with the development of the dummy, an FE computational model of the THOR 50th percentile male has been developed and integrated through the collaboration between several institutions (**Figure 17**).

The THOR FE model has been developed and evaluated using the solver LS-DYNA. Before starting to use the model, it's better to learn the unit system, integration, model organization, how to position the occupant, and model outputs through the manual (Panzer, 2015)

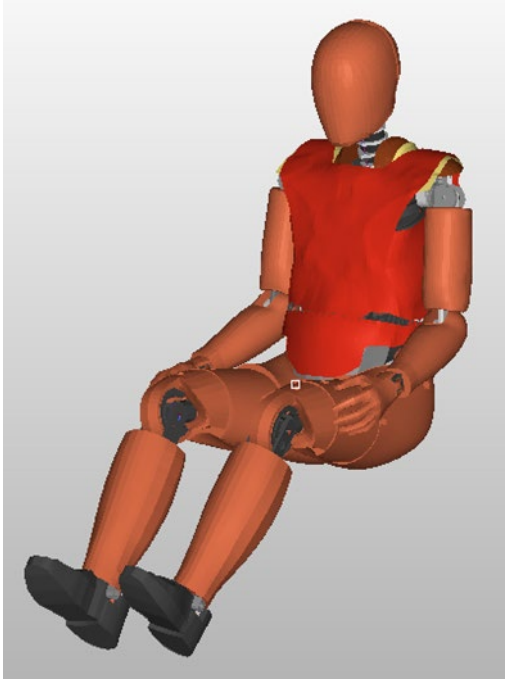

Figure 17. NHTSA THOR FE model version 2.1.

3.5.2 GHBMC 50th percentile male simplified occupant model

The GHBMC is a consortium of seven automakers and one supplier that have consolidated their individual research and development activities in human body modeling into a single global effort to advance crash safety technology. Chrysler Group LLC, General Motors Co., Honda R&D Co., Hyundai Motor Co., Nissan Motor Corp. Ltd., PSA Peugeot-Citroën, Renault S.A., and Takata Corp. are all members of the GHBMC. NHTSA supports GHBMC activities through a cooperative agreement.

The GHBMC 50th percentile male occupant, simplified full body model, M50-OS, is a derivative model from the more detailed variant designed to be computationally efficient for large parametric studies (**Figure 18**). Most of the biomechanics of the M50-OS model have been reduced in complexity, and whole-body response is largely driven by the model acting as a multibody model. Because of this, tissue-level injury prediction is not applicable to the M50-OS; instead, the M50-OS model is used similarly to a dummy, taking forces, moments, and accelerations from digitally instrumented sensors on the model to calculate injury risk. The M50-OS model used in this study was version 1.8.3.

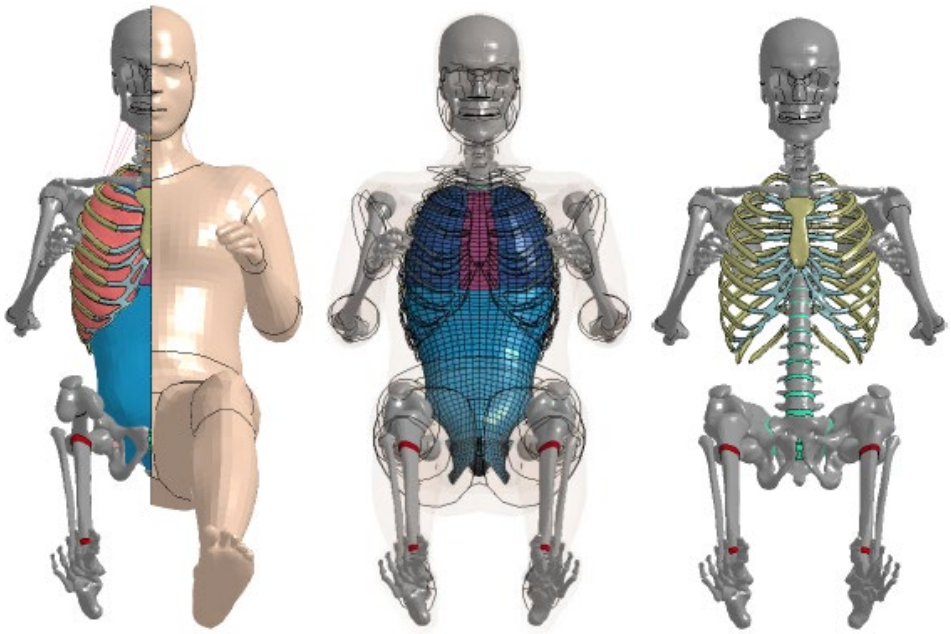

Figure 18. The GHBMC M50-OS occupant model.

3.5.3 GHBMC 50th percentile male detailed occupant model

The GHBMC 50th percentile male occupant, detailed full body model, M50-O, is a more refined model than the M50-OS, and contains a mesh resolution approximately twice as refined as the simplified model (**Figure 19**). The M50-O model was designed to predict injuries to the occupant based on tissue-level failure criterion rather than injury risk functions. The model version used in this study was version 4.4.

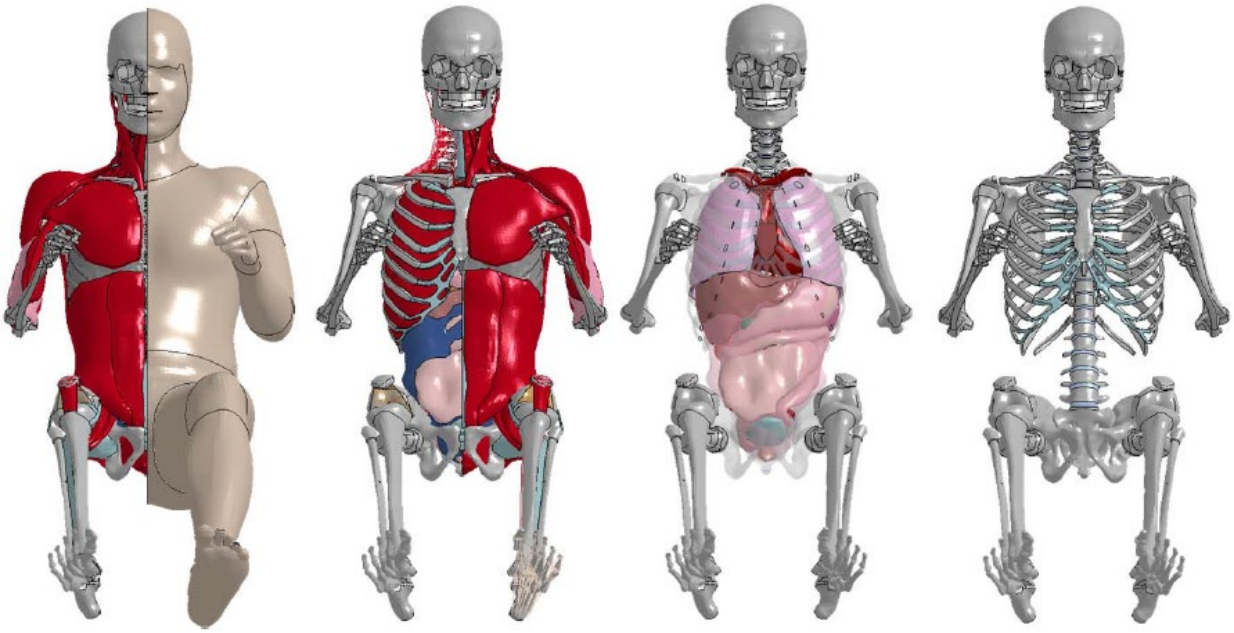

Figure 19. The GHBMC M50-O occupant model.

4 Occupant Integration and Positioning

4.1 THOR

4.1.1 Integration challenges

There were no extraneous challenges integrating the THOR FE model into the vehicle FE model.

4.1.2 Units

Due to different unit systems between the THOR FE model and the vehicle model, THOR was converted to tonne, millimeter, and second using the *INCLUDE_TRANSFORM keyword.

4.1.3 Seating

The instrumented NHTSA THOR FE model was integrated into the FE vehicle model and qualitatively positioned (**Figure 20**). Settlement was performed without any pre-simulation by adding penetration with the seat in conjunction with LS-Prepost "Seat Deformer" (**Figure 21**).

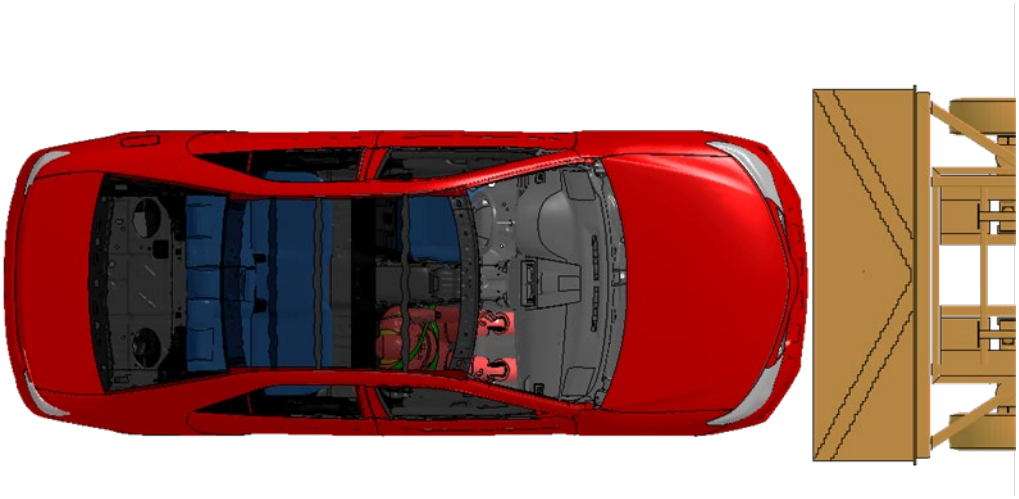

Figure 20. 56 km/h stability setup with THOR.

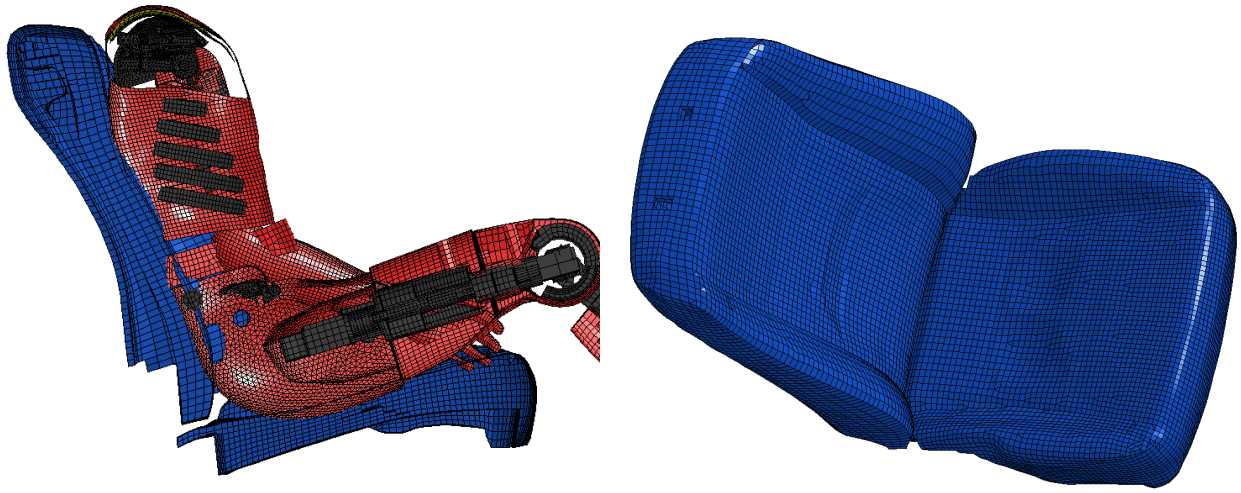

Figure 21. THOR dummy settling using the seat deformer tool included in LS-Prepost.

4.1.4 Positioning

THOR was positioned in the reclined seat using the occupant positioning tree defined in the model. An occupant position tree was used to modify the dummy's joint positions in LS-PrePost. The model was not able to be positioned in the 45˚ position (and 60˚ by extension) without losing the contact with floor (**Figure 22**). It was estimated that the maximum seat recline angle that can be achieved with the THOR FE model is 40˚ (**Figure 22**).

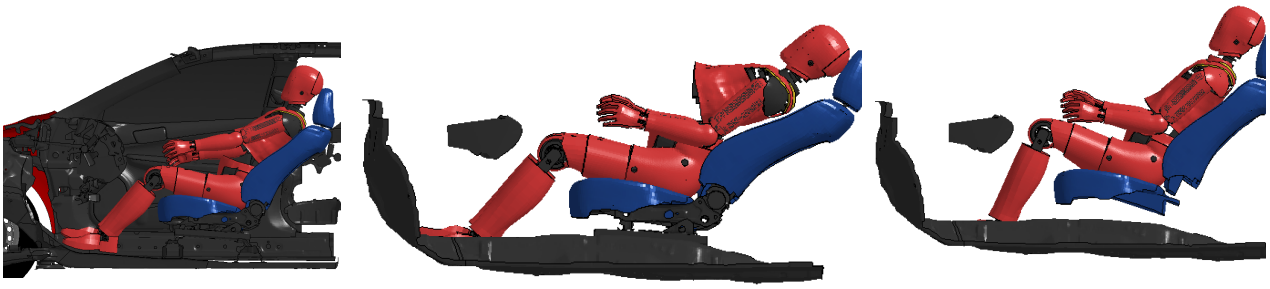

45^0 60^0 Estimated limit (40^0)

Figure 22. THOR FE model integration into reclined seat.

Because there was interference of the upright (25˚) seated THOR FE model with the windshield, roof, and the floor in some proposed seat rotations, it was necessary to adjust the nominal position of THOR. Since the goal of this study was to compare the occupant response in several seating configurations, a unified seating position that fit all of the proposed seat positions was developed. This was achieved via the occupant positioning tree (**Figure 23**).

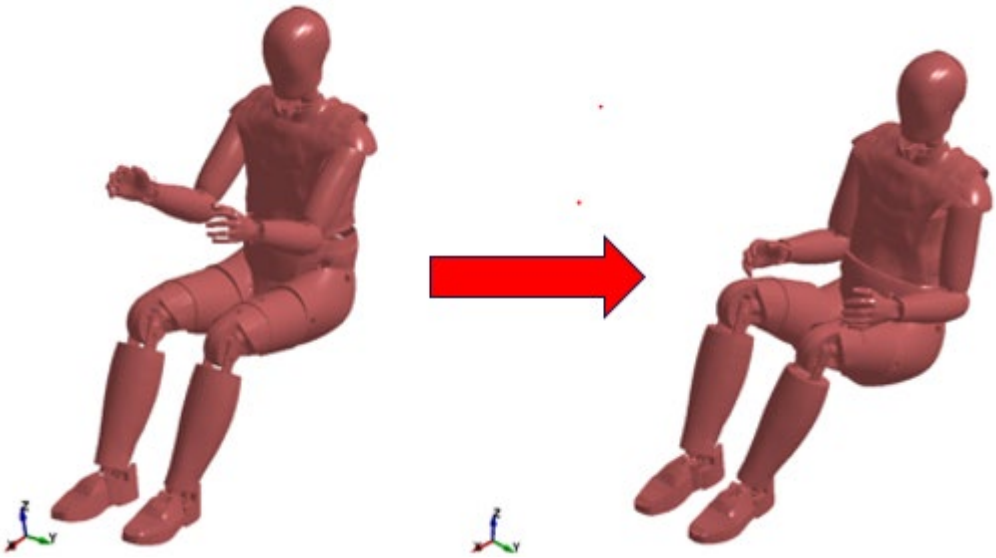

Figure 23. Nominal THOR position in this study.

4.1.5 THOR FE model modification

Because the current version of the THOR FE model has a gap in the jacket mesh to allow for easy positioning of the model without mesh quality issues, a shell element part with null material was created to fill the gap of the jacket for the THOR FE model (**Figure 24**). This was used for contact purposes.

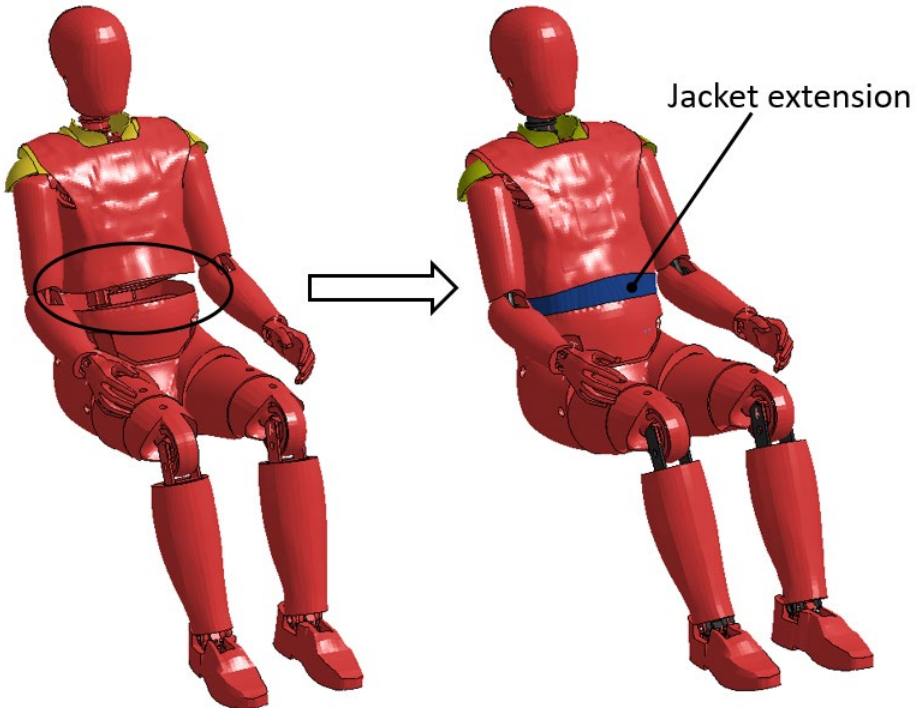

Figure 24. Jacket modification for the THOR FE model.

4.2 GHBMC M50-OS

4.2.1 Integration challenges

The GHBMC M50-OS model was delivered to UVA from Elemance with an encryption file that contained many of the model keywords, including CONTACT_INTERIOR and the part set referenced by this keyword. Since only one instance of CONTACT_INTERIOR is allowed in an LS-Dyna simulation, and the Toyota Camry model used this keyword for its stability, integrating the M50-OS model into the vehicle resulted in immediate failure of the simulation to initiate. After identifying the model conflict, which was challenging because the contents of the encryption file were unknown, we were able to receive an updated M50-OS model from Elemance[1] without *CONTACT_INTERIOR encrypted so that the HBM and the vehicle model keywords could be combined.

4.2.2 Units

Due to different unit systems between GHBMC M50-OS and the vehicle model, the GHBMC M50-OS was converted to tonne, millimeter, and second unit system using the *INCLUDE_TRANSFORM keyword.

4.2.3 Seating

To accommodate the variations in sitting postures and seat positions outlined in the simulation matrix, the GHBMC M50-OS was positioned using the pre-simulation method. Under simulated gravity load, M50-OS settled into the seat and reclined back into the seatback (**Figure 25**). However, due to the high stiffness of the spine in the model, positioning the upper torso of the occupant on the seatback was not possible without additional external force (**Figure 26** and **Figure 27**). An additional simulation was required for 45° recline and 60° recline. In these positions, M50-OS was further reclined by prescribing displacements to pull the head and shoulders back (**Figure 28** and **Figure 29**). For the last step, the lower arms were positioned through the positioning tree (**Figure 30** and **Figure 31**).

[1] Editor's Note: Elemance, of Clemmons, NC, according to its website, "is the exclusive distributor of the GHBMC models, to both commercial and academic users. We license the complete family of human body models, encompassing both male and female, a range of postures, and varying levels of complexity. In addition to licensing, Elemance provides comprehensive maintenance, enhancement and support of licensed models, as well as consulting services related to biomechanics, injury biomechanics, and other human modeling applications."

Figure 25. Upright (25˚) seated M50-OS after gravity settling only.

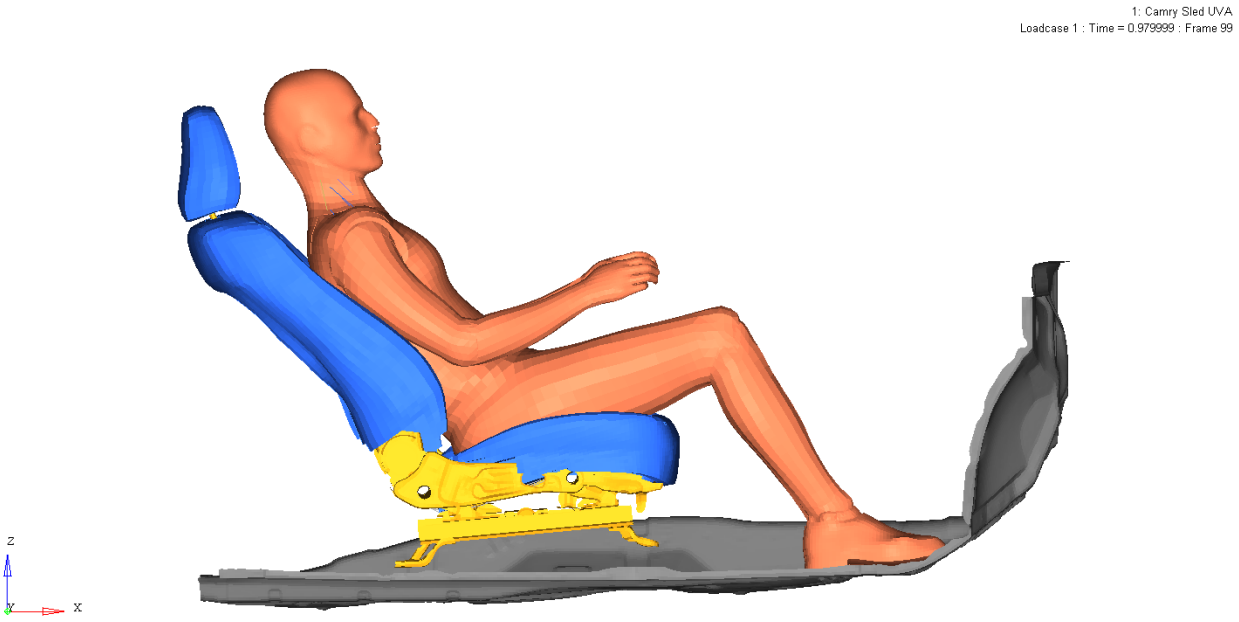

Figure 26. Semi-reclined (45˚) seated M50-OS after gravity settling only.

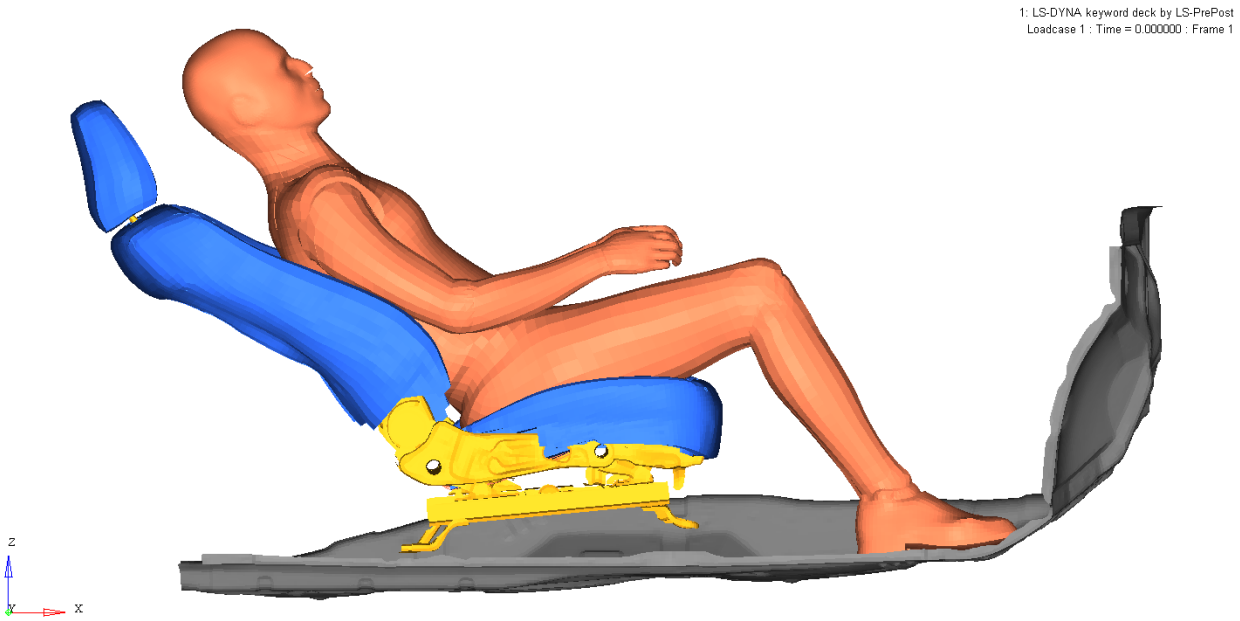

Figure 27. Reclined (60˚) seated M50-OS after gravity settling only.

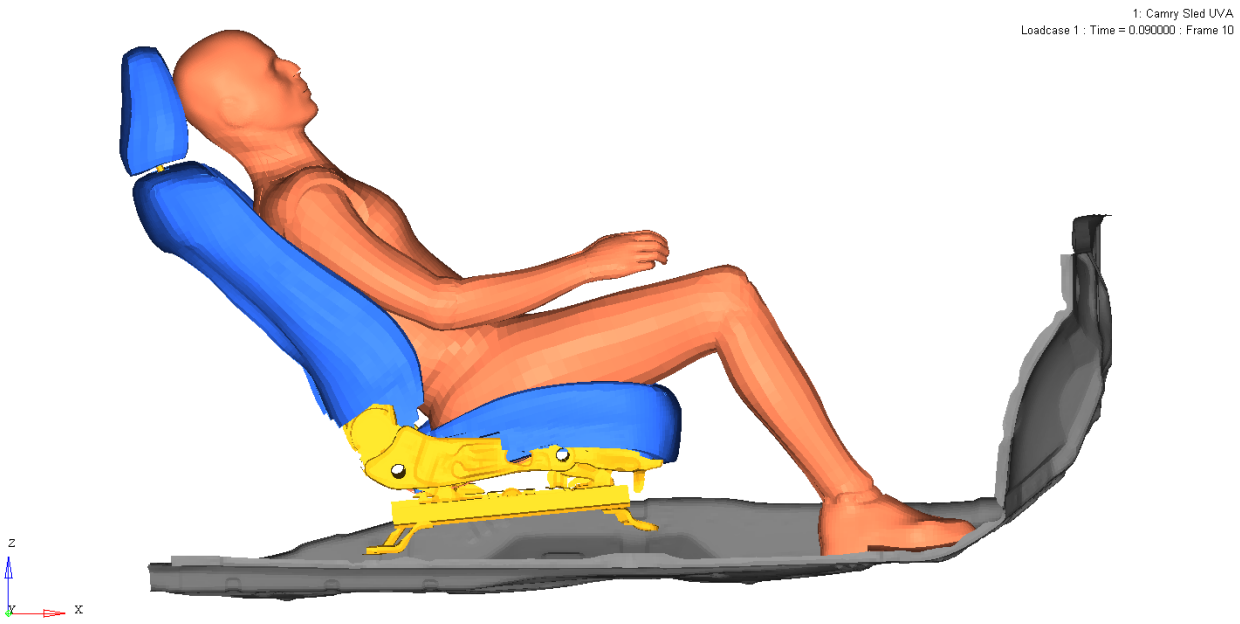

Figure 28. Semi-reclined (45˚) seated M50-OS after forcing the shoulders and head back into the seat.

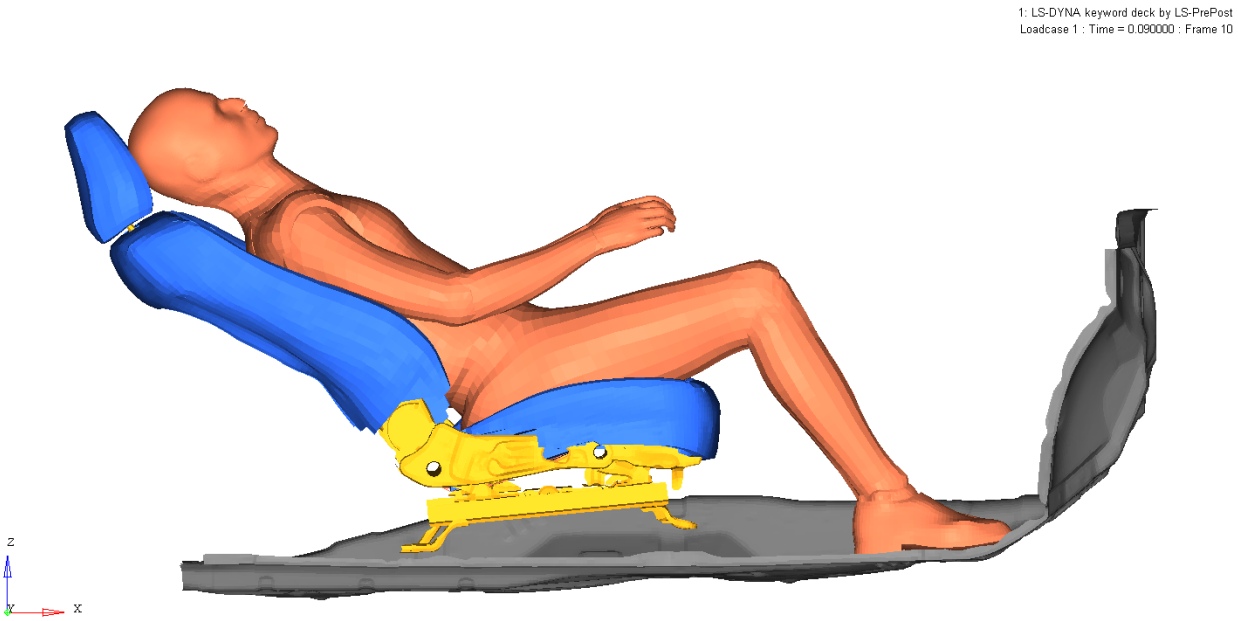

Figure 29. Reclined (60˚) seated M50-OS after forcing the shoulders and head back into the seat.

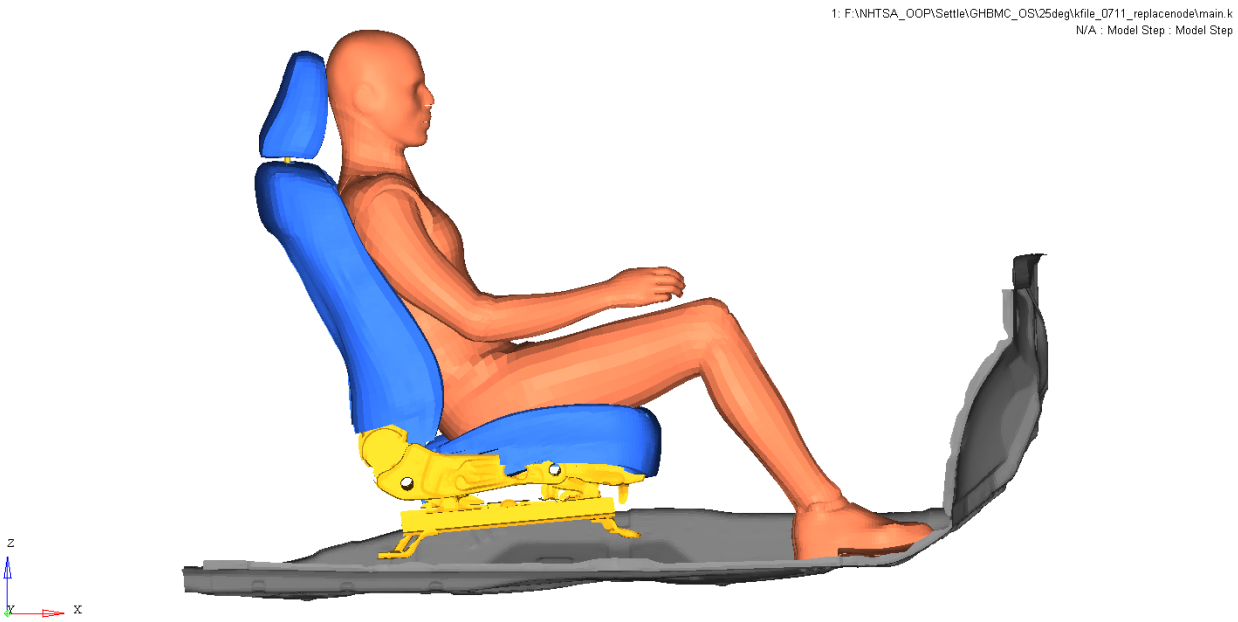

Figure 30. Upright (25˚) seated M50-OS in the final position after lowering the arms.

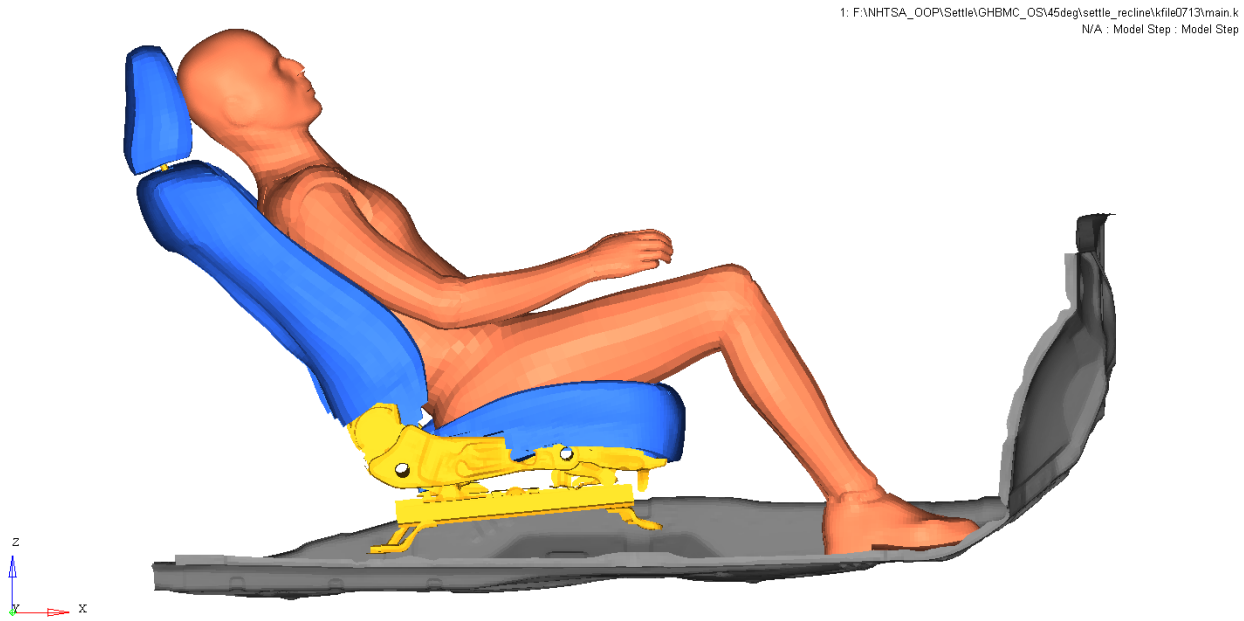

Figure 31. Semi-reclined (45˚) seated M50-OS in the final position after lowering the arms.

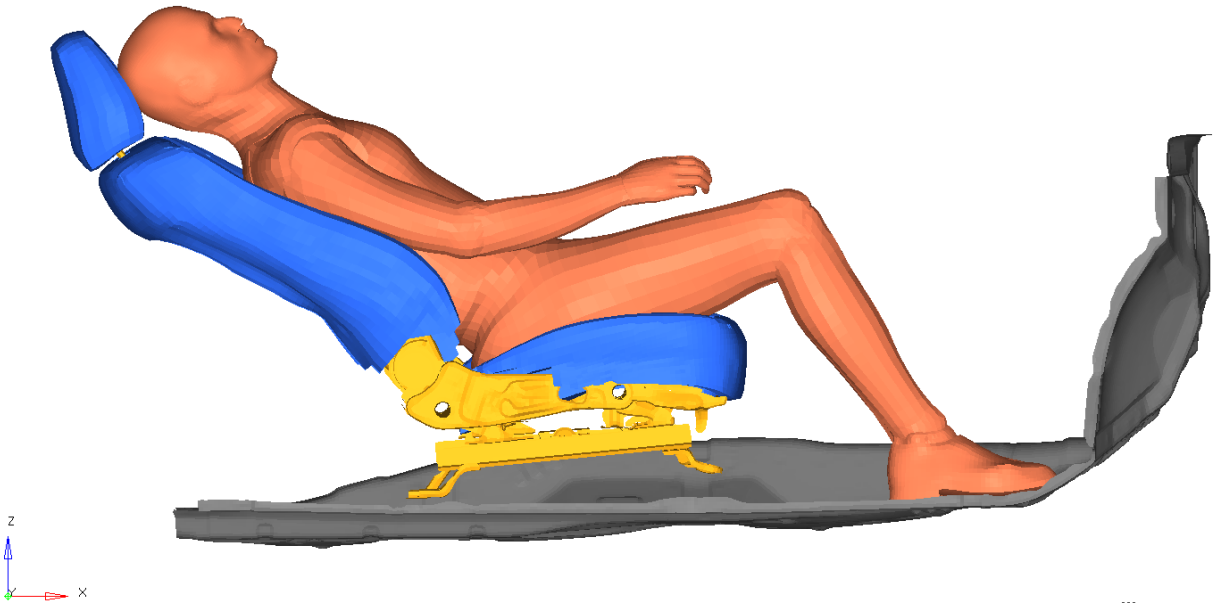

Figure 32. Reclined (60˚) seated M50-OS in the final position after lowering the arms.

4.2.4 Turned posture

To achieve a turned posture for Study C (Table 3), the torso of the M50-OS model was turned towards rear seats via pre-simulation method. The lower extremities were fixed and for hands, arms, and shoulders, they were all free to move. Additionally, the displacements were prescribed to the left clavicle and the cerebral dura along the individually defined vectors since they were both modeled as rigid bodies. **Figure 33** displays the positioned M50-OS after the pre-simulation.

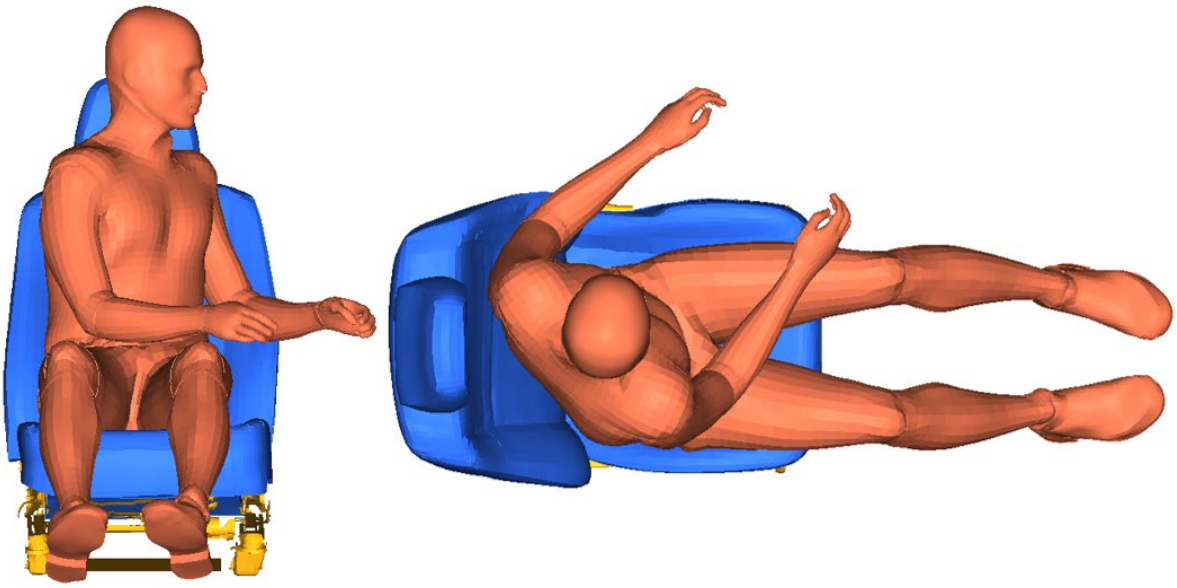

Figure 33. Seated and turned M50-OS model after positioning.

4.2.5 Leaning posture

To achieve a leaning posture for Study D (Table 4), the head and torso of the M50-OS was positioned through the pre-simulation method. Taking upright M50-OS as an example, the sled buck model with corresponding integrated seat belt was used to position the occupant that saved time by eliminating the need to reroute the shoulder belt. During pre-simulation, the lower extremities and hands were fixed. A displacement was then prescribed to the cerebral dura along the defined vector (**Figure 34**). For semi-reclined and reclined seated M50-OS, the same method was performed to position them leaning on belts (**Figure 35** and **Figure 36**).

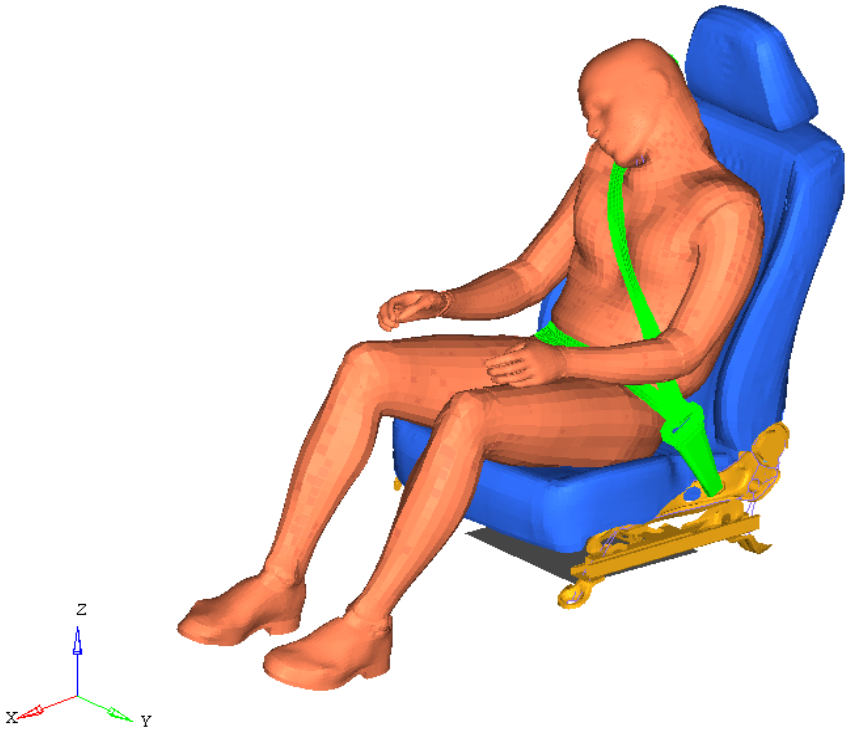

Figure 34. Upright seated and leaning M50-OS after being positioned.

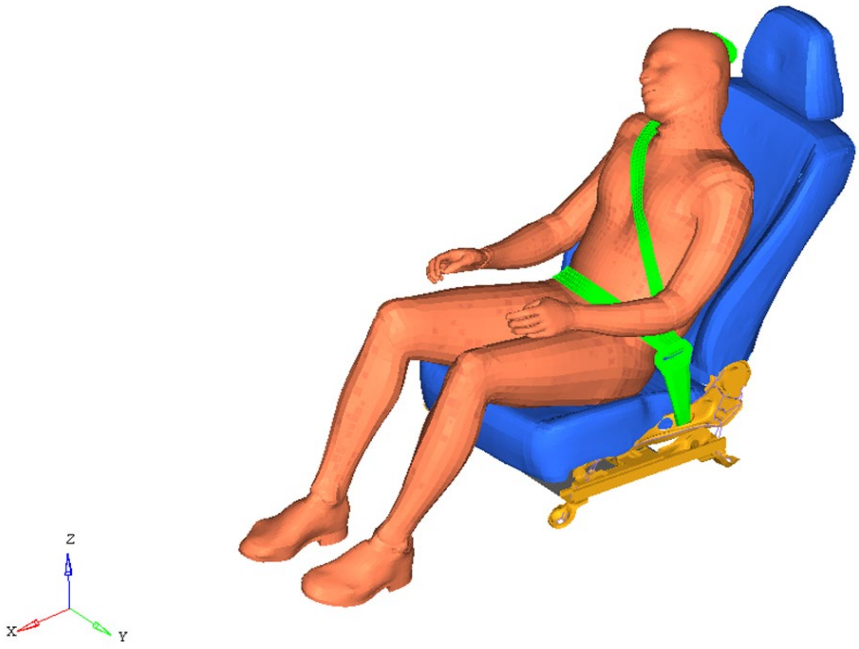

Figure 35. Semi-reclined seated and leaning M50-OS after being positioned.

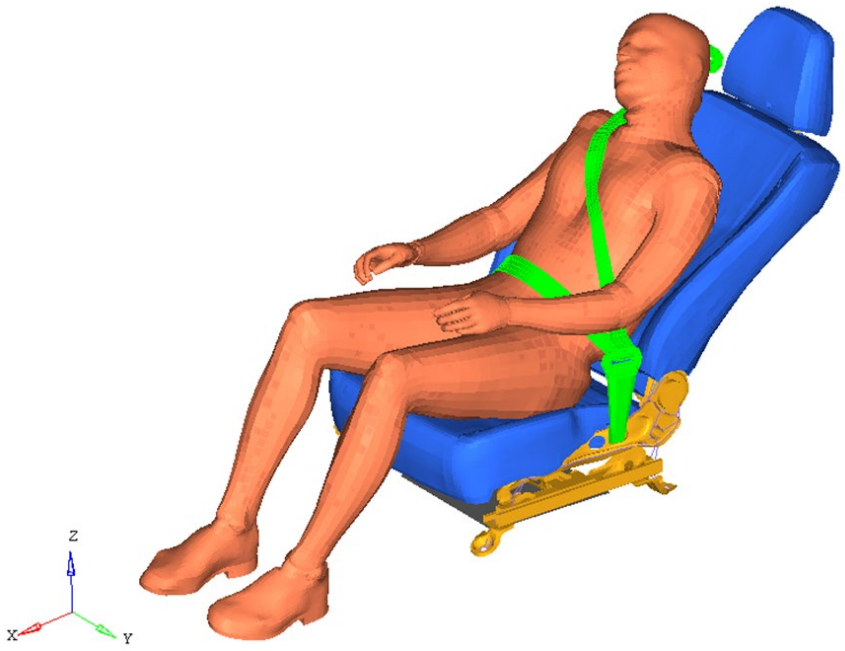

Figure 36. Fully reclined and leaning M50-OS after being positioned.

4.3 GHBMC-M50-O

4.3.1 Integration challenges

Since GHBMC M50-O V4.5 was encrypted and it was difficult to solve the issue that the unit of time failed to be transferred, we switched back to the unencrypted GHBMC M50-O V4.4.

4.3.2 Units

Due to different unit systems between GHBMC M50-O and the vehicle model, the GHBMC M50-O was converted to tonne, millimeter, second using the *INCLUDE_TRANSFORM keyword.

4.3.3 Seating

To accommodate the variations in sitting posture and seat position outlined in the simulation matrix, the M50-O was positioned using the simulation method that is similar as M50-OS. Additionally, the M50-O thorax was observed to be stiffer than the M50-OS during the gravity settling phase of the seating process (**Figures 37 – 39**). The upright (25°) seated M50-OS was able to be directly positioned on the seatback with gravity, however, the M50-O required one more simulation to pull it back to the seatback. Furthermore, during the positioning process, several rib elements failed by reaching the failure plastic strain implemented for injury evaluation. We believe this issue was a result of the current GHBMC flesh and skin models, and this is an area of the model that is currently being addressed by the GHBMC. Once the plastic strain reached the failure threshold, the elements were eliminated. Since there's no need to evaluate injuries during the positioning process, the failure of plastic strain was disabled to avoid element elimination.

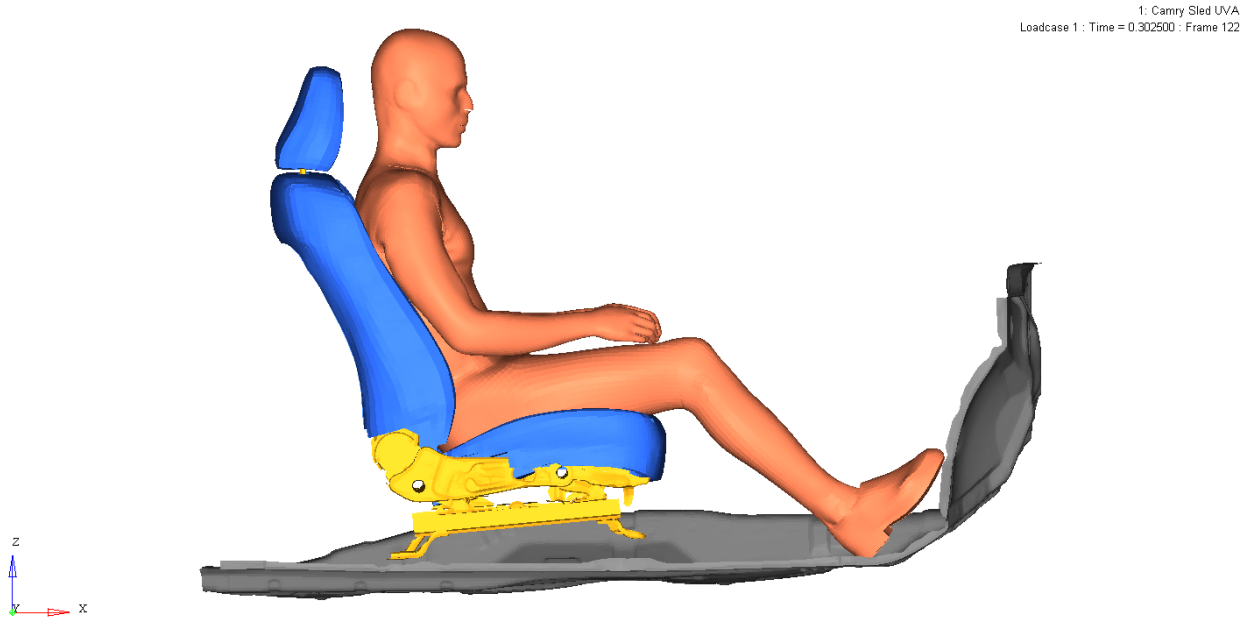

Figure 37. Upright (25˚) seated M50-O after gravity settling.

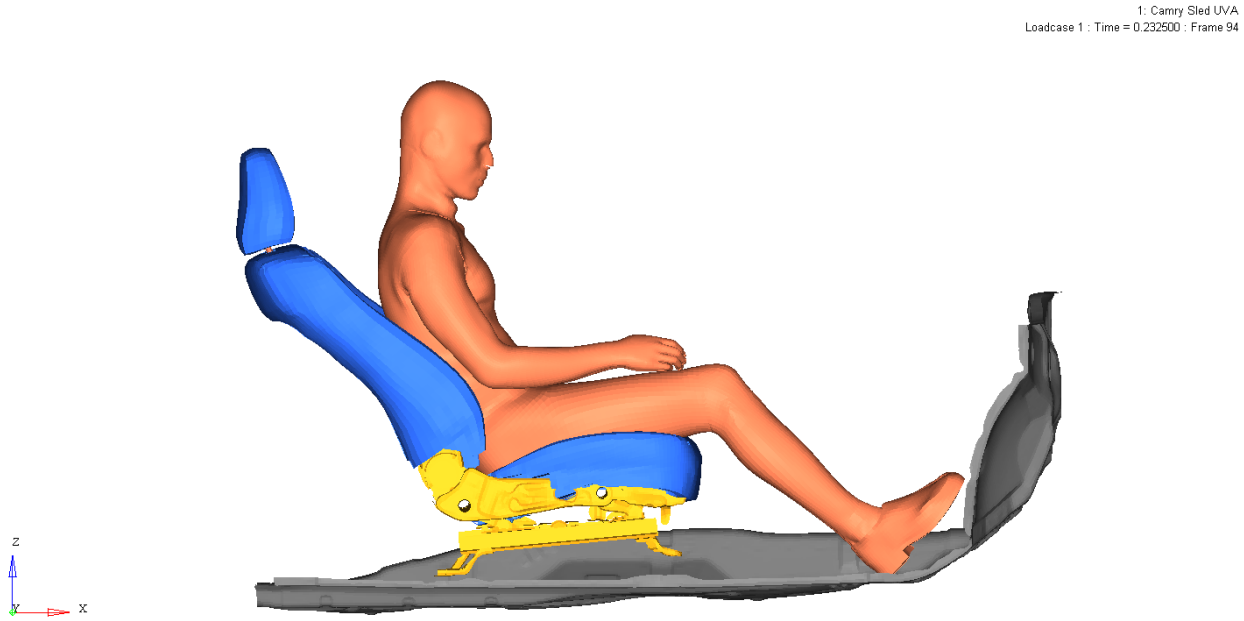

Figure 38. Semi-reclined (45°) seated M50-O after gravity settling.

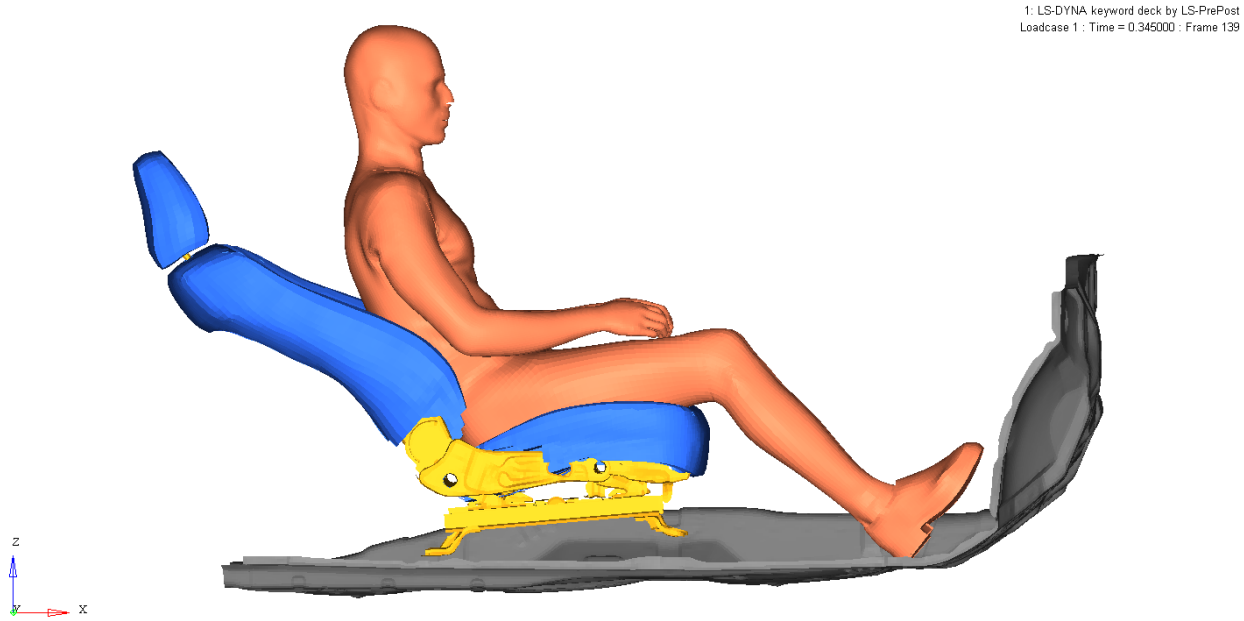

Figure 39. Reclined (60°) seated M50-O after gravity settling.

After settling the M50-O, we compared the position of M50-O with that of M50-OS by overlaying 2 models and realized they did not quite match with each other (**Figure 40**). Differences in the positions of the scapula, pelvis, femur, tibia, and feet were noted.

Figure 40. Position comparison between M50-O and M50-OS in the upright (25°) seat after gravity settling.

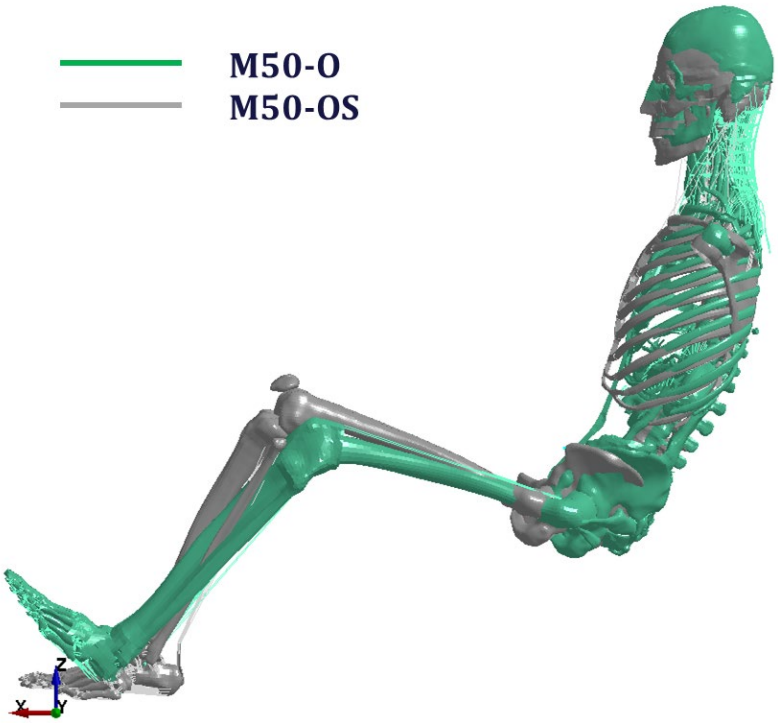

To make the positioning consistent, we ran additional simulations for M50-O to match M50-OS posture (**Figure 41**). First, 3-point transform that is a transformation tool in LS-Prepost was used to match pelvis (**Figure 42**). Second, we used cable discrete beams to pull components of the M50-O model to the desired position. Taking the upright M50-O as an example, there were 17 points in the upper body that were selected to match those of M50-OS (**Figure 43** and **Figure 44**). The same method was implemented to position femur, hands, tibia, and feet (**Figure 45** and **Figure 46**).

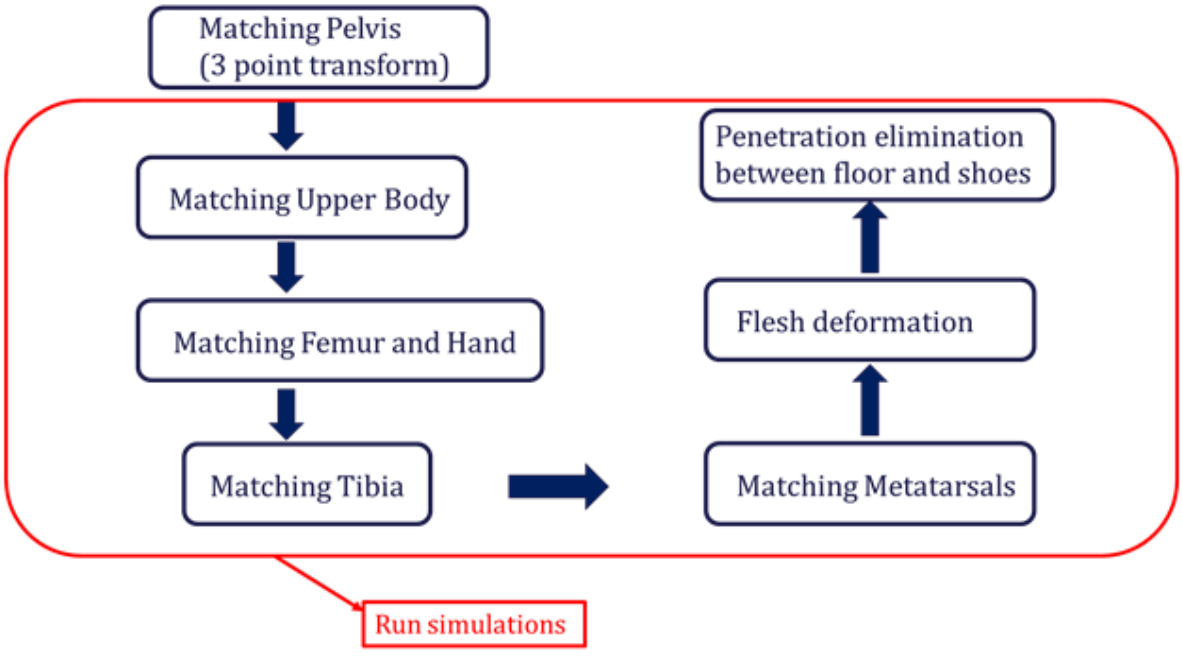

Figure 41. Flow chart to match the position of M50-O with M50-OS.

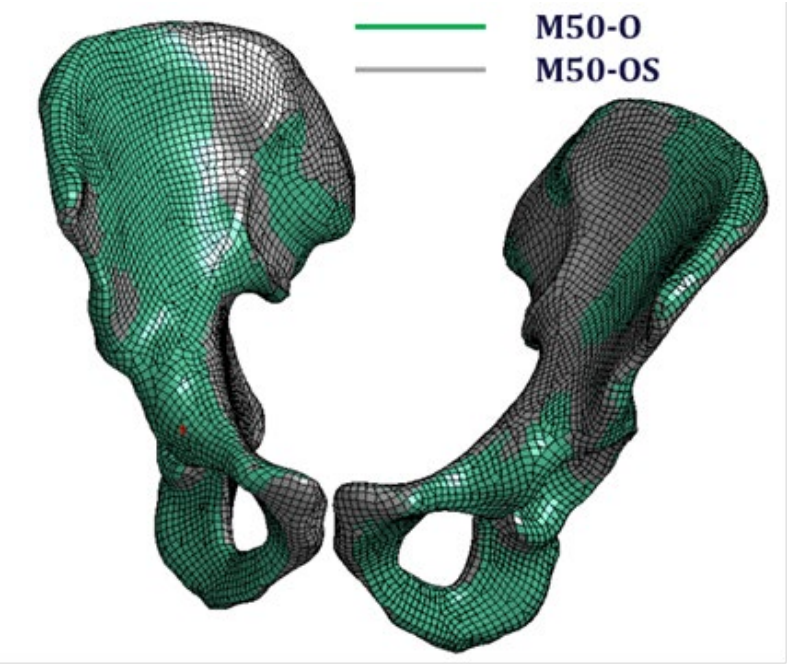

Figure 42. Comparison of position between the M50-O and M50-OS after pelvis matching.

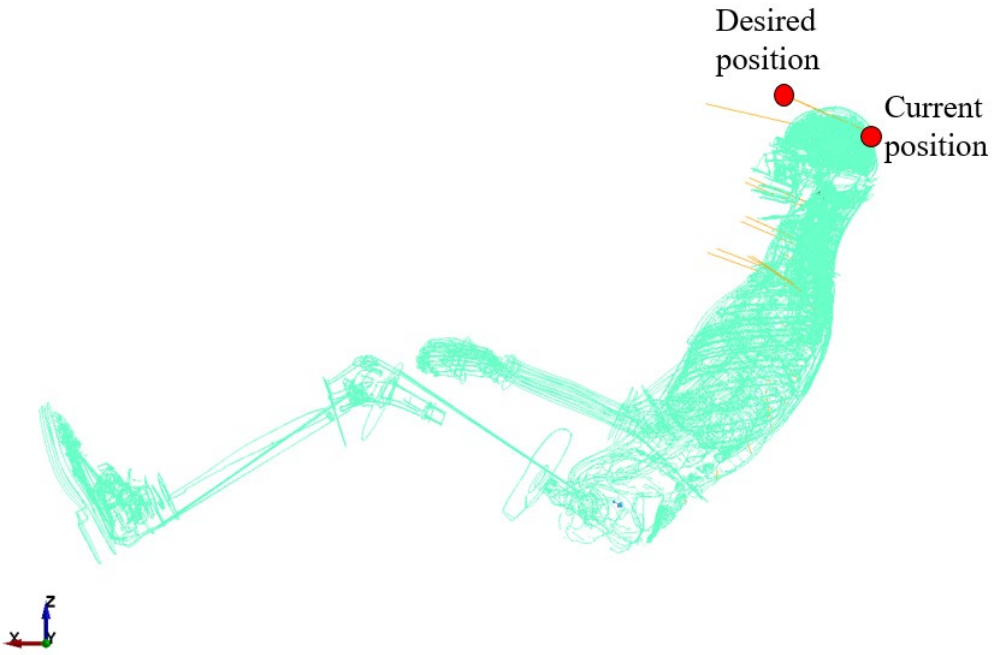

Figure 43. Cable pulling method for the M50-O upper body to match positions in the M50-OS.

	M50-O	M50-OS (Desired location)
T1	NODE ID= 4131106	NODE ID=407508
T3	NODE ID= 4131929	NODE ID=407810
T5	NODE ID= 4131588	NODE ID=407698
T7	NODE ID= 4131372	NODE ID=407620
T9	NODE ID= 4131196	NODE ID=407550
T11	NODE ID= 4130770	NODE ID=407463
L1	NODE ID= 6039214	NODE ID=600114
L3	NODE ID= 6041506	NODE ID=601367
L5	NODE ID= 6044720	NODE ID=603162
Dura L	NODE ID= 1493900	NODE ID=151256
Dura R	NODE ID= 1444501	NODE ID=122930
Dura M	NODE ID= 1444206	NODE ID=122635
clavicle L	NODE ID= 4003248	NODE ID=318565
clavicle L M	NODE ID= 4003201	NODE ID=318534
clavicle L(inner)	NODE ID= 4004349	NODE ID=319106
clavicle R	NODE ID= 4150380	NODE ID=502365
clavicle R(inner)	NODE ID= 4151583	NODE ID=502988
clavicle R M	NODE ID= 4150403	NODE ID=502384

Figure 44. Points used to match the M50-O upper body with M50-OS.

	M50-O	M50-OS (Desired location)
L hand	NODE ID= 3020451	NODE ID=310553
L hand	NODE ID= 3012730	NODE ID=305326
L hand	NODE ID= 3017812	NODE ID=308760
R hand	NODE ID= 5017022	NODE ID=509635
R hand	NODE ID= 5024717	NODE ID=514846
R hand	NODE ID= 5019652	NODE ID=511422
L Femur	NODE ID= 7024276	NODE ID=702610
L Femur	NODE ID= 7029991	NODE ID=704177
L Femur	NODE ID= 7025279	NODE ID=702857
R Femur	NODE ID= 9046258	NODE ID=913085
R Femur	NODE ID= 9039218	NODE ID=911201
R Femur	NODE ID= 9040888	NODE ID=911610

Figure 45. Points used to match the M50-femur and hands with M50-OS.

	M50-O	M50-OS (Desired location)
Metatarsal L	NODE ID= 7909385	NODE ID= 81943437
Metatarsal L	NODE ID= 7909810	NODE ID= 82145461
Metatarsal L	NODE ID= 7912133	NODE ID= 81943862
Metatarsal R	NODE ID= 7912133	NODE ID= 81946031
Metatarsal R	NODE ID= 79121336	NODE ID= 82141736
Metatarsal R	NODE ID= 7912133	NODE ID= 82142860

Figure 46. Points used to match the M50-O metatarsals with M50-OS.

It was problematic to position all the parts at the same time, and the process had to be sequential (**Figure 47** and **Figure 48**). For instance, when positioning tibia and femur simultaneously, the tibia position would match but the femur was too far removed from that of M50-OS. In the end, there was good agreement between the M50-O and M50-OS initial positions in all seating cases **(Figure 49**).

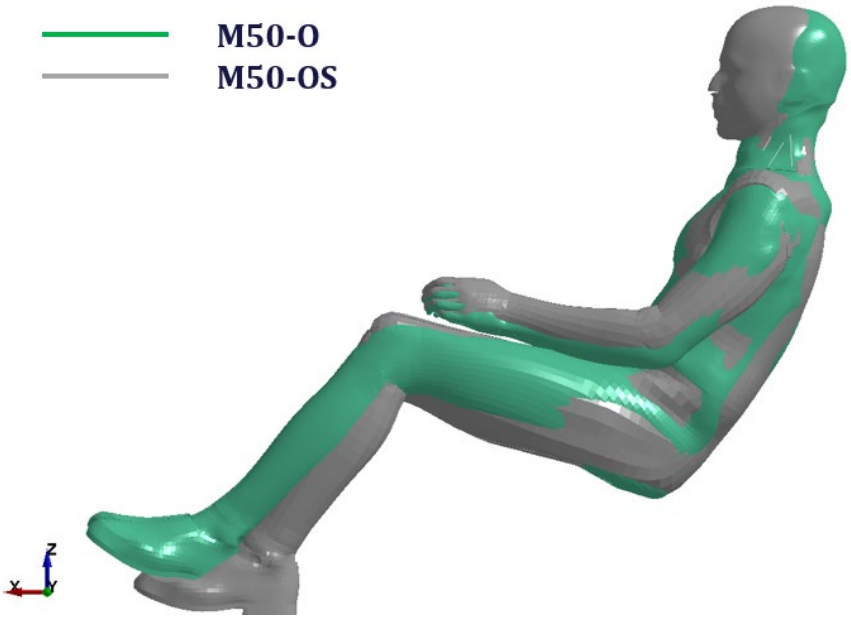

Figure 47. Position comparison between M50-O and M50-OS in the upright (25°) seat after matching upper body, hands, and femur.

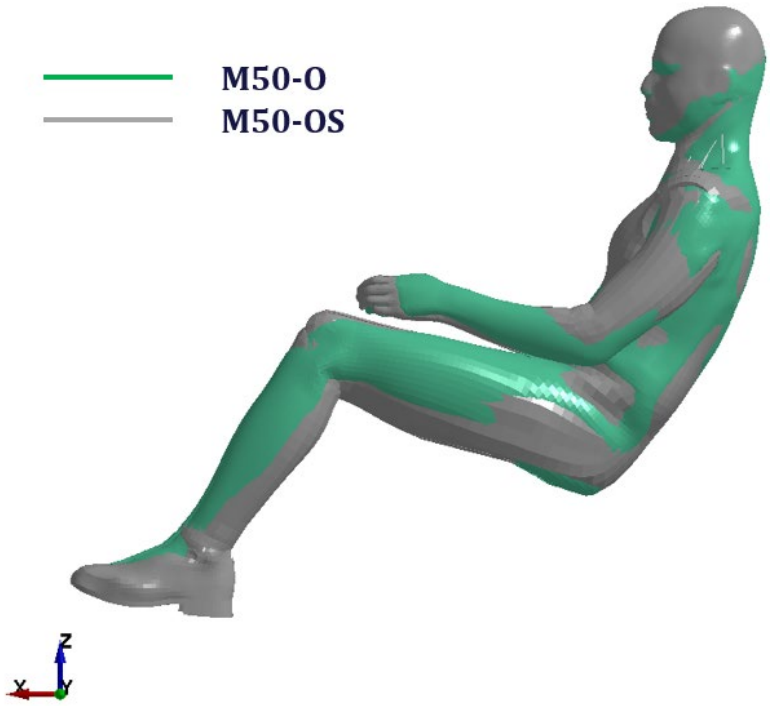

Figure 48. Position comparison between M50-O and M50-OS in the upright (25°) seat after matching upper body, hands, femur, and metatarsals.

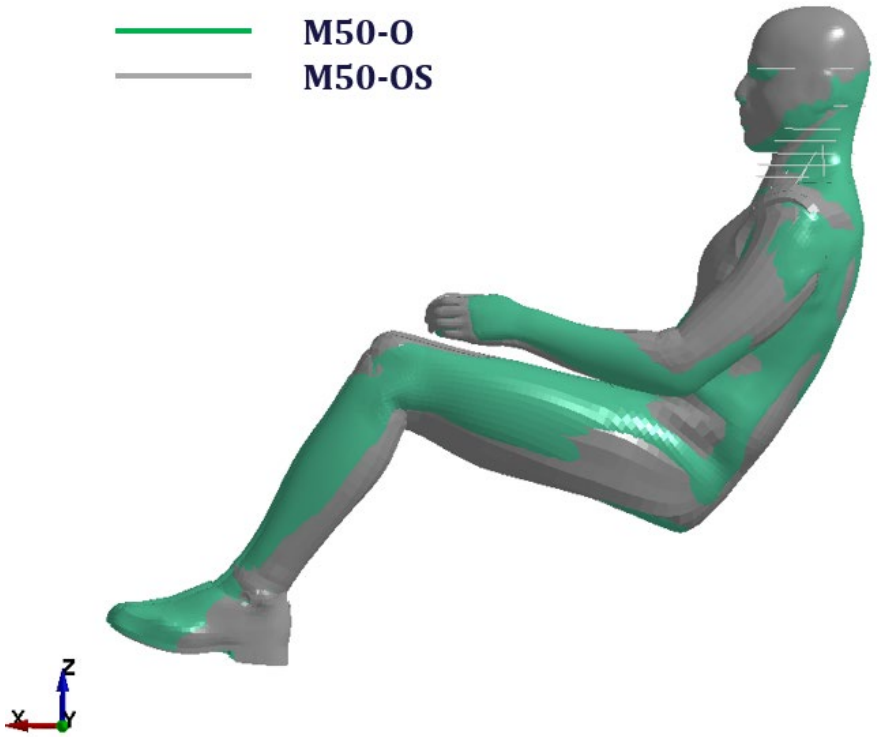

Figure 49. Final position comparison between M50-O and M50-OS in the upright (25°) seat after matching all components and removing penetrations.

After making M50-O match M50-OS for each posture, penetration between flesh and seat cushions was observed. To eliminate the penetration, we offset the M50-O model from the seat and prescribed a displacement to the occupant model to move along the defined vector. With the defined contact, the flesh of M50-O re-deformed again. However, in this simulation, the contact between toe pan and shoes was not defined, which caused penetration among these parts. Therefore, the last simulation was to offset the floor and prescribe the motion to the rigid toe pan along positive Z so as to eliminate penetration.

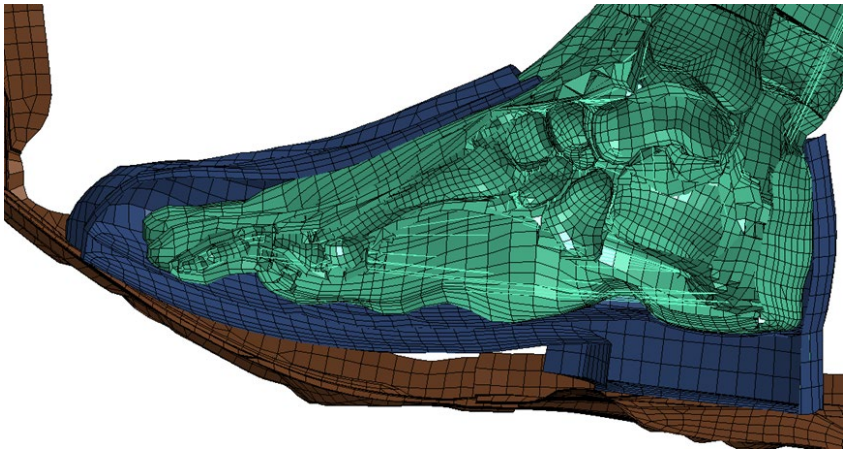

Figure 50. Final clearance check between the toe pan and shoes for M50-O.

The final seated positions for the M50-O model is shown in **Figure 51**, **Figure 52**, and **Figure 53**.

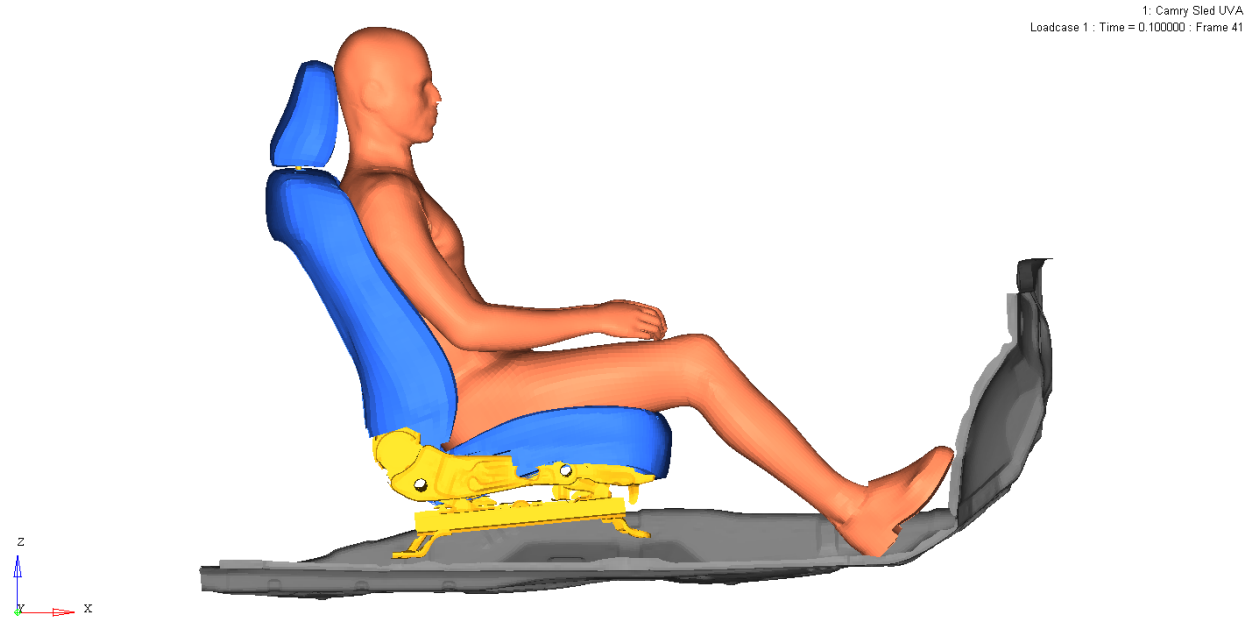

Figure 51. Upright (25˚) seated M50-O model after positioning.

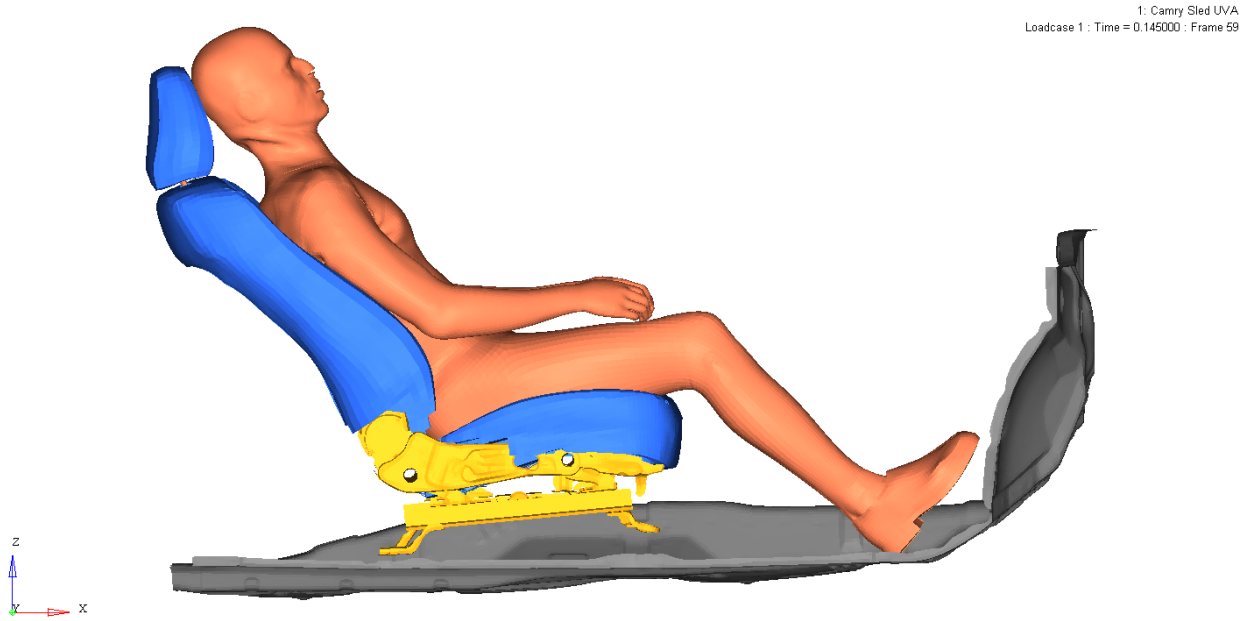

Figure 52. Semi-reclined (45˚) seated M50-O model after positioning.

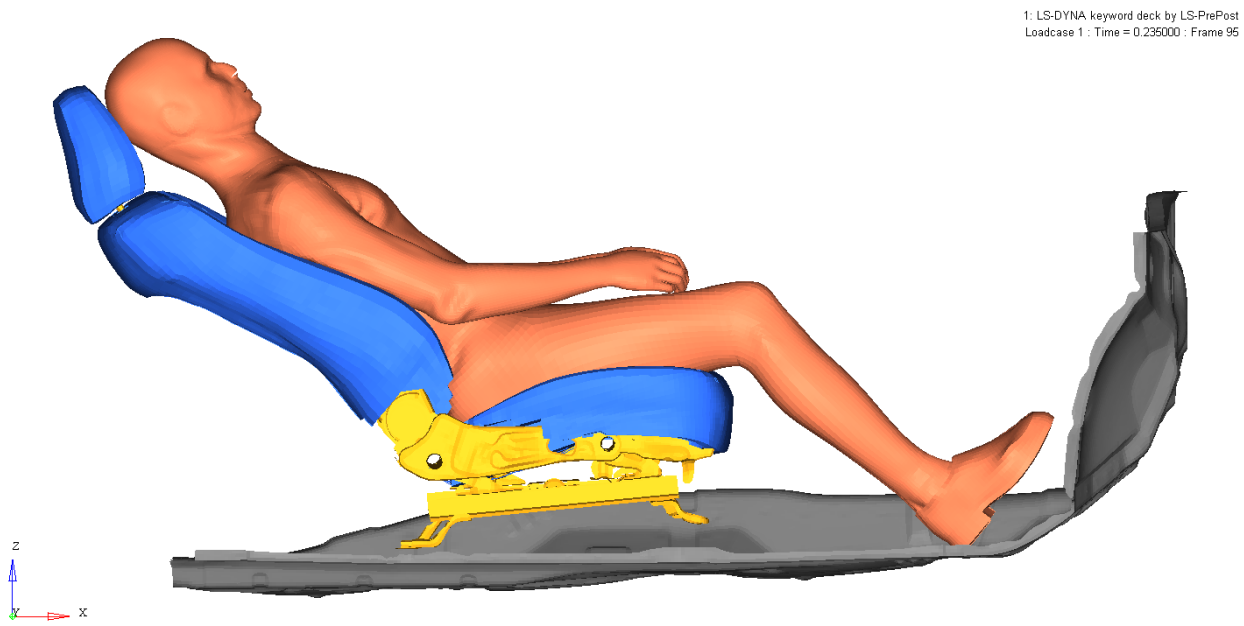

Figure 53. Reclined (60°) seated M50-O model after positioning.

4.4 Seat Belt Integration With Occupant Models

With the completed positioning of the THOR and GHBMC models, the integrated and standard seat belt routings were carried out. A beltFit algorithm, available in LS-Prepost, was used for this task. An individual belt FE model was generated for standard and integrated belt in both upright, semi-reclined, and reclined occupant positions. A selection tree was used in the parametric model to select the appropriate belt model file for the desired occupant and seating configuration (**Figure 54**). Belts for alternative seat orientations (30°, 90°, 135°, and 180°) were obtained by

using the *INCLUDE TRANSFORM keyword. An example of seat belt fits for the THOR model is shown in **Figures 56 – 60**.

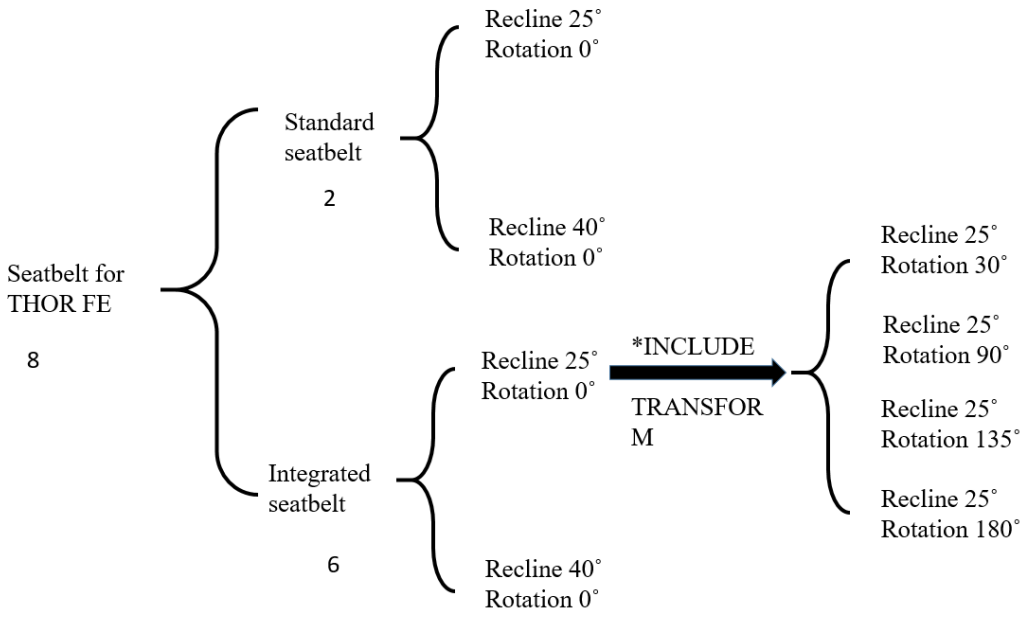

Figure 54. Seat belt models selection tree (example for THOR).

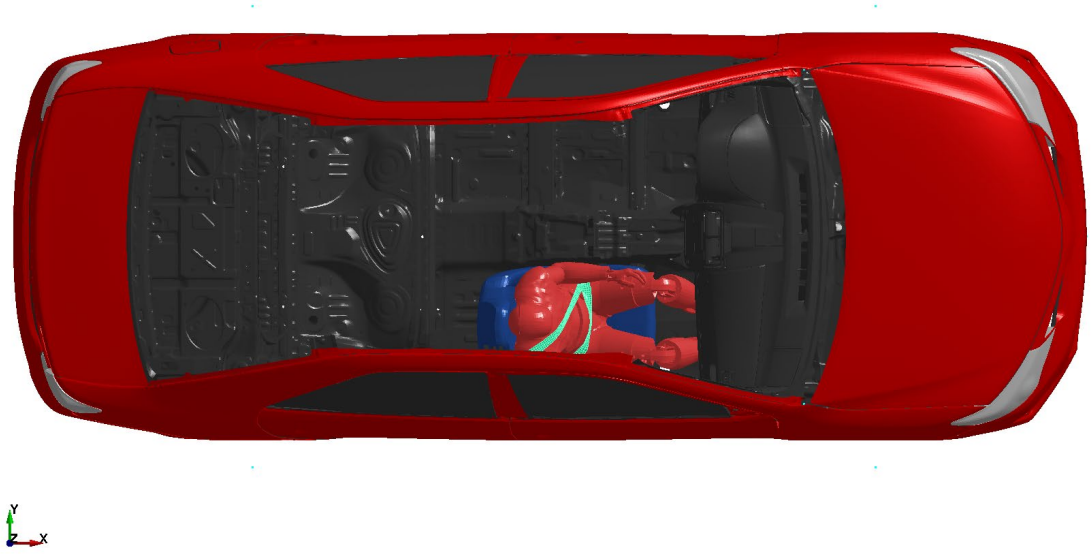

Figure 55. THOR fit with the integrated seat belt in the 0° seat position.

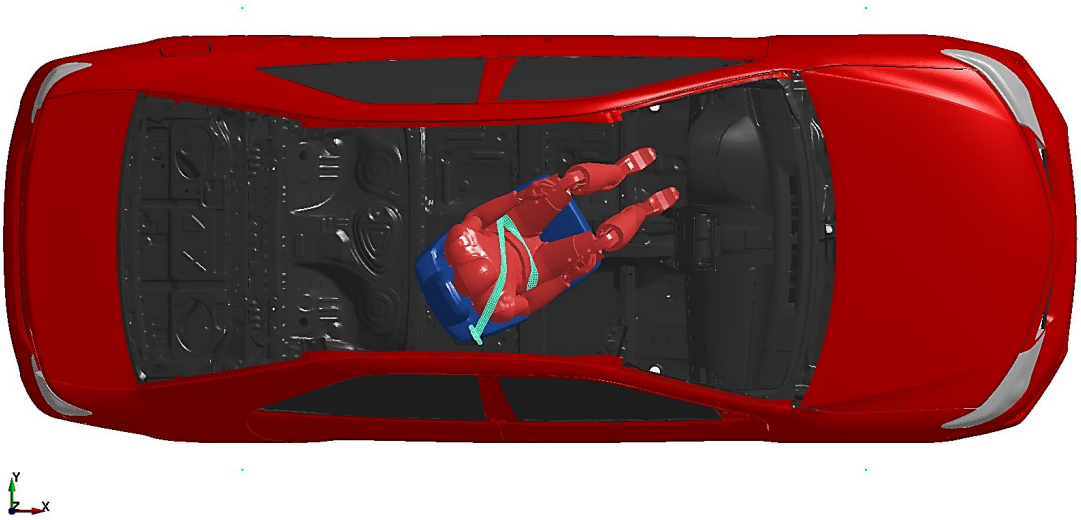

Figure 56. THOR fit with the integrated seat belt in the 30° seat position.

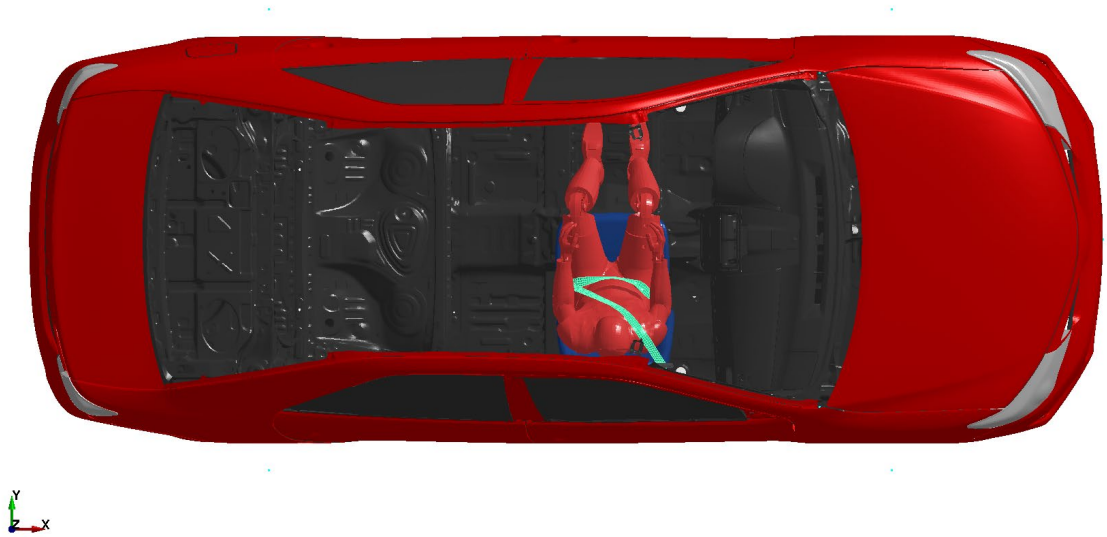

Figure 57. THOR fit with the integrated seat belt in the 90° seat position.

Figure 58. THOR fit with the integrated seat belt in the 135° seat position.

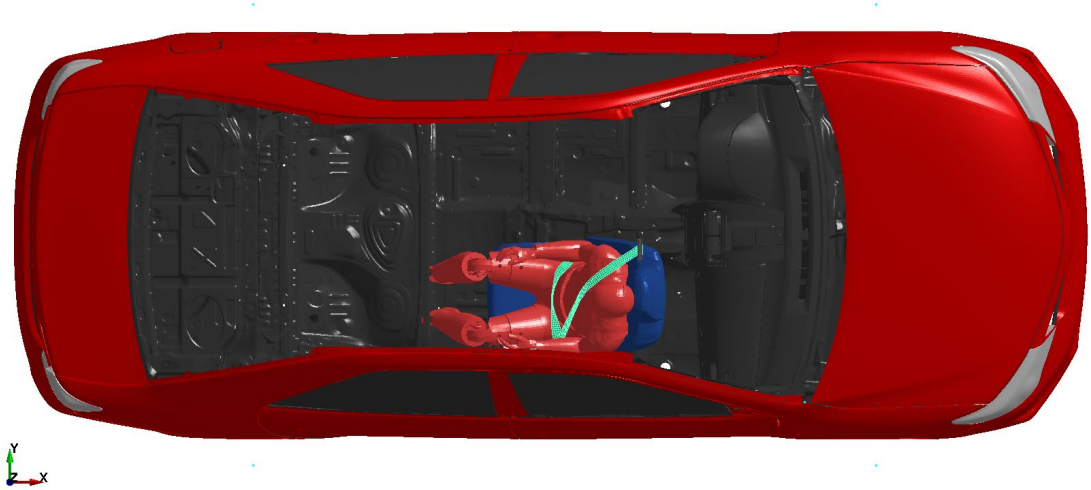

Figure 59. THOR fit with the integrated seat belt in the 180° seat position.

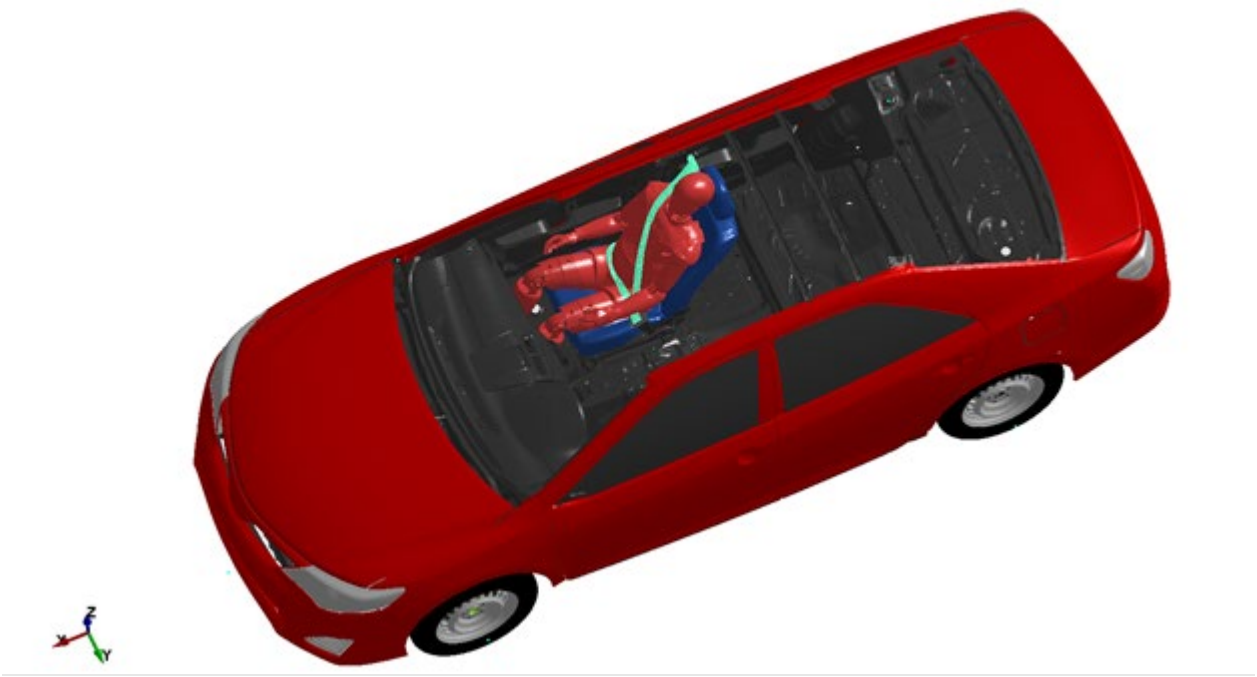

Figure 60. THOR fit with the integrated seat belt in the 40˚ reclined position.

5 Instrumentation Modelling

5.1 Injury Risk

To assess the risk of injury in performed crash simulations, the injury criteria and risk curves that have been used in NHTSA research, and previously published (Saunders, 2015) were used. Some modifications were made based on the expected crash scenarios for occupants in ADS-equipped vehicles. The capability of current occupant models (THOR, GHBMC M50-OS, GHBMC M50-O) in assessing injury risk is summarized (Table 6).

Table 6. The capability of injury assessment for THOR FE, GHBMC M50-OS and GHBMC M50-O models

Injury Criteria (reference)	THOR	M50-OS	M50-O
HIC_{15} (Versace, 1971)			
BrIC (Takhounts, 2013)			
N_{ij} (Eppinger, 1999)			
cN_{ij} (TBD)			
NIC (Bostrom, 1998)			
Shoulder Load (Petitjean, 2012)			
Clavicle Load (Zhang, 2014)			
Multi-point Thoracic Injury Criterion or PCA (Crandall, 2013)			
Rib Strain (TBD)			
Abdomen Compression (Kent, 2008)			
Lateral Shoulder, Chest and Abdomen deflection (Petitjean, 2012)			
Lumbar Spine Load (TBD)			
ASIS Load (TBD)			
Sacral Iliac Load (TBD)			
Acetabulum Load (Martin, 2011)			
Pubic Symphysis Load (Petitjean, 2012)			
Femur Axial Load (Kuppa, 2001)			
Revised Tibia Index (Kuppa, 2001)			
Distal Tibia Axial Force (Kuppa, 2001)			
Proximal Tibia Axial Force (Kuppa, 2001)			

Green: The model has the required instrumentation to output the injury metric.
Yellow: The current model doesn't have the required instrumentation to output the injury metric, but there's potential to access the injury after instrumentation.
Red: The model is not capable of predicting the injury metric.

5.2 Added Capability

The THOR FE model was designed to allow output measurements similar as those recorded by the instrumentation of the physical dummy. The GHBMC M50-OS, unlike its more detailed counterpart, is not intended to predict crash induced injuries based on tissue-level criterion, but virtual instrumentation (load cell, accelerometer, and deflection sensor) is required to be integrated in the simplified model for injury risk assessment. To assess injury and extract injury criteria from the current GHBMC M50-OS model, the following preparations were made.

5.2.1 Accelerations and angular velocities

Tri-axial linear accelerations and angular velocities are measured at anatomical locations including head, C1, T1, T8, T12, and pelvis in the local anatomical coordinate system. The anatomical coordinate systems for each bone in the experiments were defined by locating the specific anatomical landmarks using the 3D geometry (**Figure 61**).

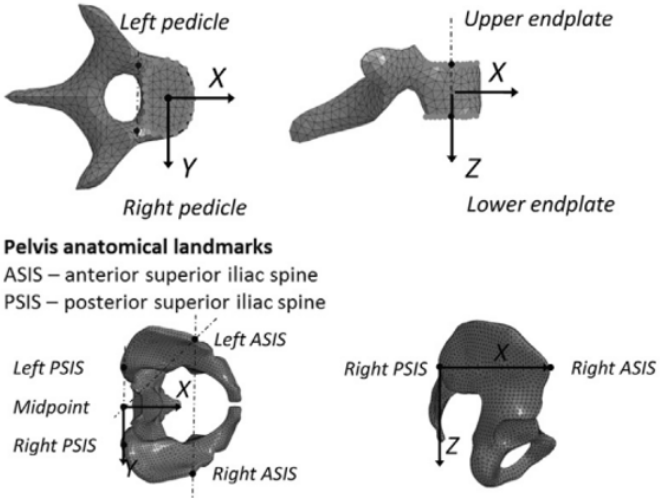

Figure 61. Anatomical coordinate system definition.

5.2.2 Deflection sensor

GHBMC M50-OS was instrumented to measure frontal thorax and abdomen deflection, and lateral shoulder, thorax, and abdomen deflection. The measured locations and referred coordinate systems are similar as those in the IR-TRACCs in the NHTSA THOR ATD and WorldSID-50M ATD (**Figure 62**).

5.2.3 Load cells

GHBMC M50-OS allows for load measurements to be evaluated, including those for neck, clavicle, lumbar spine, and pelvis. Different instrumentation methods were applied according to the modeling methods that worked for different body regions (Table 7 and **Figure 63**).

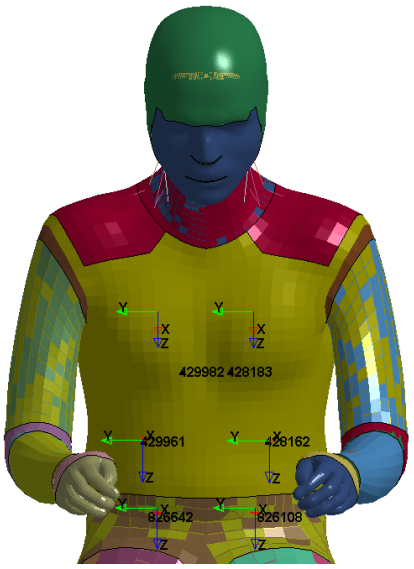

GHBMC M50-OS Instrumentation

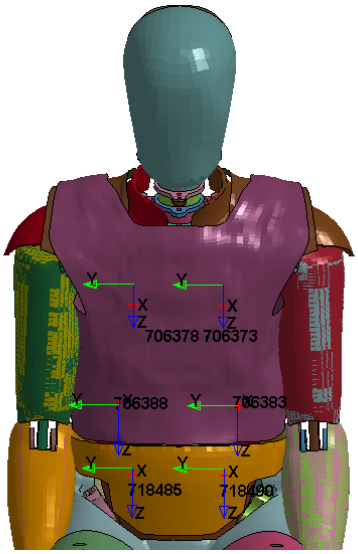

THOR FE IR-TRACCs

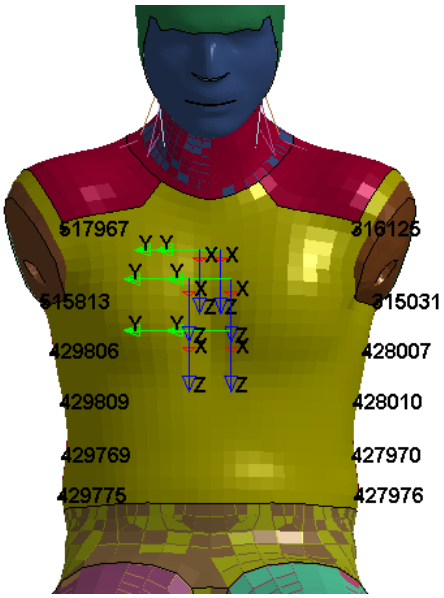

GHBMC M50-OS Instrumentation

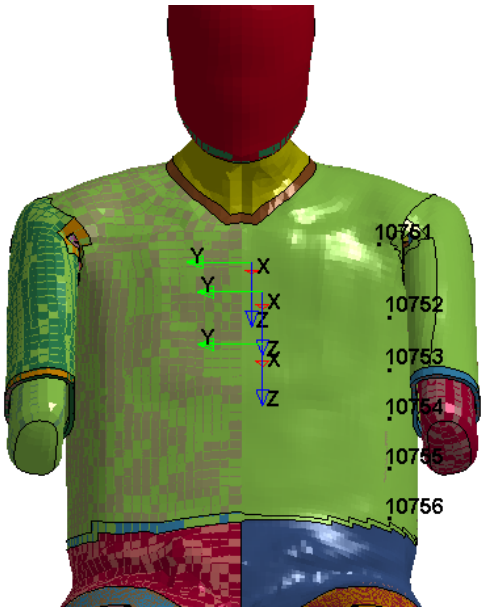

WorldSID 50M FE IR-TRACCs

Figure 62. Deflection sensors defined in GHBMC M50-OS, compared with THOR FE and WorldSID FE IR-TRACCs.

Table 7. Load cells and instrumentation methods used in GHBMC M50-OS

Region	Instrumentation Methods	Notes
Upper/Lower neck (bone)	Discrete beam output	Discrete beam existed
Clavicle	Joint output	Joint existed
Lumbar spine	Cross-section output	Cross-section was newly defined
Acetabulum	Joint output	Joint existed
Public symphysis	Cross-section output	Cross-sections were newly defined
Sacral iliac joint	Cross-section output	
Femur	Discrete beam output	Discrete beam existed, resultant forces and moments of a discrete beam were modified to output in the local coordinate systems (Figure 63)
Tibia	Discrete beam output	

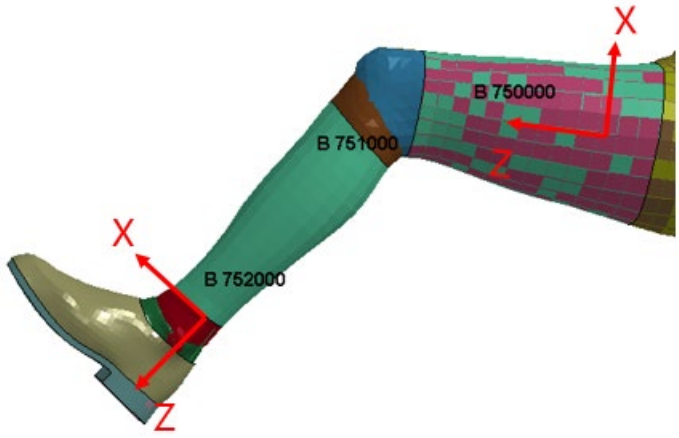

Figure 63. Local coordinate systems for femur and tibia load cells.

5.3 Limitations

To facilitate injury risk assessment, the GHBMC M50-OS was instrumented to extract injury metrics. The model was able to evaluate most of the injury criteria in the current study. Several injury metrics including N_{ij}, shoulder load, and anterior superior iliac spine (ASIS) load were not measured for reasons specified below. The GHBMC M50-OS shoulder complex and neck region are both modelled in a way so that they have multiple loading paths during an impact, the load sustained would be distributed through kinematic joints, solid flesh elements, and ligaments represented as beam elements. So it is difficult to assess the overall load sustained by the shoulder or neck; thus, N_{ij} and shoulder load are not evaluated. Since the iliac wings were modelled as rigid shell elements, the GHBMC M50-OS is not able to output the load sustained by the anterior superior iliac spine (ASIS) through conventional approaches such as the cross-sections output.

5.3.1 Lower extremity moment output from M50-OS

During initial shakedown of the instrumented M50-OS model it was observed that the recorded lower extremity bending moments had very low value. The M50-OS lower extremity moment value was an order of magnitude below the value recorded in the THOR FE model (**Figure 64**).

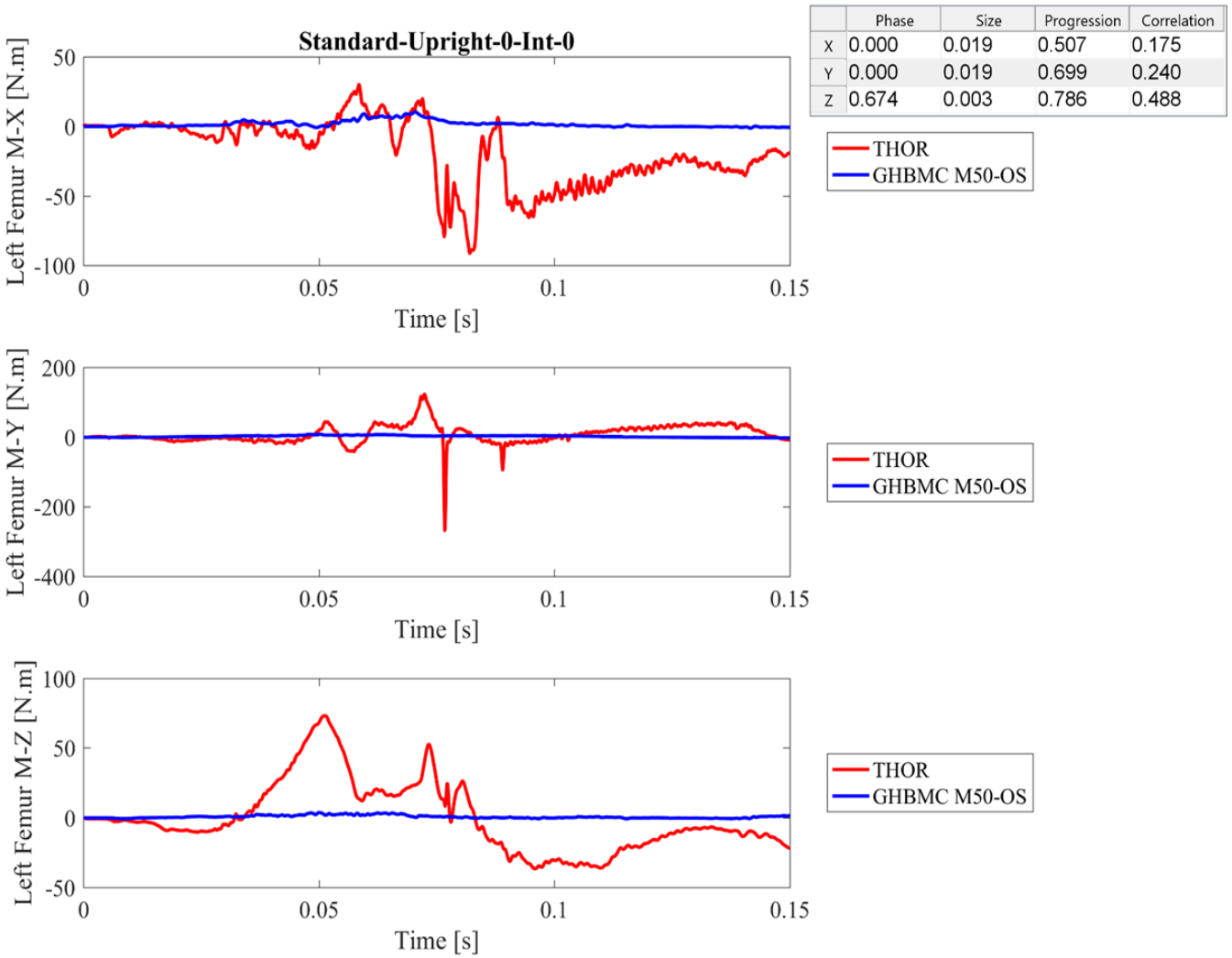

Figure 64. Comparison of left femur moment outputs between M50-OS and THOR.

The method used for the M50-OS lower extremity load cells **(Figure 65)** is a zero-length beam sandwiched between two rigid sections of the femur. The zero-length beam is intended as a load cell which measures the loads passing from one rigid part of the femur to the other. However, also connecting the two rigid femur parts is a shell cortical bone. This essentially shunts the load cell beam as it is modeled since this shell part is capable of bearing load and providing an alternative load path.

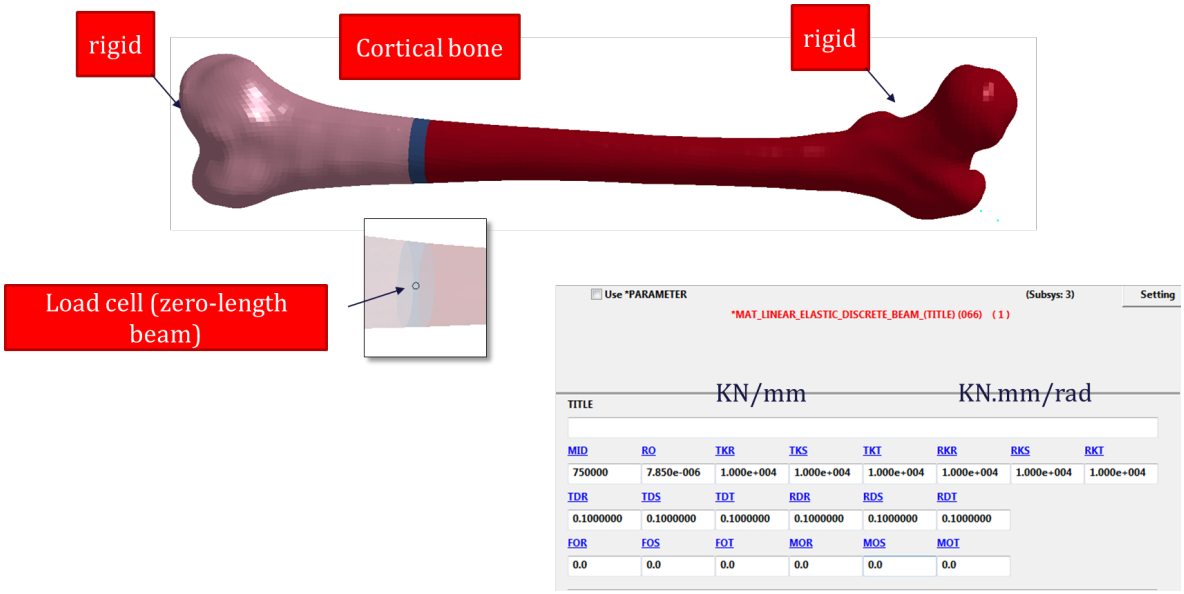

Figure 65. Lower extremity load cells as modeled in the M50-OS.

There are two solutions to this problem: (1) remove the cortical bone material from the femur, and replace the zero-length beam material card in the M50-OS model to that of the THOR FE model (the M50-OS model has this incorrectly modeled), or (2) remove the zero-length beam and measure the forces and moments in the femur through the cross-section of the cortical bone shells. Both methods provide similar femur moment magnitudes (**Figure 66** and **Figure 67**). However, the recommendation is to use the zero-length beam approach since a coordinate system for that load cell can be easily defined and be consistent with what is measured on the THOR. Using the cross-section approach results in an output in the global coordinate system.

Unfortunately, this issue was identified after all the M50-OS simulations were complete, so lower extremity moments are not accurate with the M50-OS model in this study.

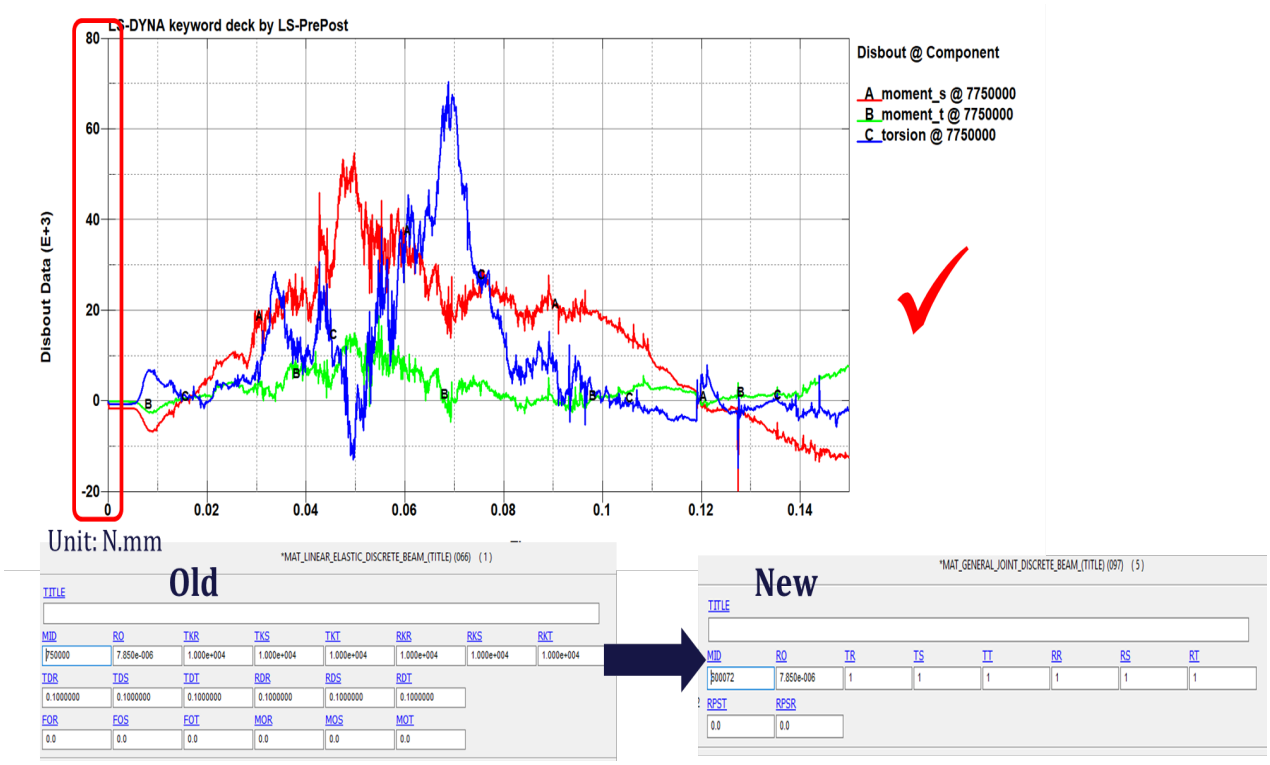

Figure 66. Eliminate cortical shell and update beam material to output femur moments from 0-length beam.

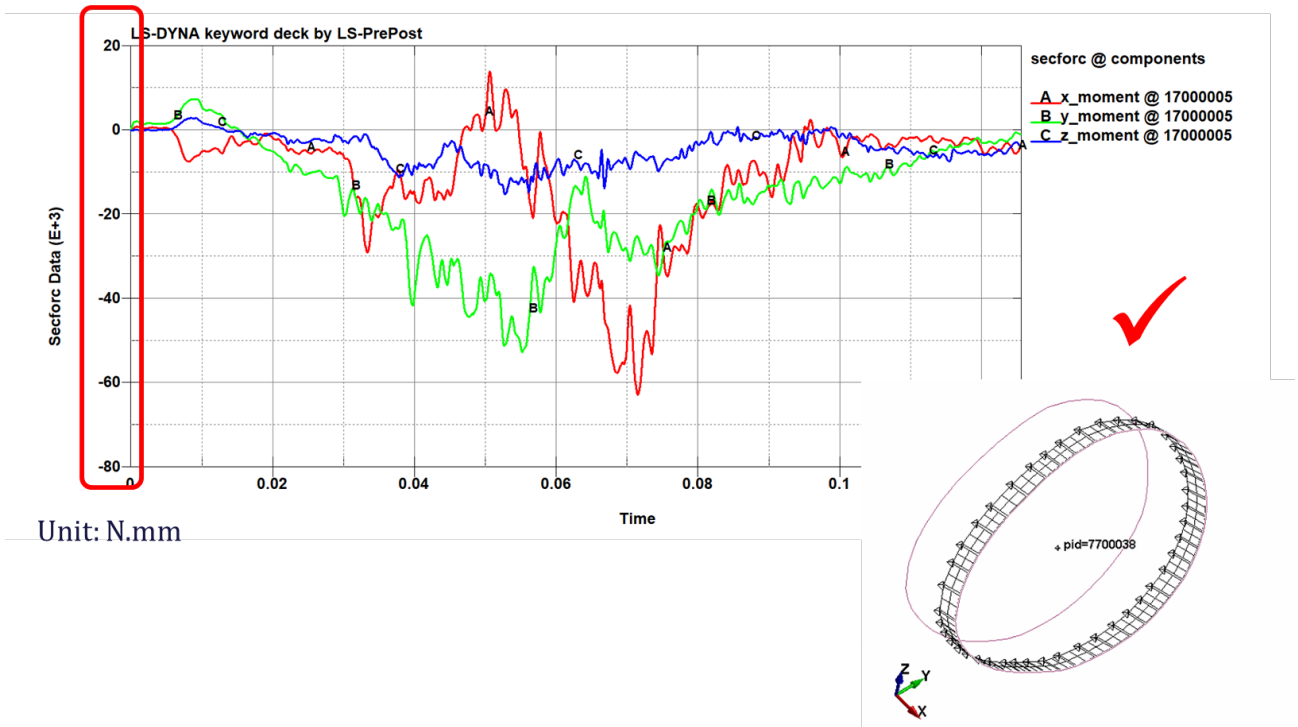

Figure 67. Eliminate zero-length beam load cell and output femur moments from cortical shell cross-section.

6 Parametric Simulation Suite

To facilitate rapid model generation, a parametric simulation suite was developed. The goal of this effort was to create a library of interconnected and complementing FE models that could be swapped with ease. Results of this effort are shown in **Figure 68**. The simulation suite was developed to allow simulations of full vehicle, and subsystem environments. The subsystem setup was used to shakedown and verify the implementation of all of the included components.

The simulation files included in the simulation suite were grouped by type. These groups included; vehicle (Camry model), subsystem (sled), RMDB, system, seat, occupant (THOR, M50-OS, M50-O), restraints (passenger air bag, curtain air bag, side air bag, standard and integrated seat belt), and group of files necessary to simulate all of the interactions among included models (**Figure 68**). In addition, a MATLAB script was developed to organize and handle all of the included FE models. This allowed for a rapid model generation, and batch processing of the input files and simulation results.

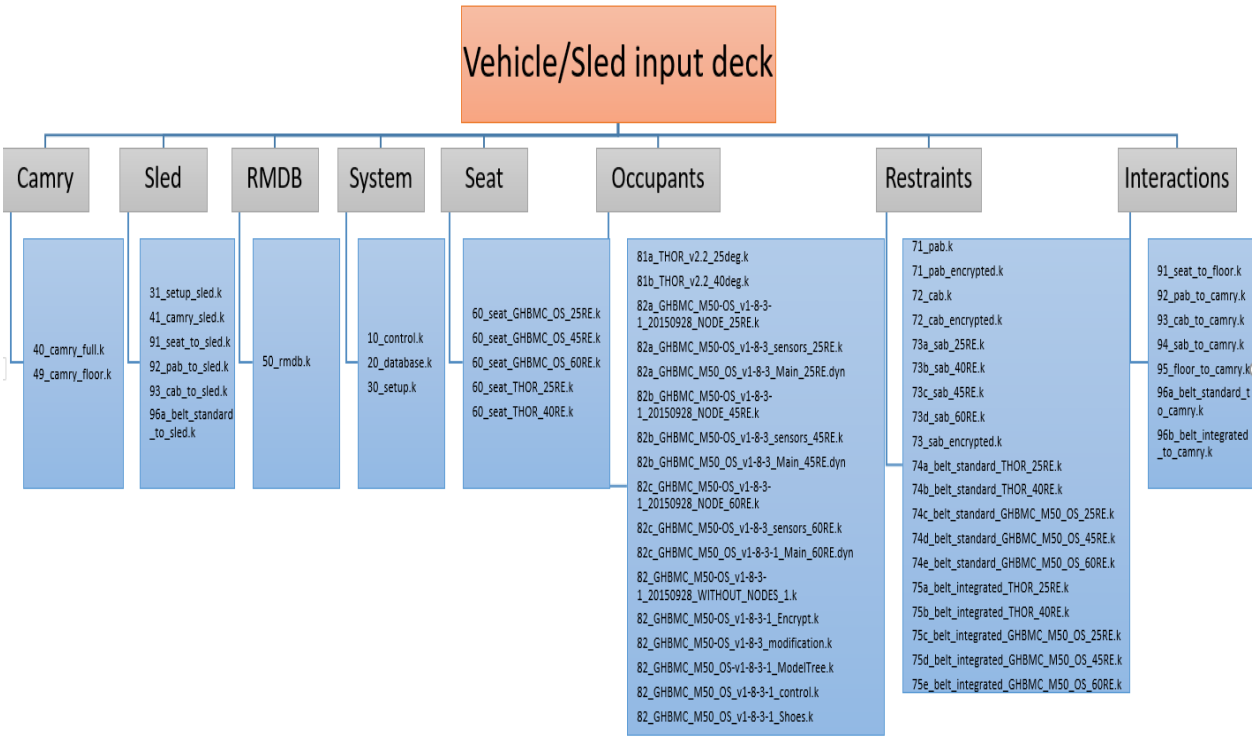

Figure 68. Parametric model suite structure.

7 Results Analysis

Given the large number of simulations conducted in this study, only a select number of cases will be presented in this report. All data will be provided in an appendix. We will present a complete detail of all error termination cases where the occupant model failed to reach the desired termination time.

7.1 Termination Results Summary

In general, the THOR and M50-OS models were stable in most seating positions (Table 8). The M50-OS model was most stable of all the occupant models (3/95 simulations ending in error), with THOR also being fairly stable (7/67 simulations ending in error). The M50-O model was more prone to stability errors, and over half of the simulations using this occupant model resulted in error (8/13 simulations ending in error). Out-of-range force or moment errors are typically associated with something "blowing up" in the model. Negative volume errors are associated with an element collapsing on itself, also often initially caused by an element "blowing up."

Table 8. Error analysis for all simulations performed in this study

Simulation	Termination Time	Reported error	Part responsible
THOR_Standard_Upright_0_Int_90	0.0562s	Out-of-range forces	Abdominal block
M50-OS_Standard_Reclined_0_Std_90	0.0713s	Out-of-range moments	Sacroiliac joint
M50-O_Standard_Upright_0_Int_0	0.075s	Out-of-range forces	Pelvis 3D skin
M50-O_Standard_Semireclined_0_Std_0	0.112s	Negative volume error	Neck muscle
M50-O_Standard_Reclined_0_Std_0	0.082s	Negative volume error	Abdomen muscle
M50-O_Standard_Reclined_0_Int_0	0.106s	Out-of-range forces	Neck muscle
THOR_Standard_Upright_180_Int_90	0.0382s	Out-of-range forces	Jacket
THOR_Standard_Upright_30_Int_150	0.128s	Out-of-range forces	Upper AB rear foam
THOR_Standard_Upright_30_Int_270	0.05s	Out-of-range forces	Upper AB rear foam
THOR_Standard_Upright_90_Int_150	0.0852s	Out-of-range forces	Upper AB rear foam
THOR_Standard_Upright_90_Int_180	0.096s	Out-of-range forces	Upper AB rear foam
THOR_Standard_Upright_90_Int_210	0.134ms	Out-of-range forces	Upper AB rear foam
M50-OS_Standard_Upright_90_Int_210	0.14s	Out-of-range forces	Thigh
M50-OS_Standard_Upright_90_Int_270	0.04s	Out-of-range moments	Sacroiliac joint
M50-O_Standard_Upright_30_Int_0	0.083	Out-of-range forces	Neck skin 3D
M50-O_Standard_Upright_90_Int_0	0.057	Out-of-range forces	Plevis 3D
M50-O Standard Upright_180_Int_0	0.105	Out-of-range forces	Foot skin
M50-O_Far_Upright_0_Int_30	0.120s	Negative volume	Neck muscle

7.1.1 Termination results for effect of seat recline

In general, the THOR and M50-OS models were stable in the reclined position. All but one THOR simulation ran to completion (31/32 normal terminations), and all but one M50-OS simulations ran to completion (47/48 normal terminations). The M50-O simulations were more prone to stability errors, and only two of six conditions that were simulated with this occupant model ran to completion.

For THOR_Standard_Upright_0_Int_90 case that is a far-side impact with upright seated THOR and integrated seat belt, the termination was recorded around 56ms. During the simulation the upper abdominal block was forced into the lower abdominal block, and as a result it sheared-off of the backing plate (**Figure 69**).

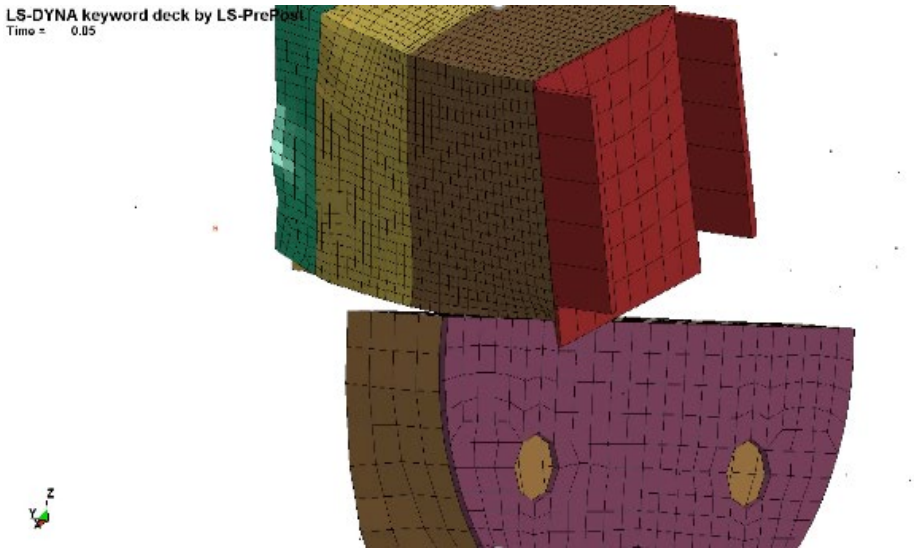

Figure 69. Error analysis for THOR_Standard_Upright_0_Int_90.

For M50-OS_Standard_Recline_0_Std_90 case that is a far-side impact with fully reclined M50-OS and standard seat belt, the error was recorded at 71ms. The early termination was a result of the sacroiliac joint failure (**Figure 70**).

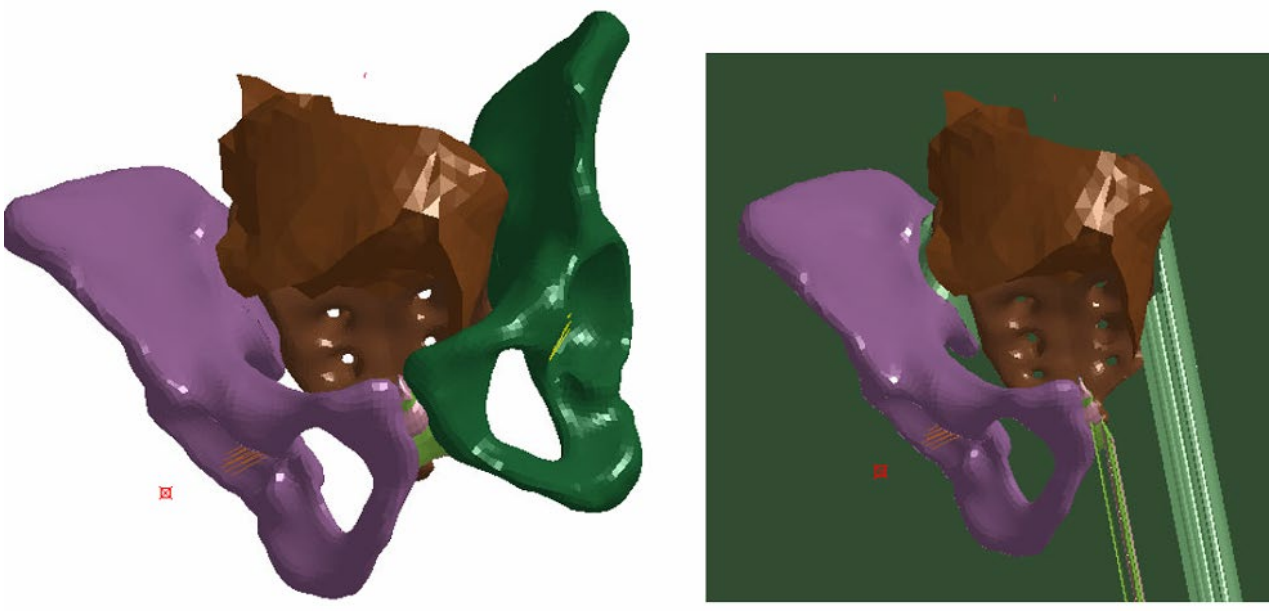

Figure 70. Error analysis for M50-OS_Standard_Recline_0_Std_90.

Considering the case of M50_O_Standard_Upright_0_Int_0 that is a frontal impact with upright seated M50-O and integrated seat belt, the error was recorded at t =75ms. A set of nodes out of range force from pelvis 3D skin (PID:18000015) caused the early termination (**Figure 71**).

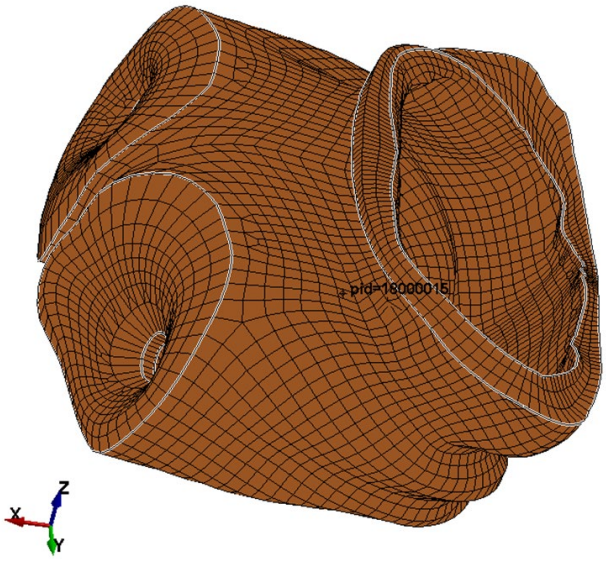

Figure 71. Error analysis for M50-O_Standard_Upright_0_Int_0.

For M50_O_Standard_Semireclined_0_Std_0 that is a frontal impact with semi-reclined seated M50-O and standard seat belt, the termination was recorded about 112ms with an error that is

negative volume in solid element from neck muscle (PID: 12100205) causing elements shooting out (**Figure 72**).

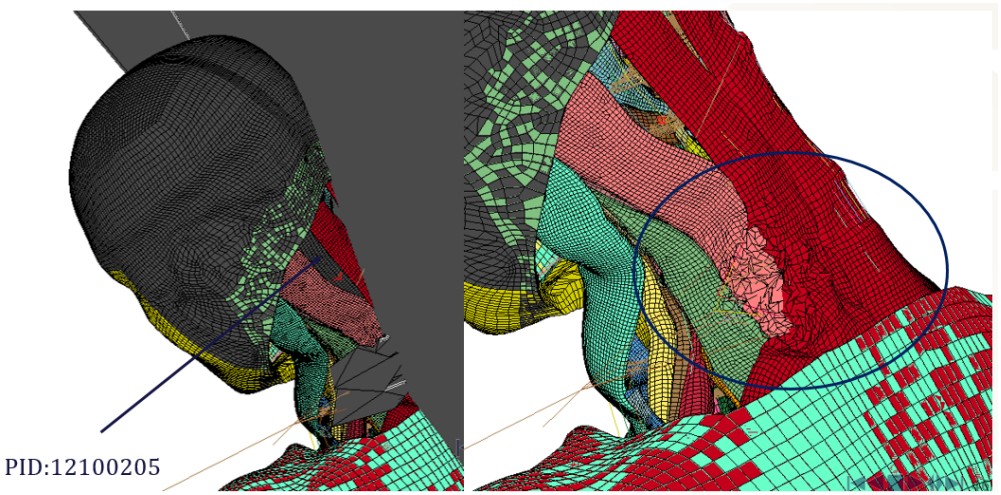

Figure 72. Error analysis for M50-O_Standard_Semireclined_0_Std_0.

For M50_O_Standard_Reclined_0_Std_0 that is a frontal impact with reclined seated M50-O and standard seat belt, the termination was recorded about 82ms with an error that is negative volume in solid element from abdomen muscle (PID: 12100205) (**Figure 73**).

Figure 73. Error analysis for M50-O_Standard_Recline_0_Std_0.

7.1.2 Termination results for effect of seat orientation

All but 6 THOR simulation ran to completion (26/32 normal terminations), and all but 2 M50-OS simulations ran to completion (30/32 normal terminations). Again, the M50-O simulations were more prone to stability errors, and only one of four conditions that were simulated with this occupant model ran to completion.

For THOR_Standard_Upright_0_Int_90 that is a far-side impact with upright seated THOR and the integrated seat belt, the error was traced back to the dummy jacket (**Figure 74**). For the cases of upright seated THOR with 30° seat rotation and integrated seat belt under impacts of near side and 150°, the error resulted from the upper abdominal foam block (**Figure 75**). Similarly, the cases of upright seated THOR with 90° seat rotation and integrated seat belt under impacts of far side, rear side, and 150° terminated due to instability in the upper abdominal foam block (**Figure 76**).

For M50-OS_Standard_Upright_90_Int_210, distortion of the flesh mesh into the femur led to the failure of the simulation at t=140ms (**Figure 77**). For the M50-OS_Standard_Upright_ 90_Int_270 simulation, the error was the result of the failure of the sacroiliac joint where the elements went unstable under a large compressive load (**Figure 78**).

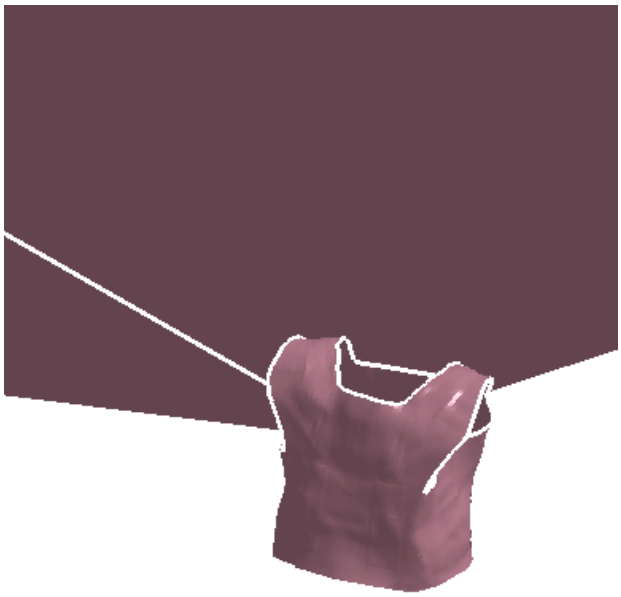

Figure 74. Error analysis for THOR_Standard_Upright_0_Int_90.

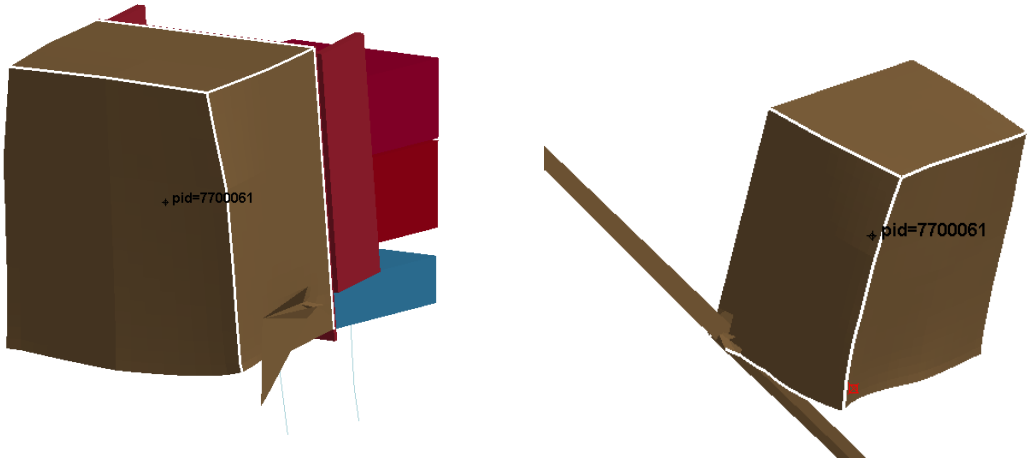

Figure 75. Error analysis for THOR_Standard_Upright_30_Int_150/270.

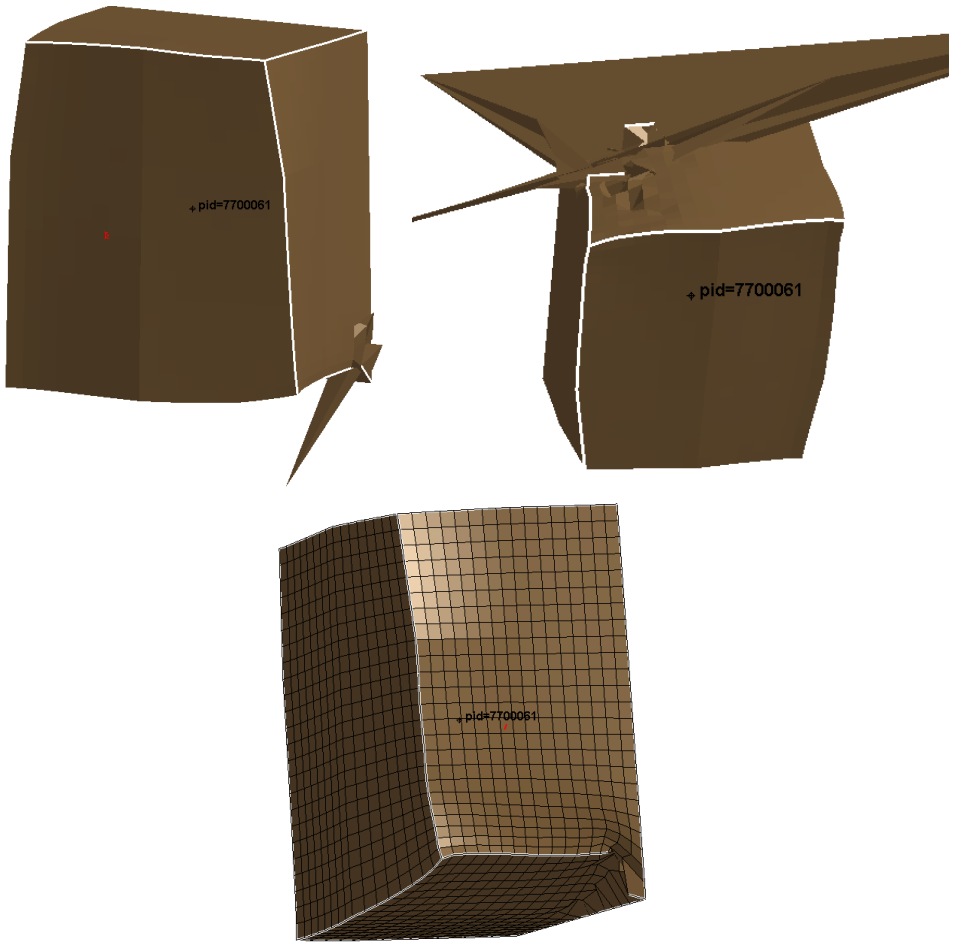

Figure 76. Error analysis for THOR_Standard_Upright_90_Int_150/180/210.

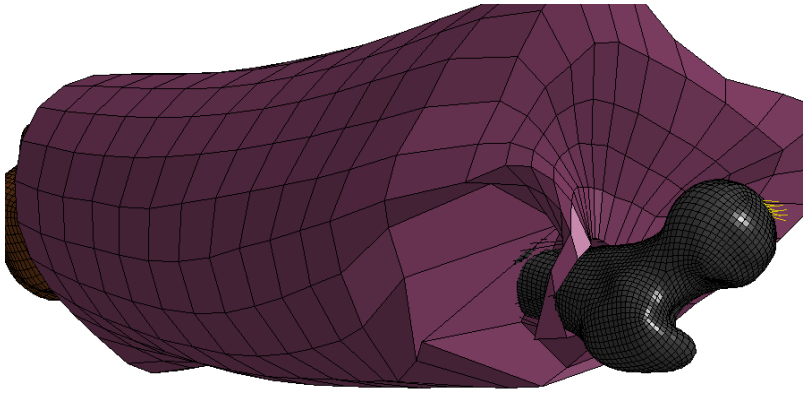

Figure 77. Error analysis for M50-OS_Standard_Upright_90_Int_210.

Figure 78. Error analysis for M50-OS_Standard_Upright_90_Int_270.

Figure 79 displays errors of case M50_Standard_Upright_30_Int_0 that is a frontal impact with 30° rotation, upright M50-O with the integrated seat belt, with the error recorded at t = 83ms. The error is due to a set of nodes of 3D neck muscle bearing out of range forces.

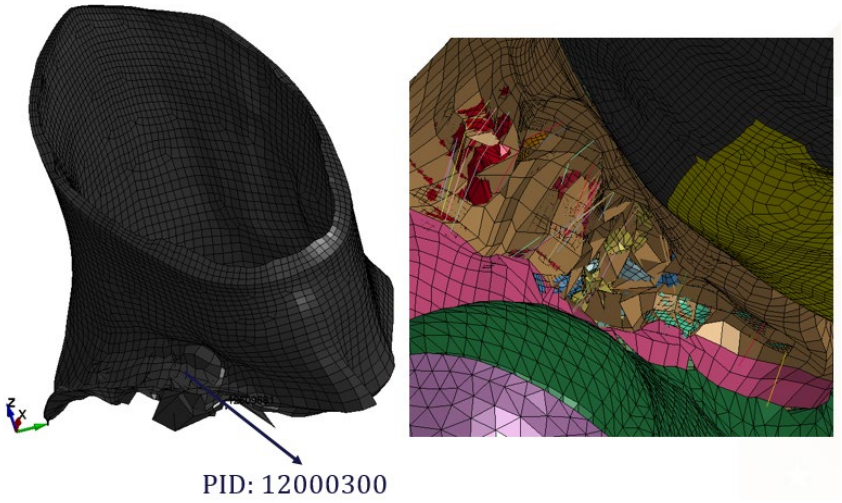

Figure 79. Error analysis for M50-O_Standard_Upright_30_Int_0.

For the case of M50_Standard_Upright_90_Int_0 that is a frontal impact with 90° rotation, upright M50-O and integrated seat belt, the error was recorded at t = 75ms that resulted from a set of nodes on pelvis 3D (PID: 18000018) (**Figure 80**).

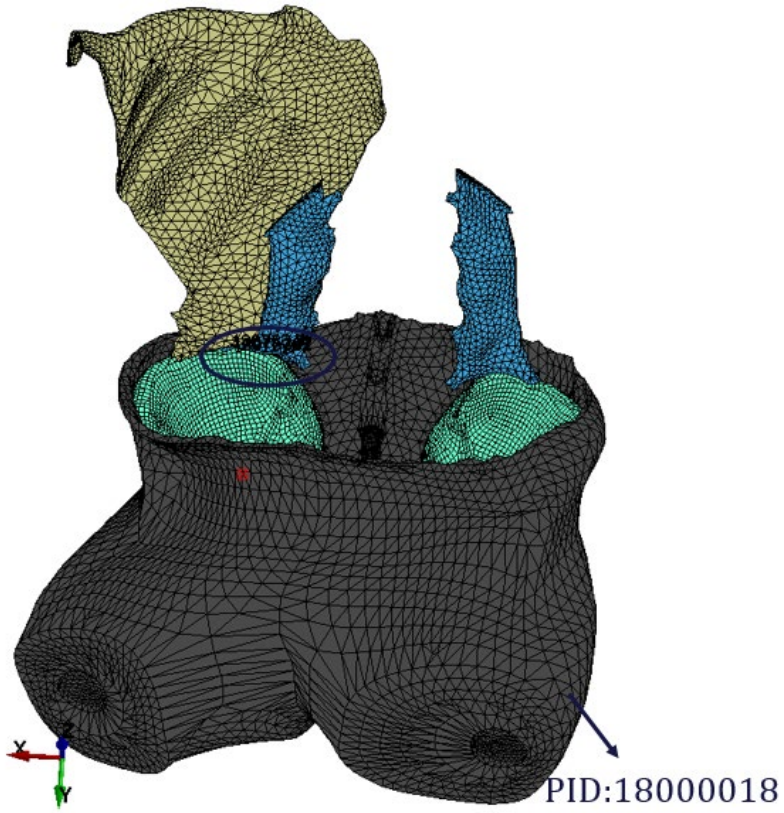

Figure 80. Error analysis for M50-O_Standard_Upright_90_Int_0.

For the case of M50_Standard_Upright_180_Int_0 that is a frontal impact with 180° rotation, upright M50-O and integrated seat belt, the error was recorded at t = 105ms that resulted from a set of nodes on left foot skin (PID: 17000901) (**Figure 81**).

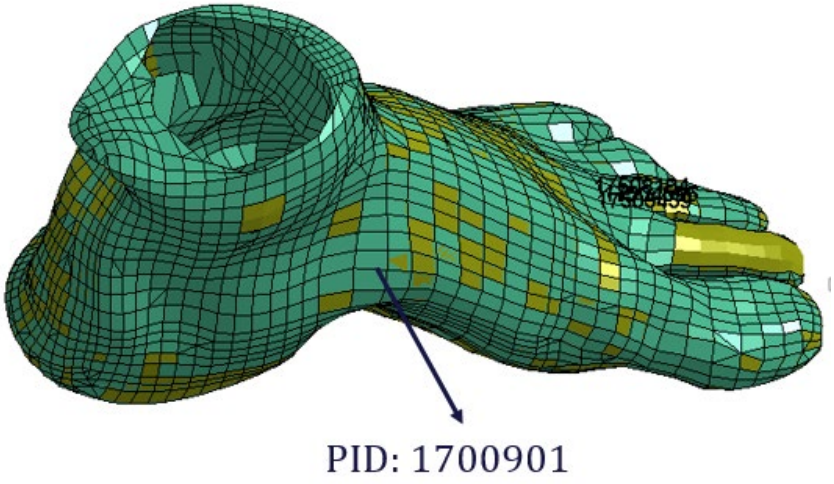

Figure 81. Error analysis for M50-O_Standard_Upright_180_Int_0.

7.1.3 Termination results for torso turn

7.1.4 All three simulations using the M50-OS model terminated normally. Termination results for effect of having occupant sleeping on the belt

All nine simulations using the M50-OS model terminated normally terminated.

7.1.5 Termination results for effect of having occupant seated far back from instrumentation panel

All but one simulation using the THOR, M50-OS and M50-O models terminated normally. In the case of M50-O_Far_Upright_0_Int_30_RMDB, which is a far side oblique impact, forward facing, and upright seated in an integrated seat belt, the error in M50-O was recorded at t = 120ms that resulted from negative volume in solid elements from the neck muscle part with PID 12100211 (**Figure 82**).

Figure 82. Error analysis for M50-O_Far_Upright_0_Int_30.

7.2 Select Frontal Impact Results

7.2.1 Upright seated, front-facing, standard seat belt (THOR versus M50-OS)

At first, a comparison was made between upright M50-OS and THOR FE in nominal position. (**Figure 83**).

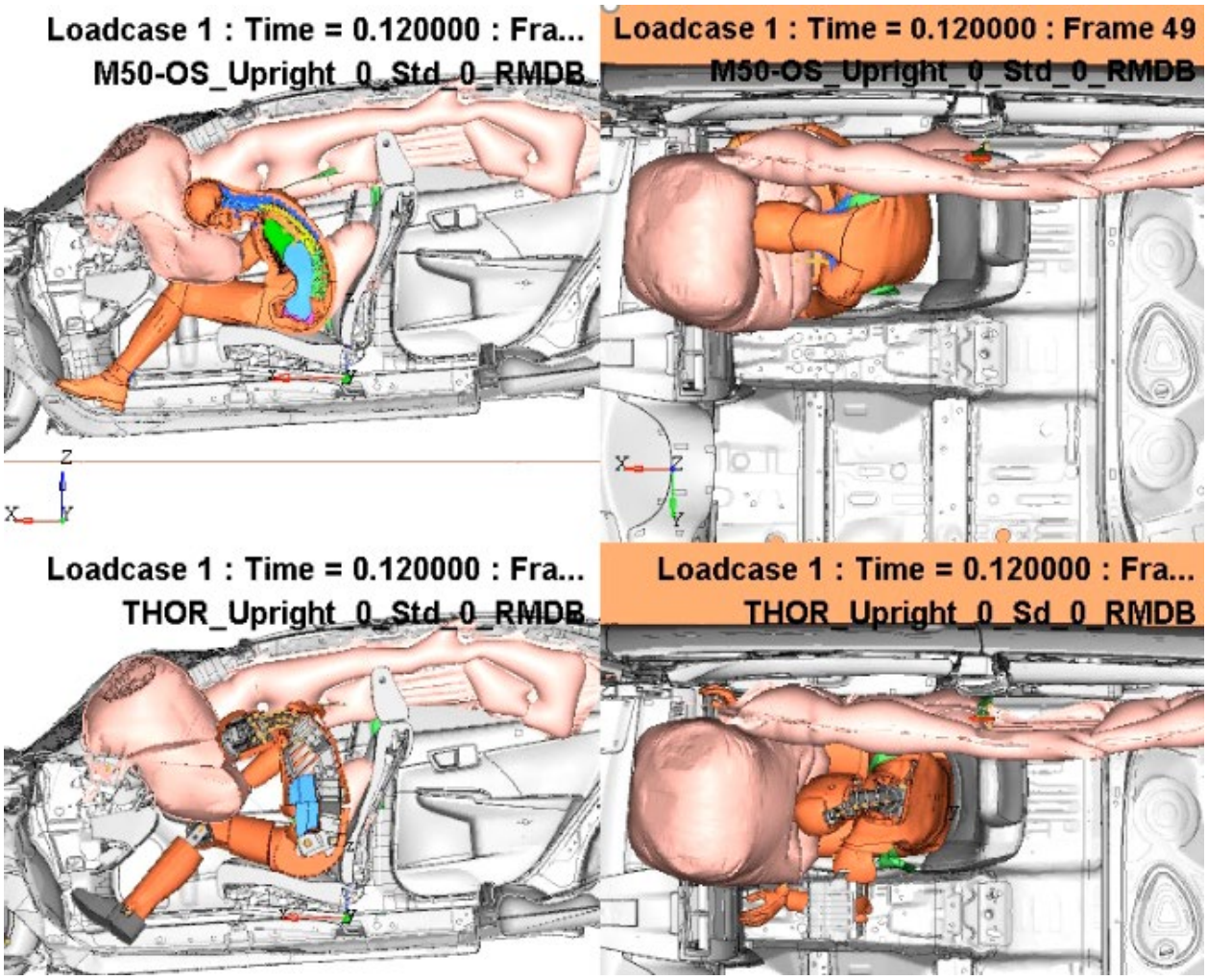

Figure 83. Upright_0_Std_0_RMDB for M50-OS/THOR at t=0.12s.

Figure 84 and **Figure 85** show the belt to occupant forces recorded from the FE simulations. These are the contact forces (including friction) between the occupants and the belts, and not belt tensile forces that would be commonly recorded during vehicle and sled testing. Figure 84 shows lap belt forces recorded for THOR and M50-OS. Both outputs are very close to each other but force recorded for THOR FE is slightly higher. Figure 85 shows the shoulder belt to occupant force, which are also comparable between THOR and M-50-OS simulations. THOR FE shoulder belt force is slightly higher at the peak, but it drops down earlier than the force recorded for M50-OS. The analysis of the occupant kinematics was used to explain the observed differences in the seat belt engagement (Figure 83). Figure 83 shows the simulation results at 120ms after the initial impact. The M50-OS shows a larger forward excursion of the torso than THOR FE model. Additionally, M50-OS exhibits a noticeable flexion in the lumbar and thoracic spine, whereas the THOR remains more upright limiting the torso forward motion. This difference in the torso kinematics is a possible explanation of the differences in the recorded belt engagement.

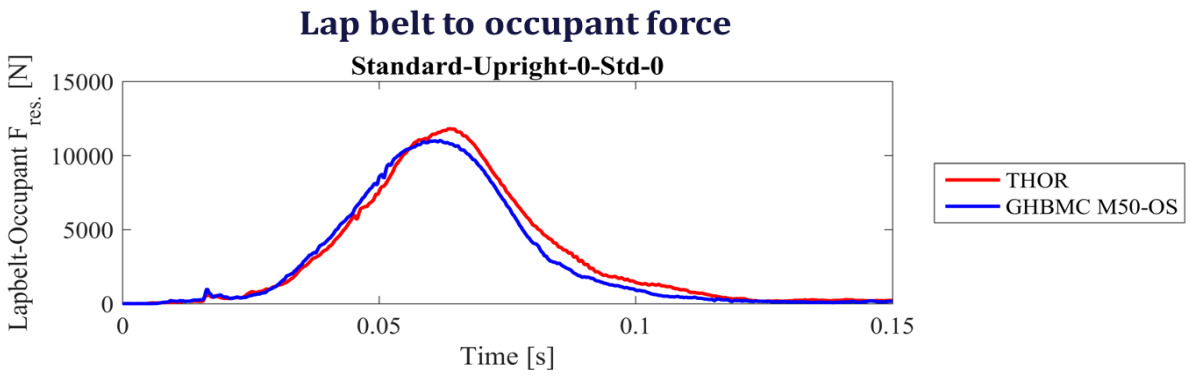

Figure 84. Lap belt to occupant force.

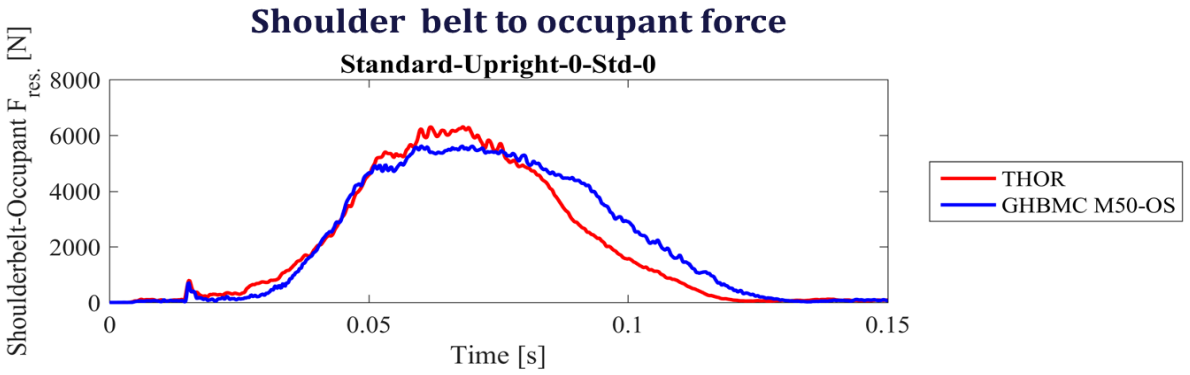

Figure 85. Shoulder belt to occupant force.

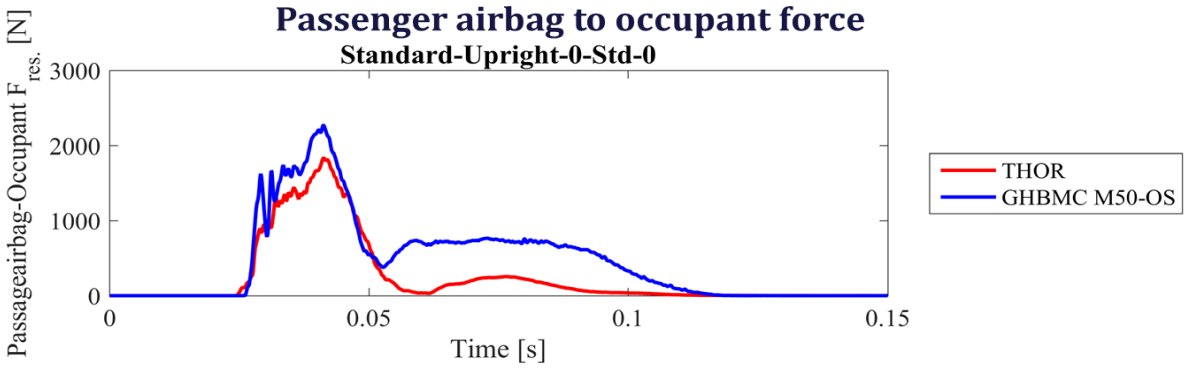

Figure 86. Passenger air bag to occupant force.

Figure 87 shows the occupant to seat cushion and seatback force respectively, with the seat cushion force recorded for THOR FE model being higher than the force recorded for M50-OS. A detailed analysis of the simulation video revealed a substantial difference in pelvis trajectory between the two models. THOR FE model with its relatively stiff pelvic flesh was driven into the seat and engaged the anti-submarining bar located below the cushion. However M50-OS model, whose pelvic flesh was observed to be softer than the flesh of THOR FE model, was driven down into the seat, compressed and sheared the pelvic flesh over the anti-submarining bar (**Figure 83**).

Figure 88 shows the comparison of the head angular velocity recorded for both occupants. Both signals remain comparable until 60ms of the recorded event. At 60ms THOR FE model recorded a spike in the y and z signal of the angular velocity. A detailed review of the simulation video revealed that this was due to the THOR having a head-to-roof impact during the forward excursion of the occupant. This impact was not observed for the M50_OS model.

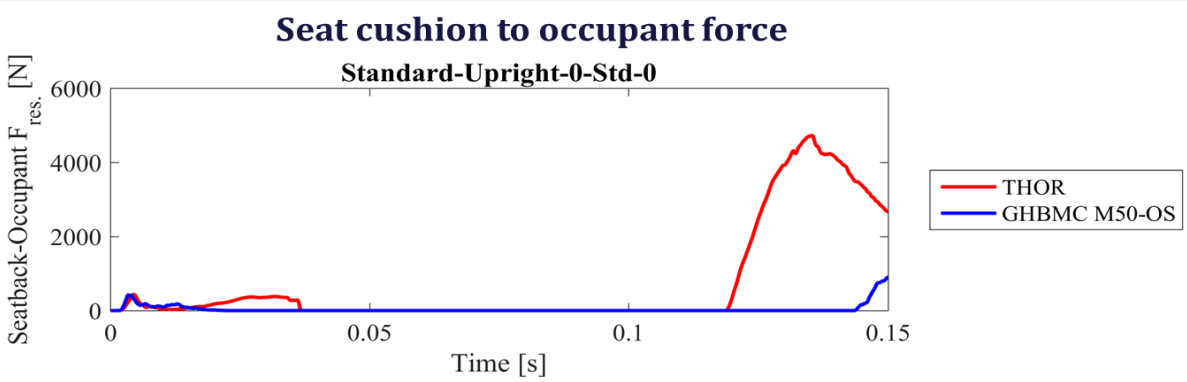

Figure 87. Seat cushion to occupant force.

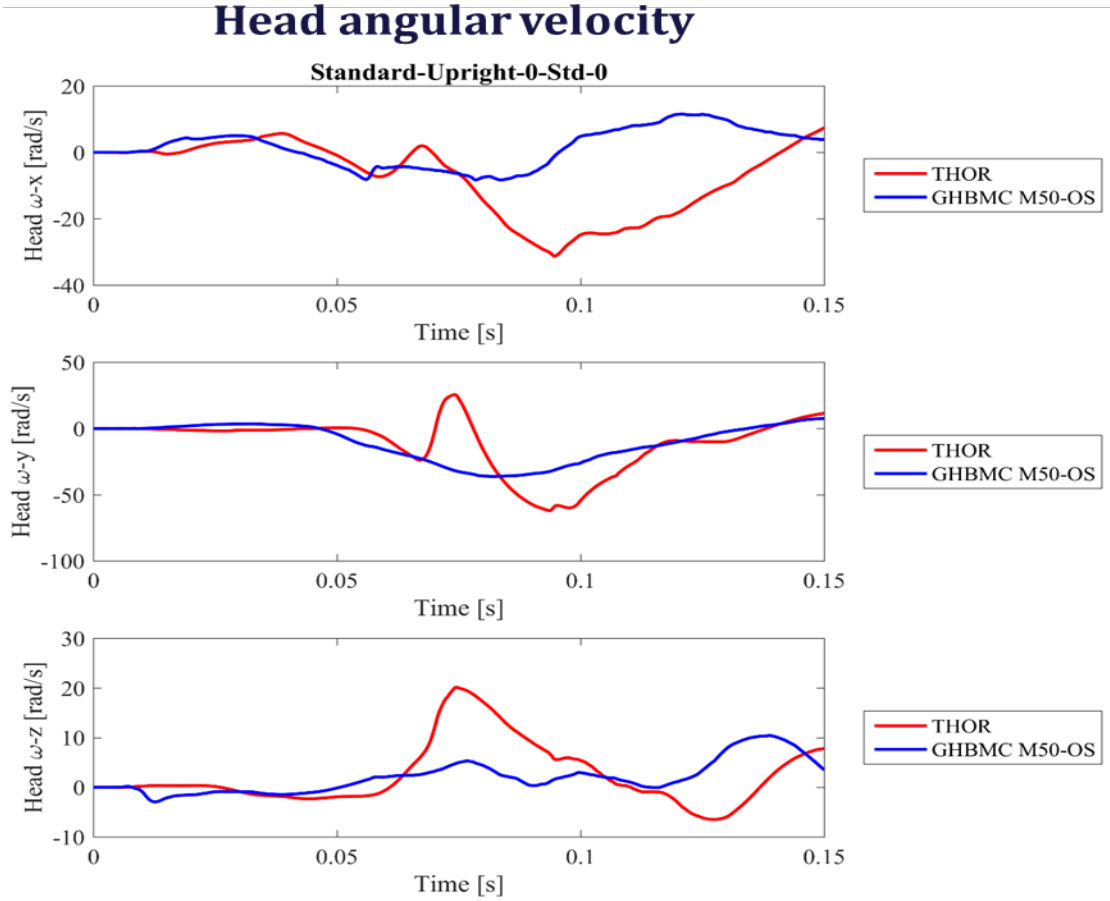

Figure 88. Head angular velocity.

Figure 89 shows the comparison of the pelvis rotation in the sagittal plane between the two models. The positive Y rotation of the pelvis represents a forward motion of the top of the pelvis, negative represents the backward motion of the top of the pelvis. The two models showed completely opposite pelvis rotation in the sagittal plane. While THOR showed a positive Y rotation throughout the entire simulation, M50-OS moved in the opposite direction and reached an extremum of -16° Y rotation at 65ms. The differences in pelvis motion between the occupants can be explained by several factors. First, as described above, the differences in the flesh stiffness keep the THOR pelvis within the loading path of the lap belt, whereas M50-OS compresses its pelvis flesh that results in a dropped pelvis position during the lap belt engagement. Second, due to the articulated nature of the M50-OS spine, its pelvis is allowed to rotate backwards while the occupant's upper torso pitches forward. Since THOR is equipped only with two compliant joints in the thoracic and lumbar spine it is not capable of mimicking the continuous flexion of the spine observed in the M50-OS model. This results in a stiffer coupling between the lumbar spine and the pelvis. This coupling forces THOR's pelvis into positive rotation while the occupant pitches forward.

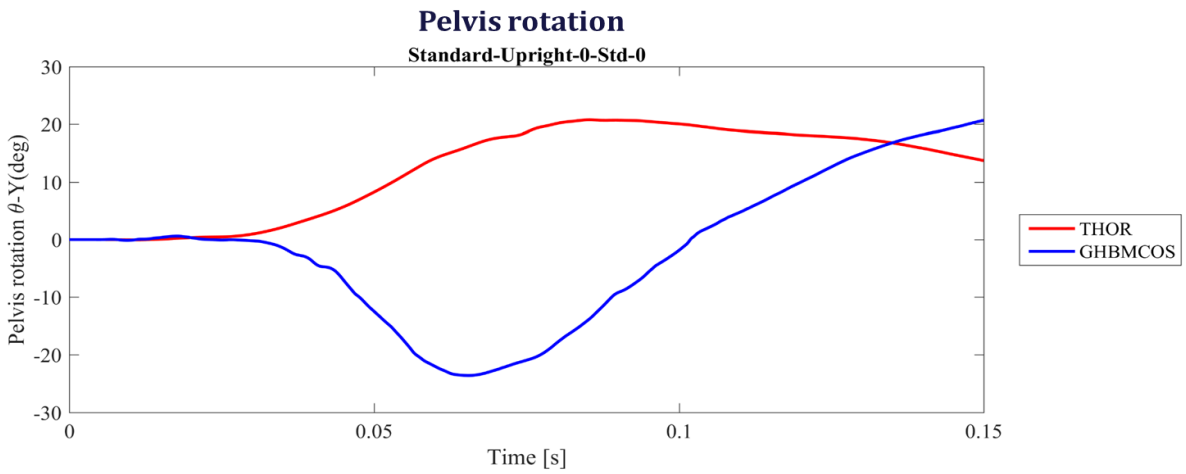

Figure 89. Pelvis rotational displacement about Y axis.

7.2.2 Upright seated, front-facing, integrated seat belt (THOR vs M50-OS)

Comparing the results obtained from the Upright_0_Int_0 for M50-OS/THOR, which is the same load cases as presented in Section 8.2.1 but with an integrated seat belt (Figures 90 – 96), shows that there is little difference between the integrated belt and standard belt in this configuration. Since both types of seat belts provide a good belt fit for the upright occupant, their results were expected to be similar. All of the conclusions made for the upright, frontal cases with standard belt are applicable to the integrated belt configuration.

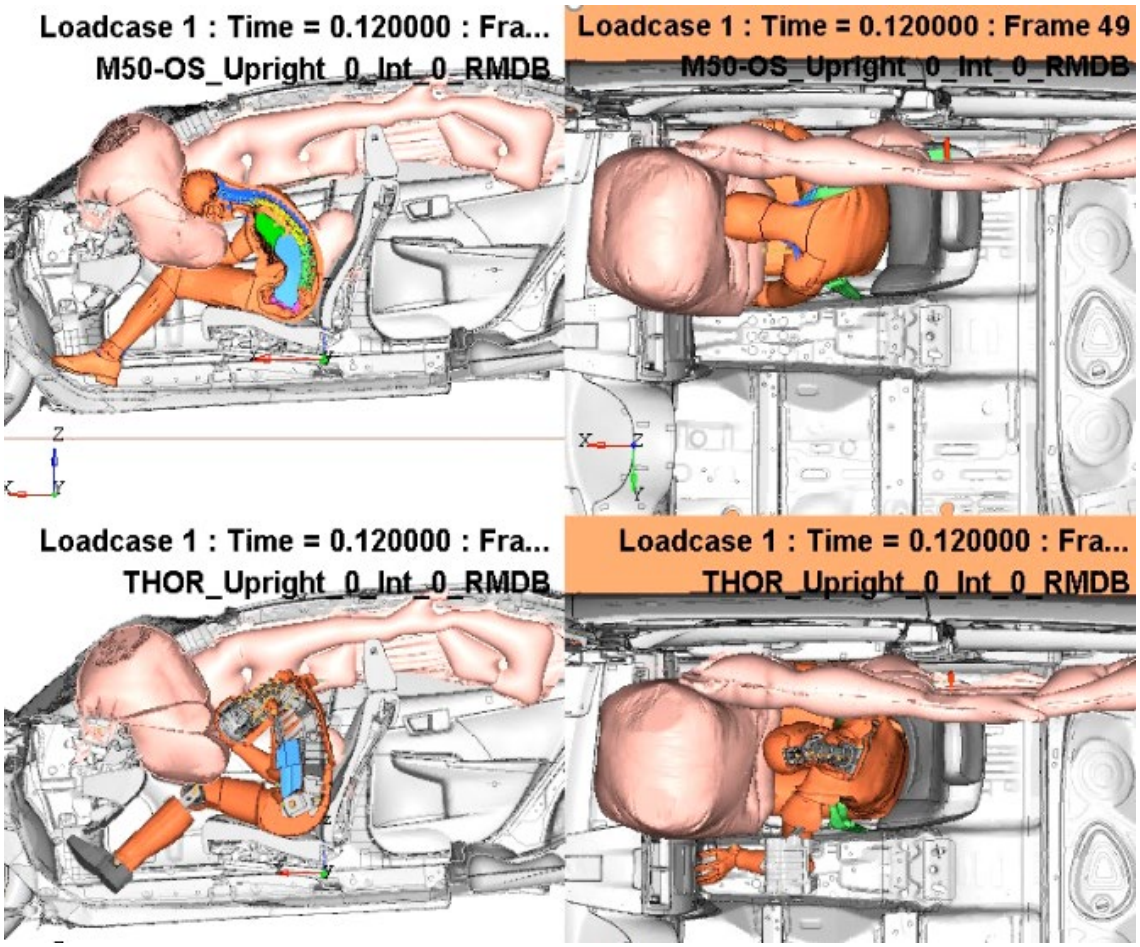

Figure 90. Upright_0_Int_0_RMDB for M50-OS/THOR.

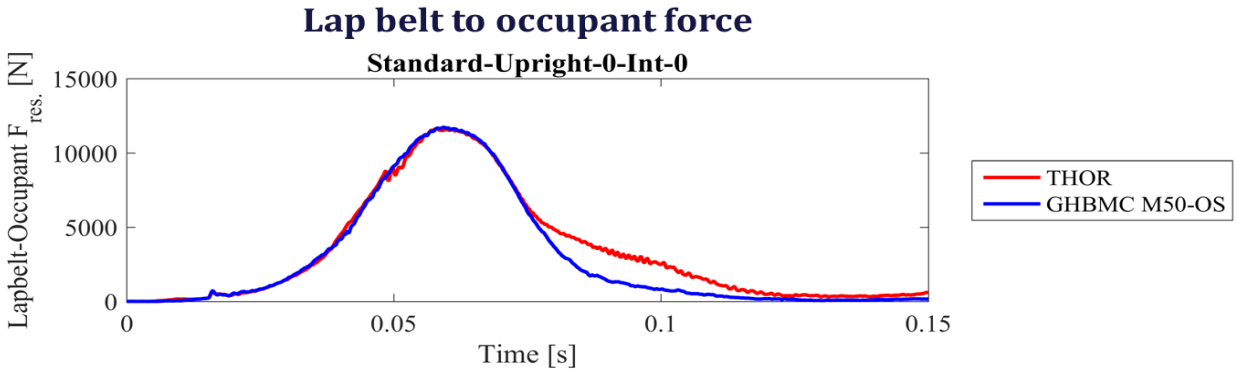

Figure 91. Lap belt to occupant force.

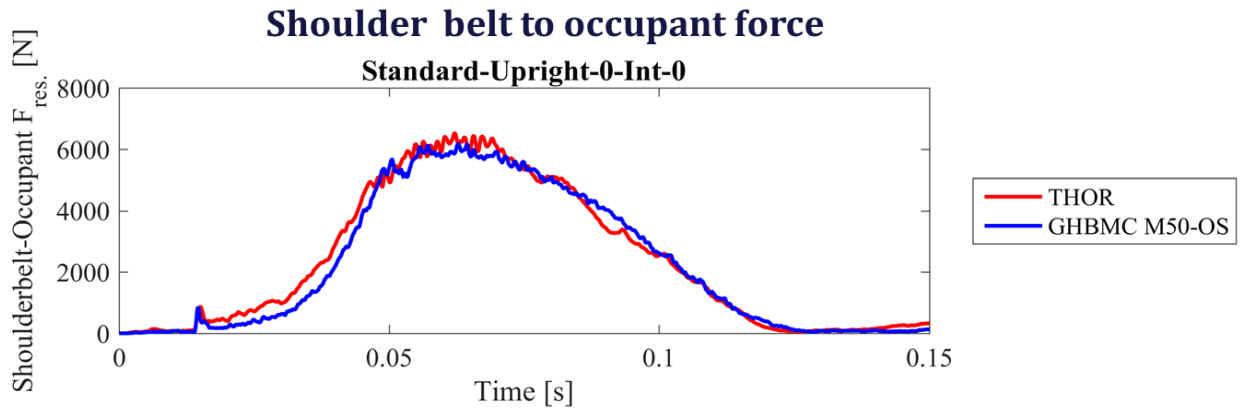

Figure 92. Shoulder belt to occupant force.

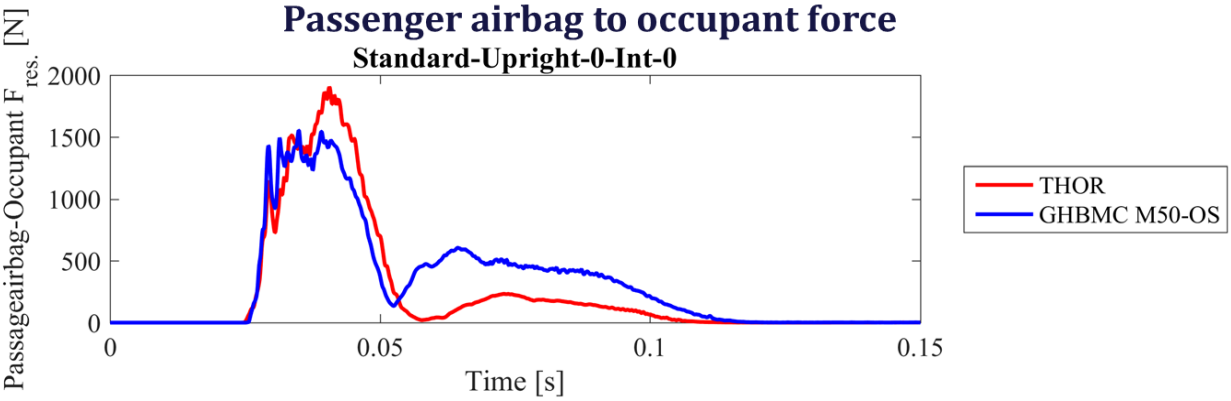

Figure 93. Passenger air bag to occupant force.

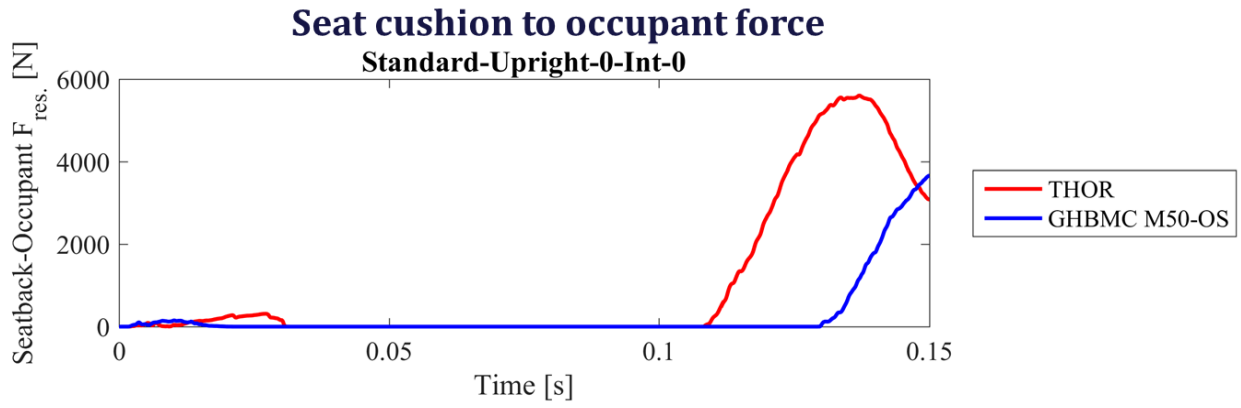

Figure 94. Seat cushion to occupant force.

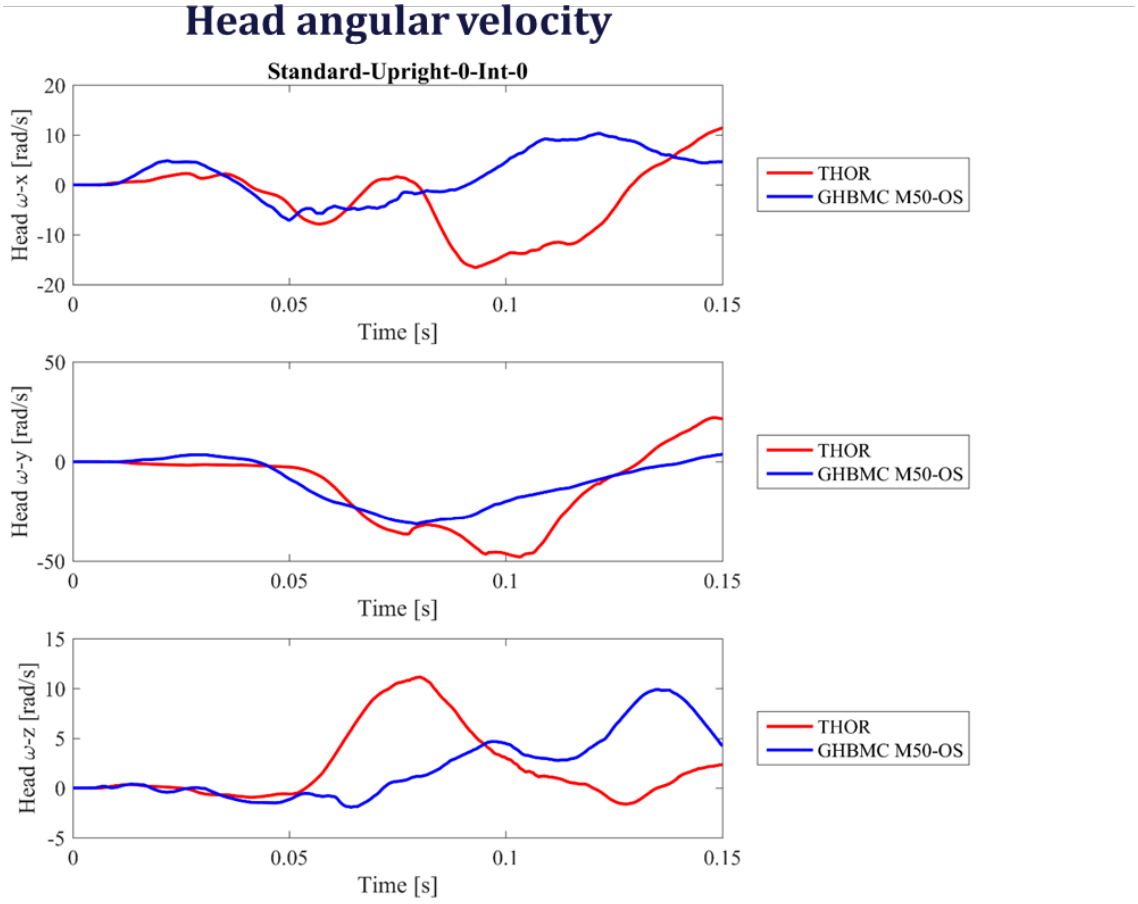

Figure 95. Head angular velocity.

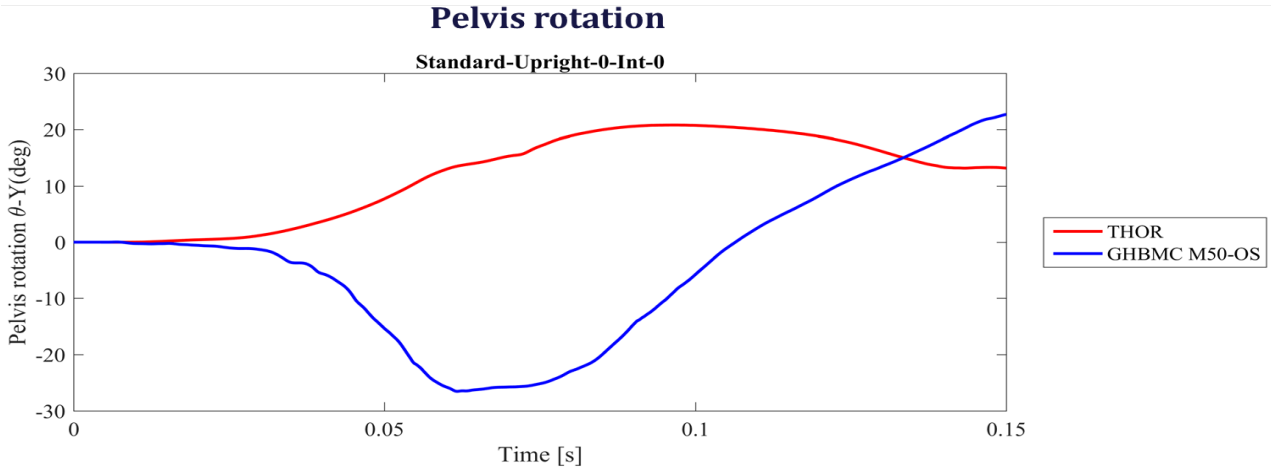

Figure 96. Pelvis rotational about Y axis.

7.2.3 Semi-reclined seated, front-facing, standard seat belt (THOR versus M50-OS)

Figure 97 shows the visual comparison between the THOR and M50-OS simulation results at 120ms. The figure shows occupants in a semi-reclined position with a standard seat belt in the frontal impact condition. It should be noted that due to model limitations, THOR was reclined only to 40°, whereas M50-OS was reclined to 45°.

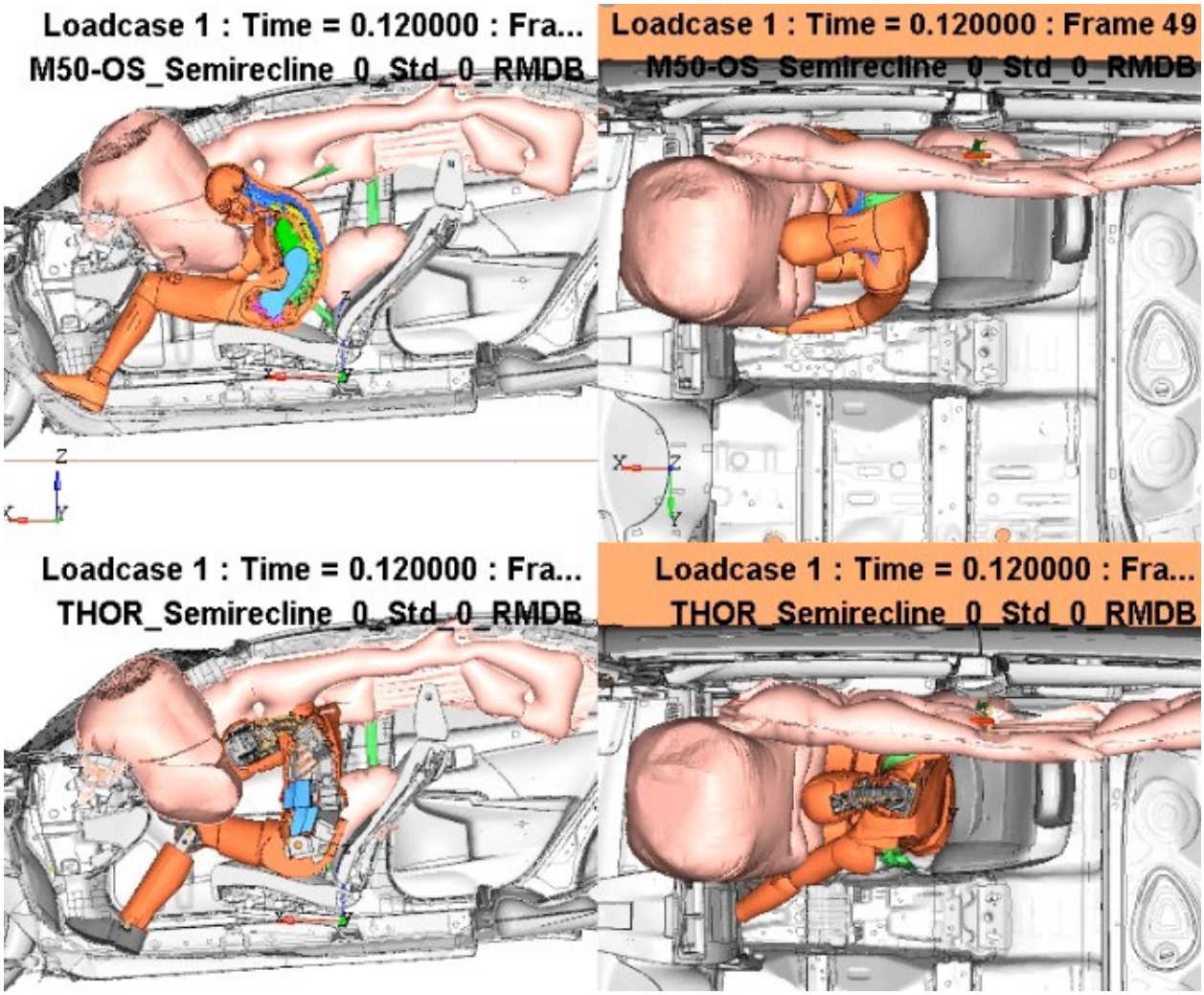

Figure 97. Semireclined_0_Std_0_RMDB for M50-OS/THOR.

Figure 98 shows a comparison of lap belt to occupant forces recorded from the simulations. THOR lap belt contact force was higher when compared with the M50-OS; however, the shoulder belt forces remained comparable between the two models (**Figure 99**). Comparing the shoulder belt forces recorded for the upright (**Figure 85**) and semi-reclined (**Figure 99**) occupant positions, one can notice a slight delay in shoulder belt engagement for the semi-reclined occupants. This is due to the fact that occupants in a semi-reclined position are initially located further away from the standard shoulder belt and engage it later than upright occupants.

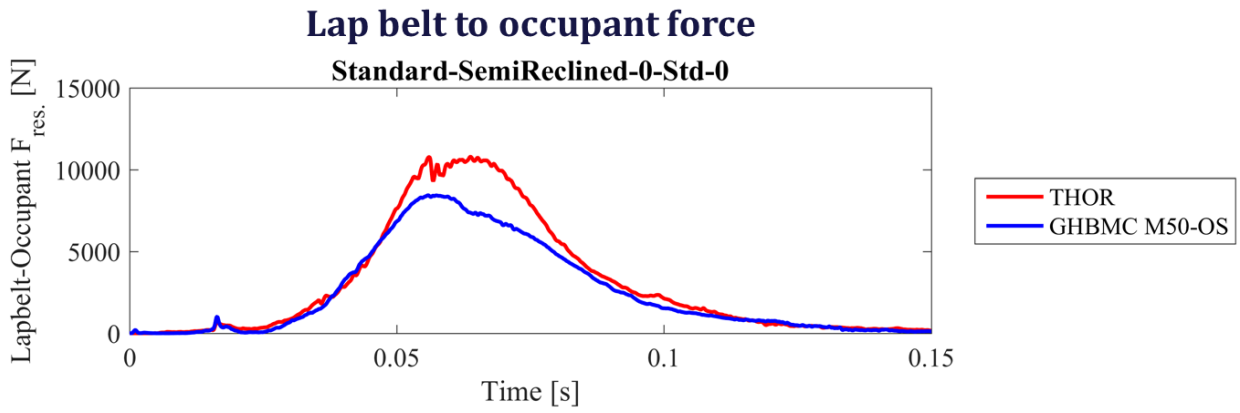

Figure 98. Lap belt to occupant force.

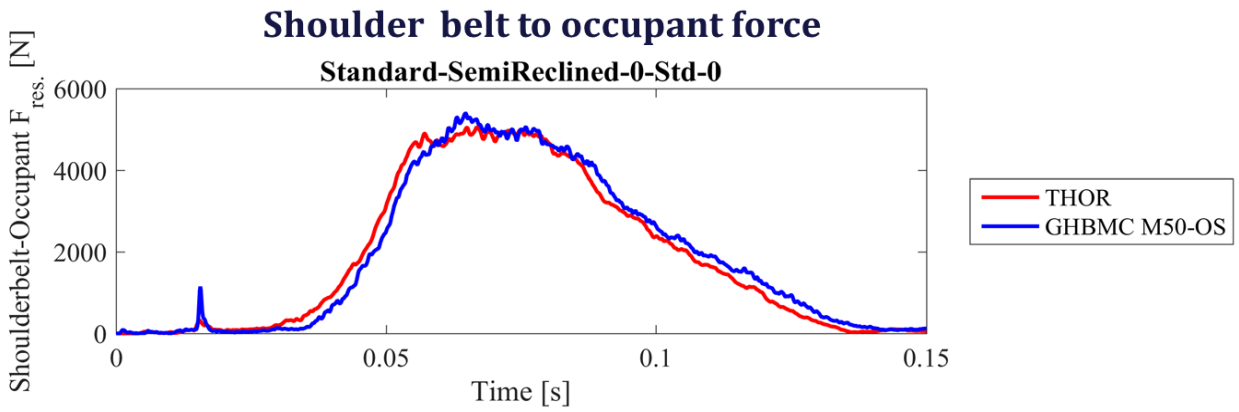

Figure 99. Shoulder belt to occupant force.

The recorded passenger air bag to occupant force (**Figures 100**) shows higher peak value for M50-OS than for THOR FE model. As discussed above, since THOR's spine incorporates only 2 compliant joints, it is not capable of mimicking the continuous flexion of the spine observed in the M50-OS model. This results in a reduced forward excursion for THOR and lower force in the passenger air bag engagement.

For head angular velocity (**Figure 101**), the responses recorded for THOR and M50-OS are similar. The Y axis angular velocity, which is the largest in the magnitude, matches well between the models. The X and Z measures show some discrepancies between the models. However. they are substantially smaller in magnitude.

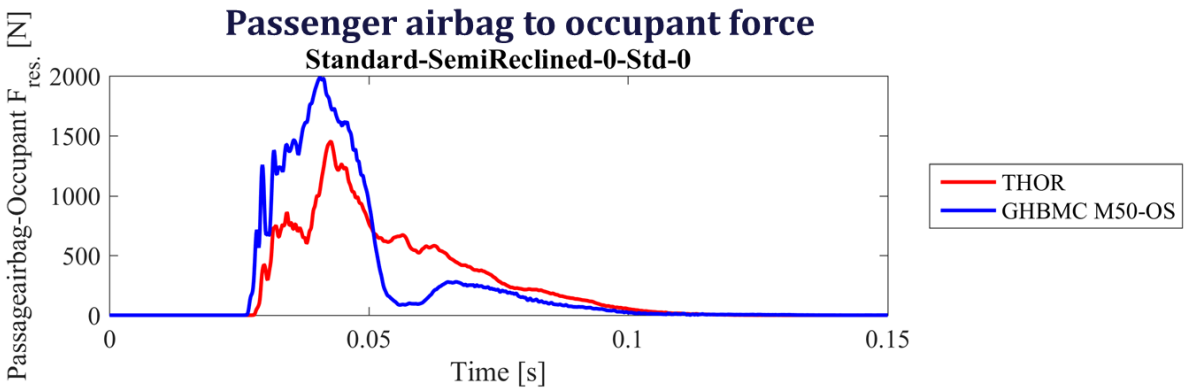

Figure 100. Passenger air bag to occupant force.

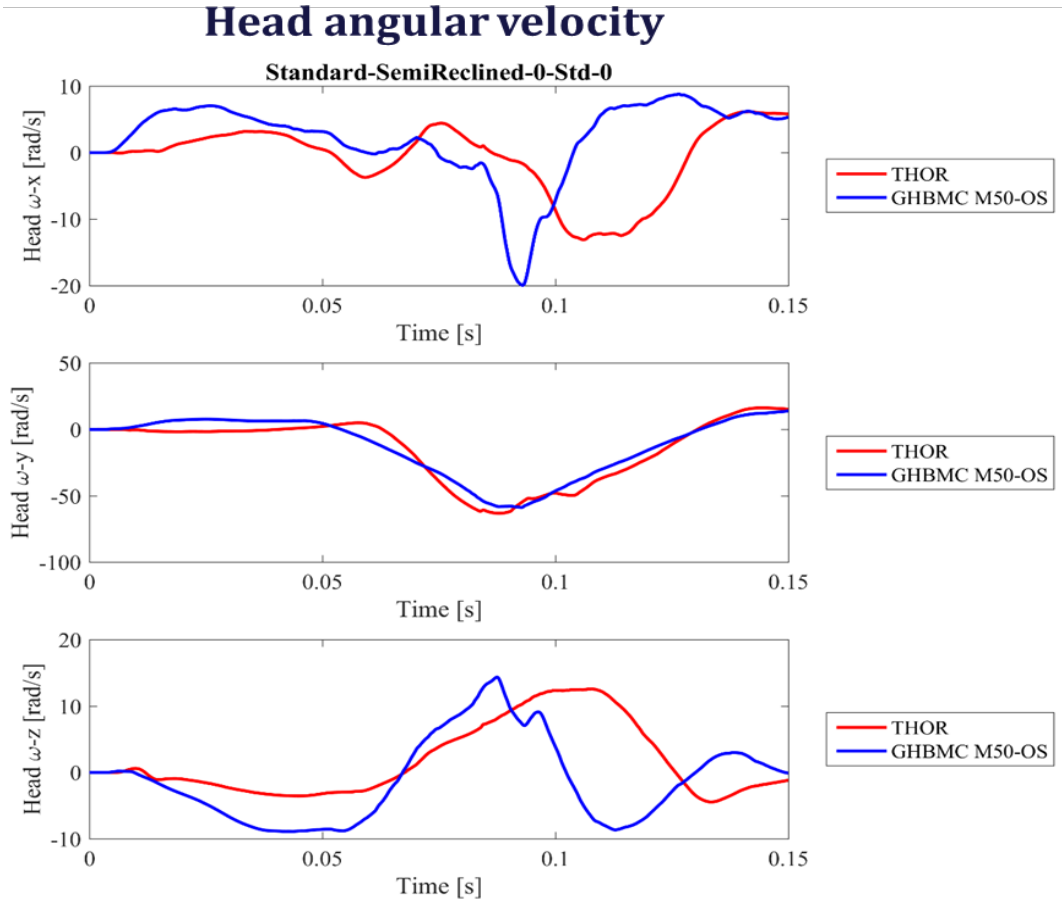

Figure 101. Head angular velocity.

The analysis of the pelvis rotation yields similar conclusions as for the upright cases. **Figure 102** shows the comparison of the pelvis rotation in the sagittal plane between the two models. The two models showed completely opposite pelvis rotation in a sagittal plane. While THOR showed a positive Y rotation throughout most of the entire simulation, M50-OS moved in the opposite

direction. The differences in pelvis motion between the occupants can be explained by several factors. First, due to initial position of the M50-OS model, the lap belt did not engage the occupant's pelvis and slid up into the abdomen. This belt load led to an observed flexion of the lumbar spine and resulted in backwards (negative) rotation of the pelvis.

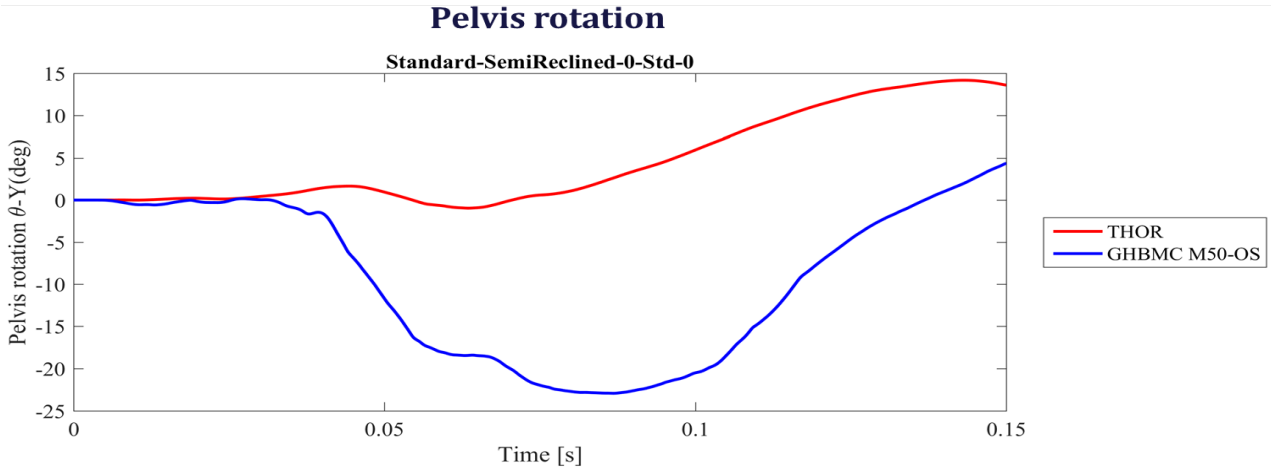

Figure 102. Pelvis rotational about Y axis.

Considering pelvis rotation about the Y axis (**Figure 102**), during the loading process, THOR anteriorly rotated about Y. Since the pelvis flesh is pretty stiff, it makes it hard for the pelvis to overcome the substantial shear force to have posterior rotation. However, for M50-OS, it had a lot of posterior rotation because the pelvis flesh deformed a lot and there's quite some room between the pelvis and flesh that allows the pelvis to rotate posteriorly.

7.2.4 Semi-reclined seated, front-facing, integrated seat belt (THOR versus M50-OS)

Figure 103 shows the visual comparison between the THOR and M50-OS simulation results at 120ms. The figure shows occupants in a semi-reclined position with an integrated seat belt in the frontal impact condition. It needs to be reiterated that due to model limitations THOR FE was reclined only to 40°, whereas M50-OS was reclined to 45°.

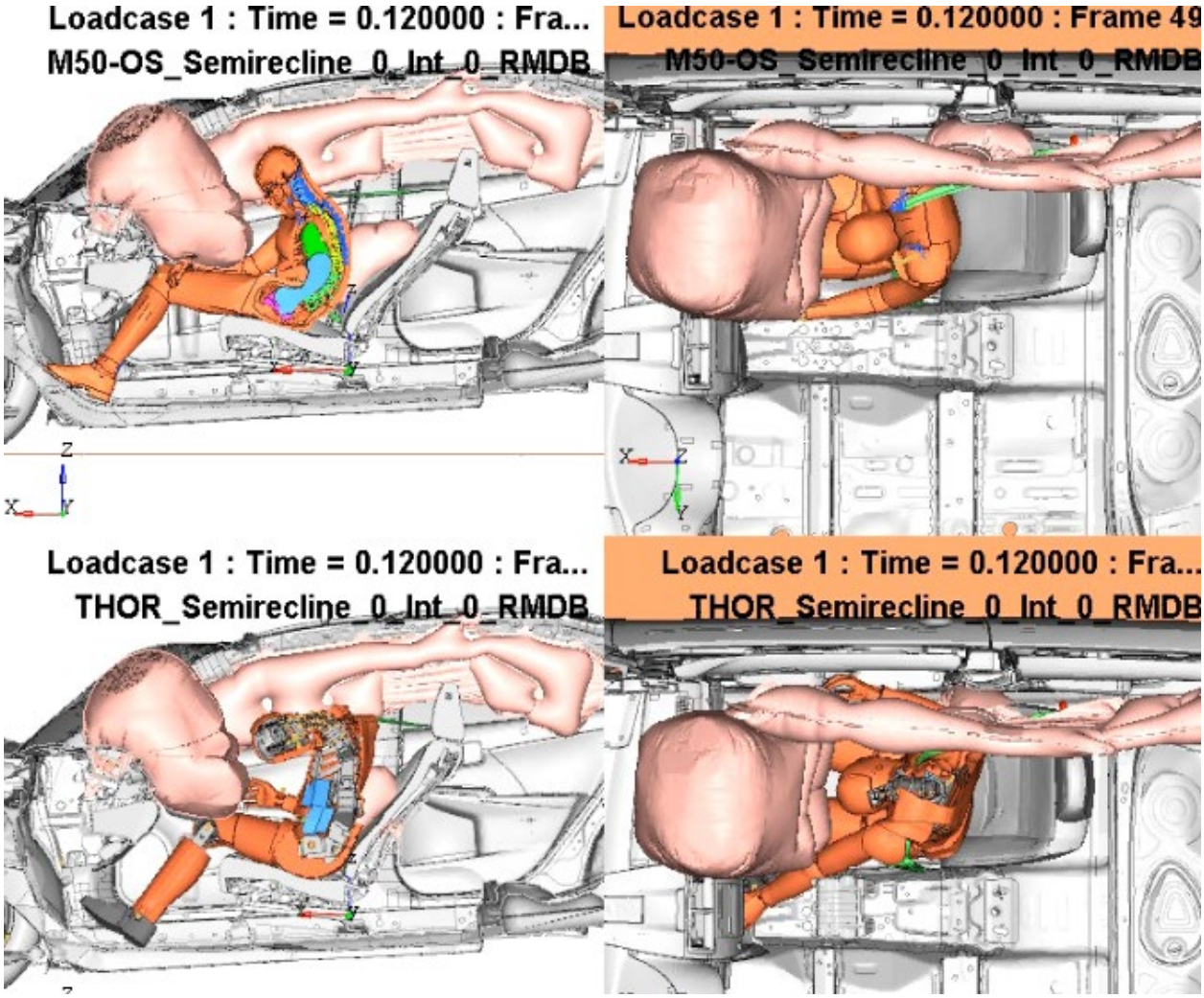

Figure 103. Semirecline_0_Int_0_RMDB for M50-OS/THOR.

Figure 104 shows a comparison of lap belt to occupant forces recorded from the simulations. The THOR lap belt contact force was higher when compared with the M50-OS; however, the shoulder belt forces remained comparable between the two models (**Figure 105**). Comparing the shoulder belt forces recorded for the upright (**Figure 92**) and semi-reclined (**Figure 105**) occupant, a similar timing of belt engagement was observed. For the integrated belt there was no engagement delay as noted for the standard belt. This is due to the fact that occupants in a semi-reclined position were located farther away from the standard shoulder belt and engage it later than with the integrated belt.

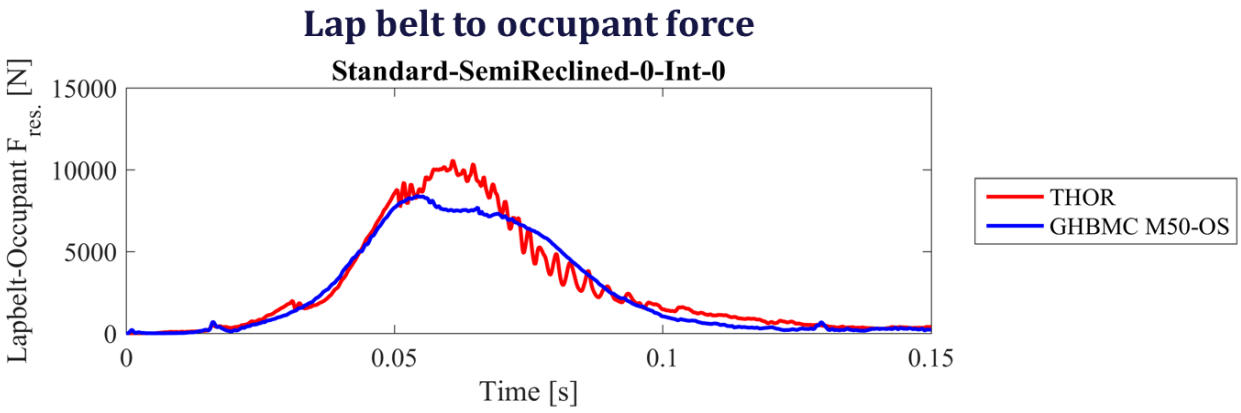

Figure 104. Lap belt to occupant force.

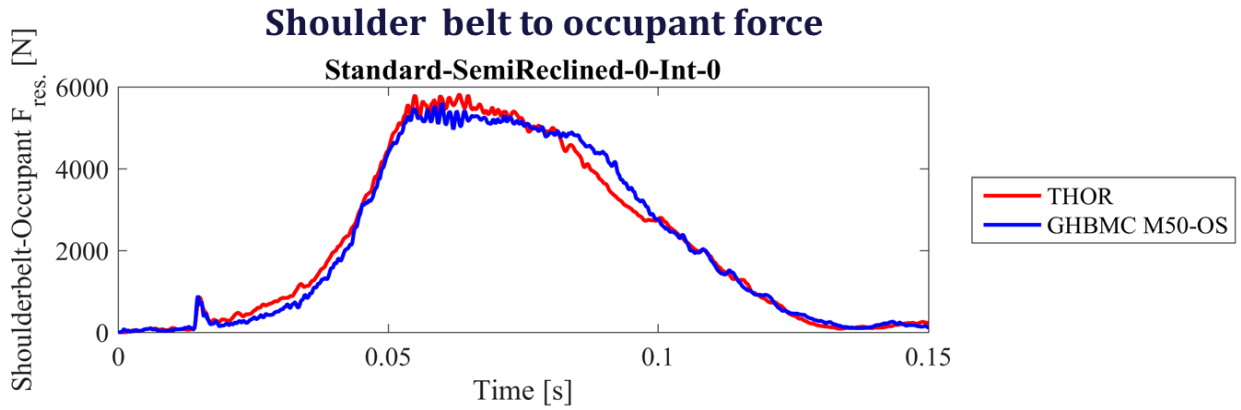

Figure 105. Shoulder belt to occupant force.

For head angular velocity, a large discrepancy may be observed between the THOR FE and M50-OS response. The peak THOR response around the local Y axis (50 rad/sec) was almost twice that of the peak recorded for the M50-OS (30 rad/sec). This difference can again be explained by the difference in thoracic and lumbar spine articulation between THOR and M50-OS occupants. THOR's lumbar and thoracic spine remained extended throughout the event (**Figure 103**), which resulted in a delayed and larger (**Figure 106**) neck flexion during the belt engagement. This resulted in a higher angular velocity recorded by THOR head in the sagittal plane. However, in the case of M50-OS the spine underwent substantial flexion throughout the event and resulted in a milder neck flexion and lower angular velocity observed by the occupant. Interestingly, comparing all frontal cases investigated in occupant semi-reclined position, the M50-OS with an integrated belt showed a lower head angular velocity than any other case.

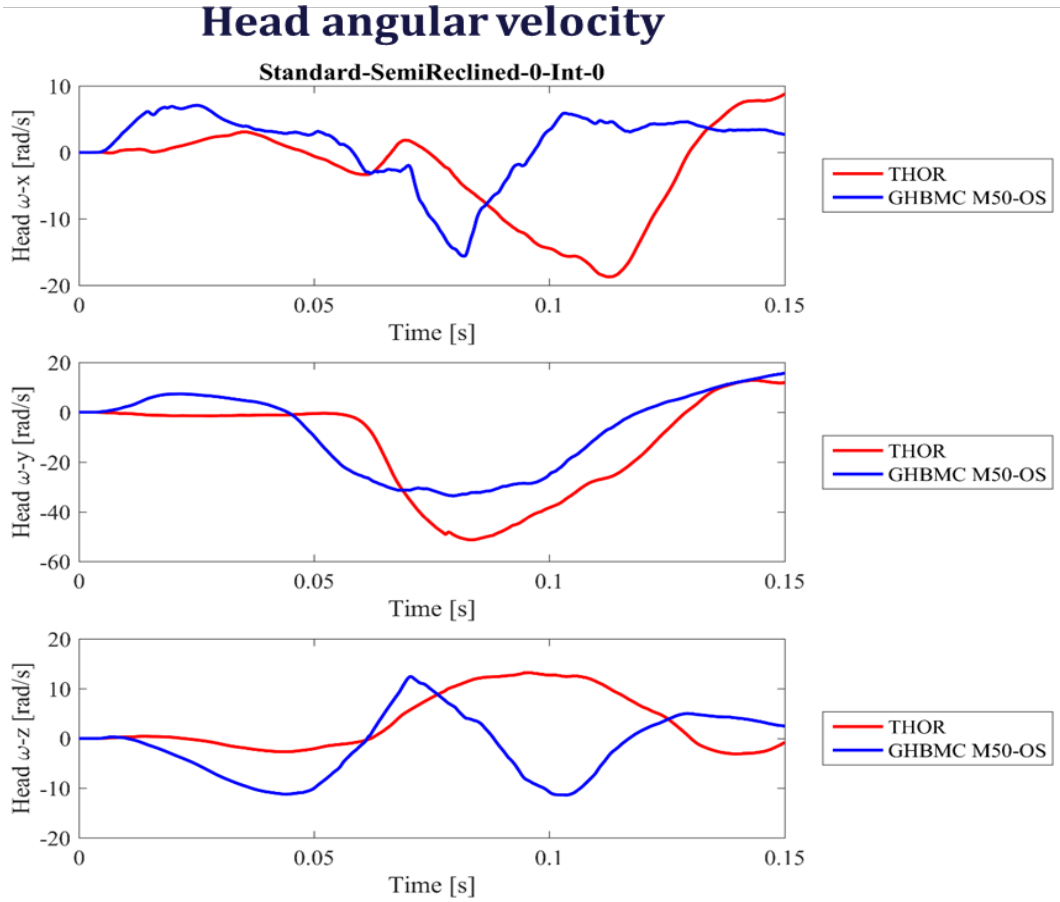

Figure 106. Head angular velocity.

The analysis of the pelvis rotation yields similar conclusions as for the upright cases. **Figure 107** shows the comparison of the pelvis rotation in the sagittal plane between the two models.

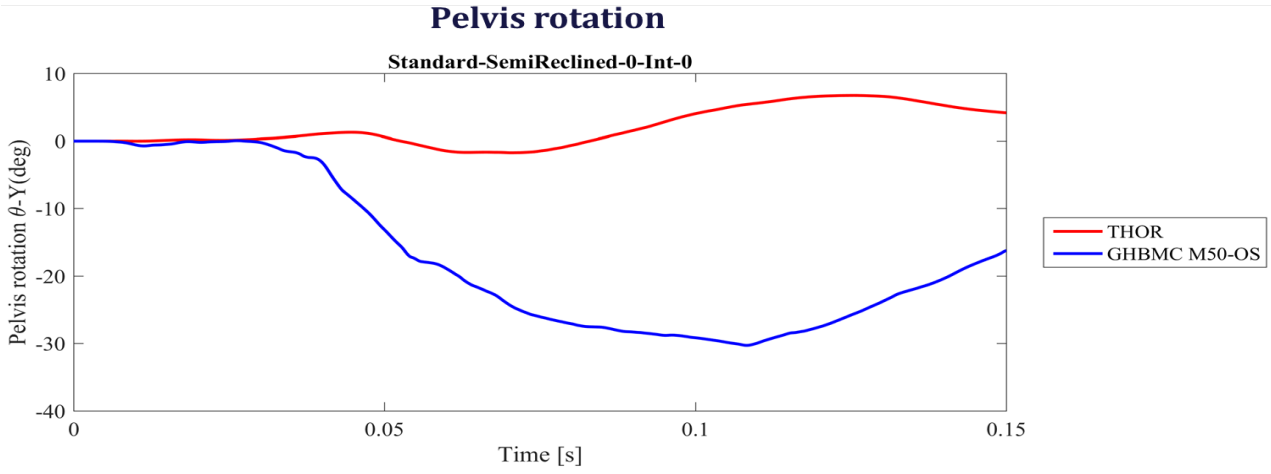

Figure 107. Pelvis rotational about Y axis.

7.2.5 Upright seated, front-facing, standard seat belt (M50-OS versus M50-O)

At first, a comparison between upright M50-OS and M50-O in nominal position, which is 0˚ seat rotation, standard seat belt under frontal impact, was made (**Figure 108**).

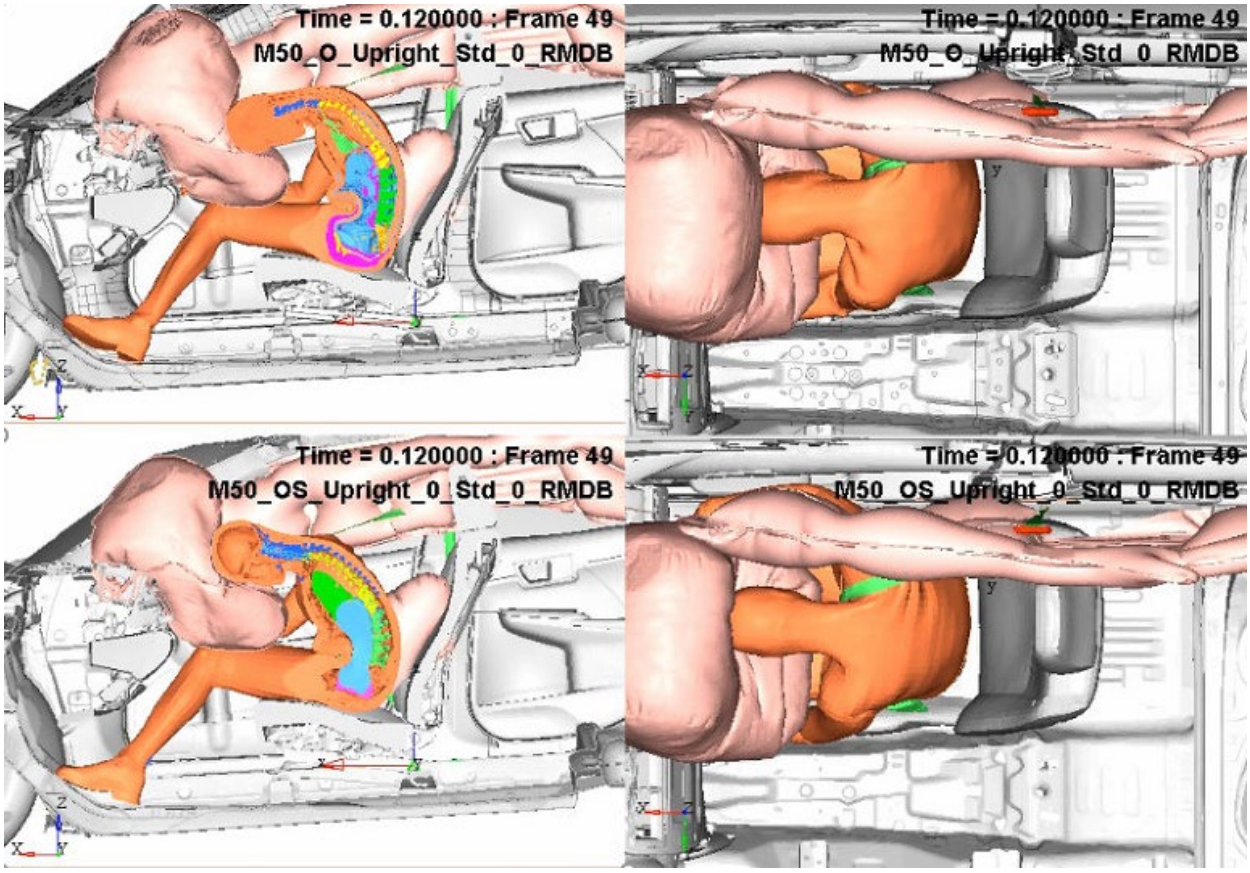

Figure 108. Upright_0_Std_0_RMDB for M50-OS/M50-O.

Considering the lap and shoulder belt forces for these two simulations, both belts provide good belt fit for the upright occupants, and their results were expected to be similar between the two models (**Figure 109** and **Figure 110**). For the interaction force between the passenger air bag (PAB) and occupant, the force to M50-OS is slightly higher than that to M50-O (**Figure 111**).

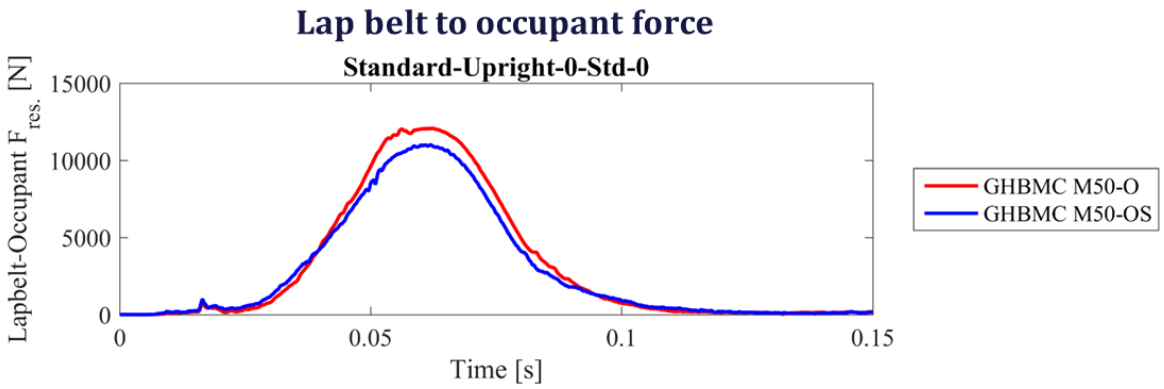

Figure 109. Lap belt to occupant force.

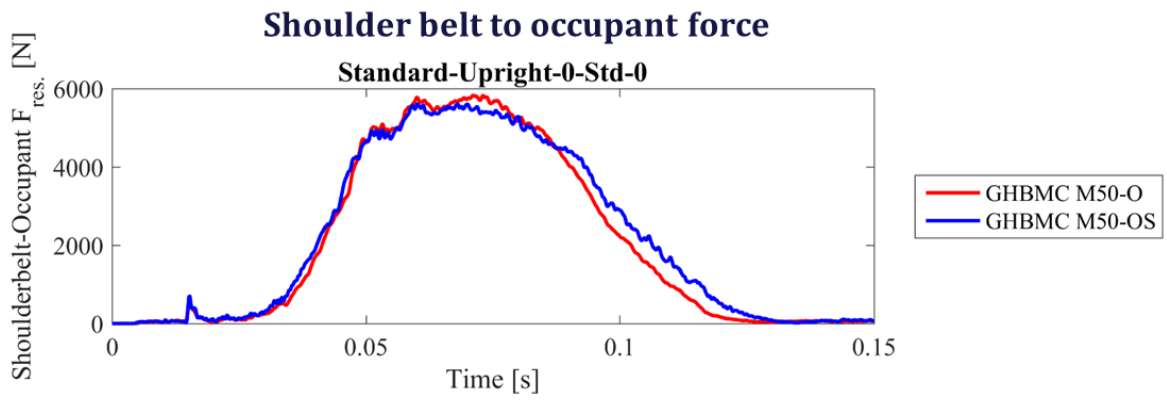

Figure 110. Shoulder belt to occupant force.

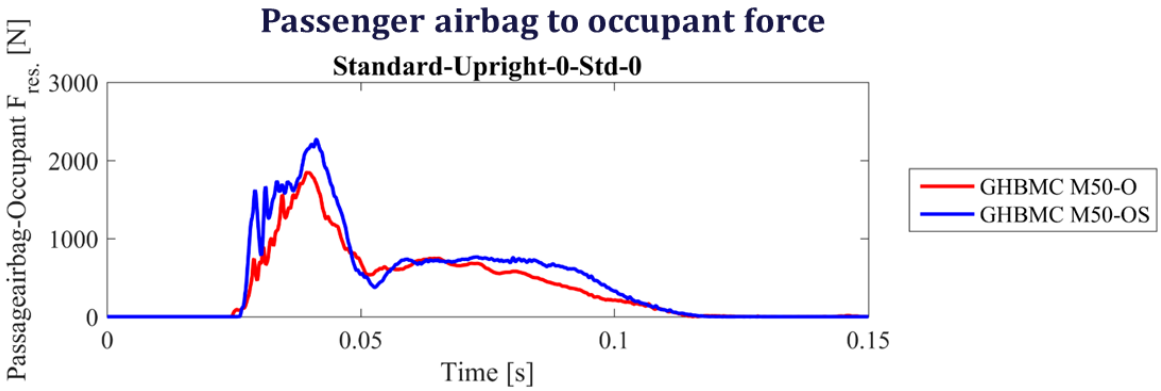

Figure 111. Passenger air bag to occupant force.

Figure 112 displays the occupant to seat cushion force and shows that the seat cushion force recorded for M50-O was higher than that recorded for M50-OS. From a detailed analysis of the simulation video, the knees of M50-O moved further into the knee bolster, which helped explain why the seat cushion force to M50-O is higher than that to M50-OS.

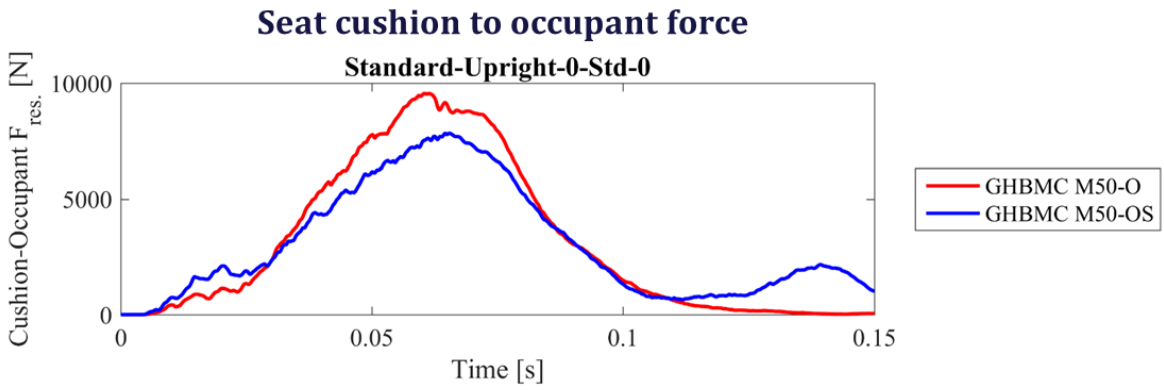

Figure 112. Seat cushion to occupant force.

In case of recorded head angular velocity, both signals remain comparable until 80ms of the recorded event. A detailed review of the simulation video revealed that M50-O's lumbar spine remained extended throughout the event that resulted in a larger neck flexion about Y axis. The X and Z measurements show some discrepancies between the models. However, they are substantially smaller in magnitude (**Figure 113**).

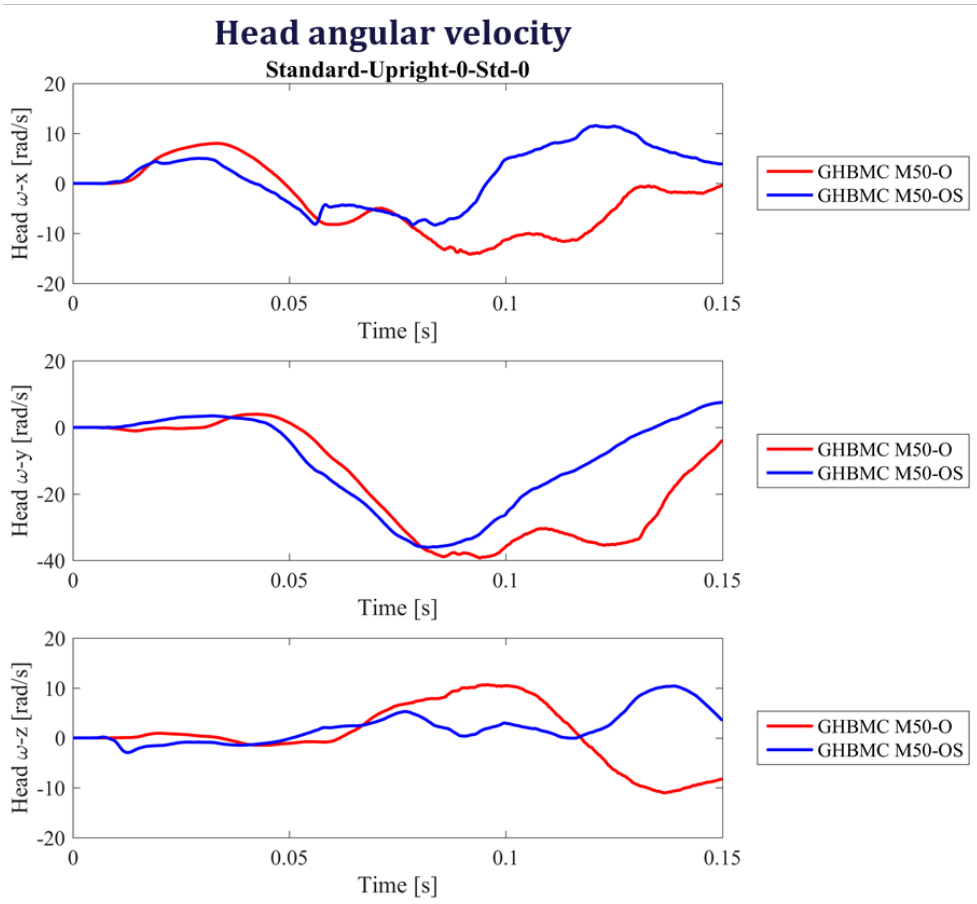

Figure 113. Head angular velocity.

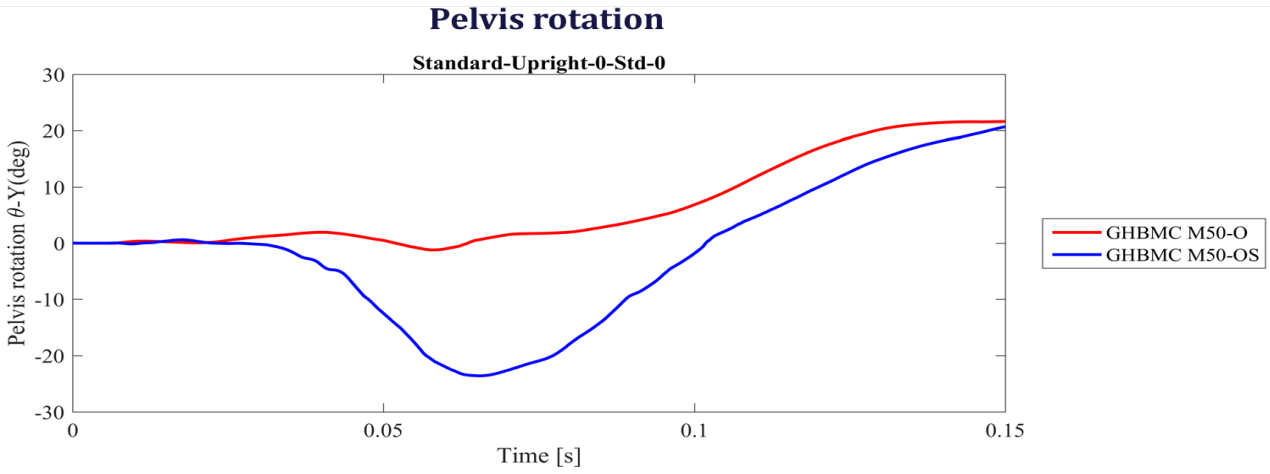

Figure 114 Pelvis rotational about Y axis.

7.2.6 Semi-reclined seated, front-facing, integrated seat belt (M50-O versus M50-OS)

This is a comparison between semi-reclined M50-OS and M50-O models, which is 0˚ seat rotation, and integrated seat belt under frontal impact was made (**Figure 115**).

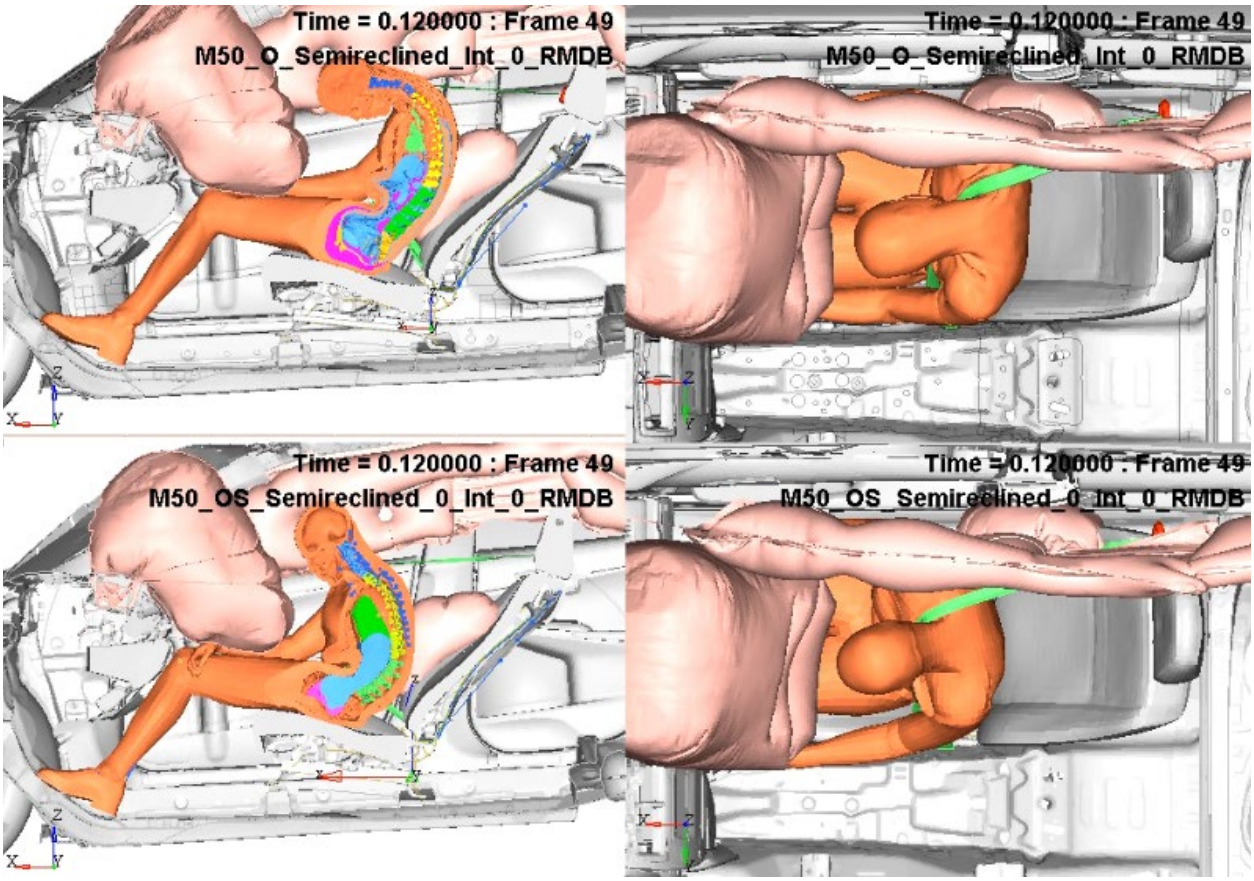

Figure 115. Semi-reclined_0_Int_0_RMDB for M50-OS/M50-O.

In terms of lap belt forces (**Figure 118**), the force to M50-O displayed higher peak value than that to M50-OS. However, the peak value of shoulder belts to both models is similar (**Figure 119**). For the interaction force between PAB and occupant, the force to M50-OS is pretty close to M50-O because occupants in a semi-reclined posture are located farther from the PAB (**Figure 118**). The forces are comparable between M50-OS and M50-O, but the M50-O vehicle force is slightly higher.

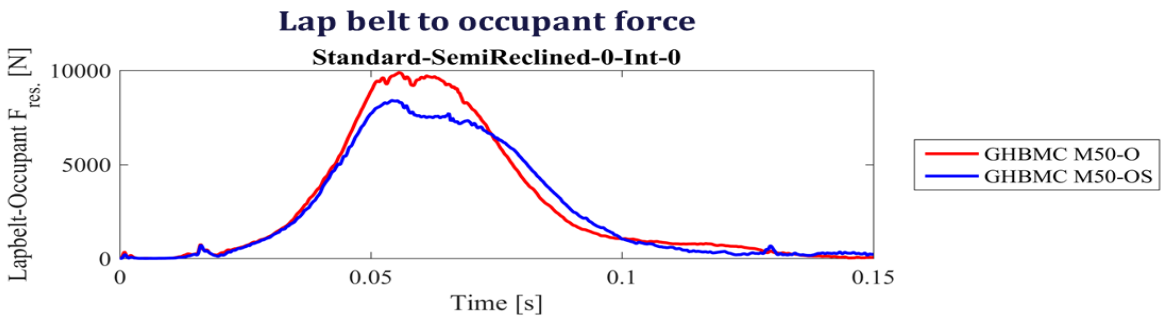

Figure 116. Lap belt to occupant force.

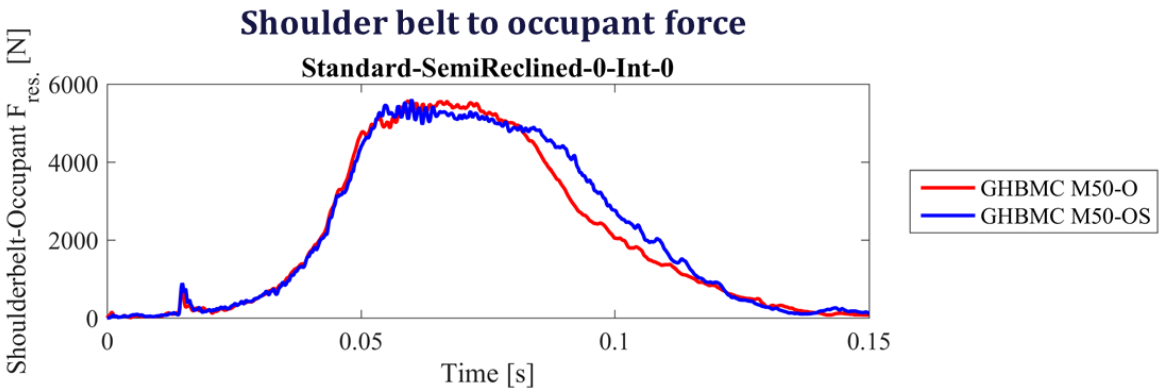

Figure 117. Shoulder belt to occupant force.

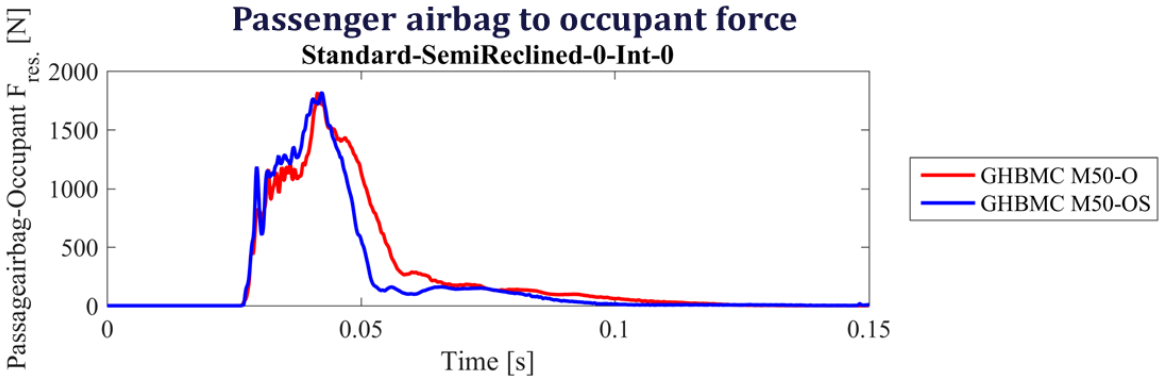

Figure 118. Passenger air bag to occupant force.

Figure 119 displays the occupant to seat cushion force and shows that the seat cushion force recorded for M50-O was higher than that recorded for M50-OS. From a detailed analysis of the simulation video, the knees of M50-O moved further into the knee bolster that helped explain why the seat cushion force to M50-O is higher than that to M50-OS.

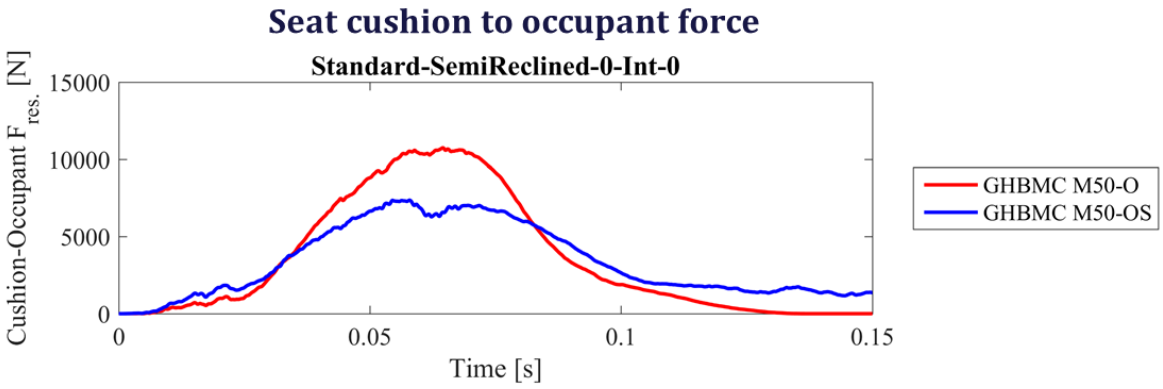

Figure 119. Seat cushion to occupant force.

In case of recorded head angular velocity, both signals remain comparable until 70ms of the recorded event. A detailed review of the simulation video revealed that M50-O's lumbar spine remained extended throughout the event that resulted in a larger neck flexion about Y axis. The X and Z measurements of M50-O are higher than those of M50-OS due to more severe shoulder loads with M50-O (**Figure 120**).

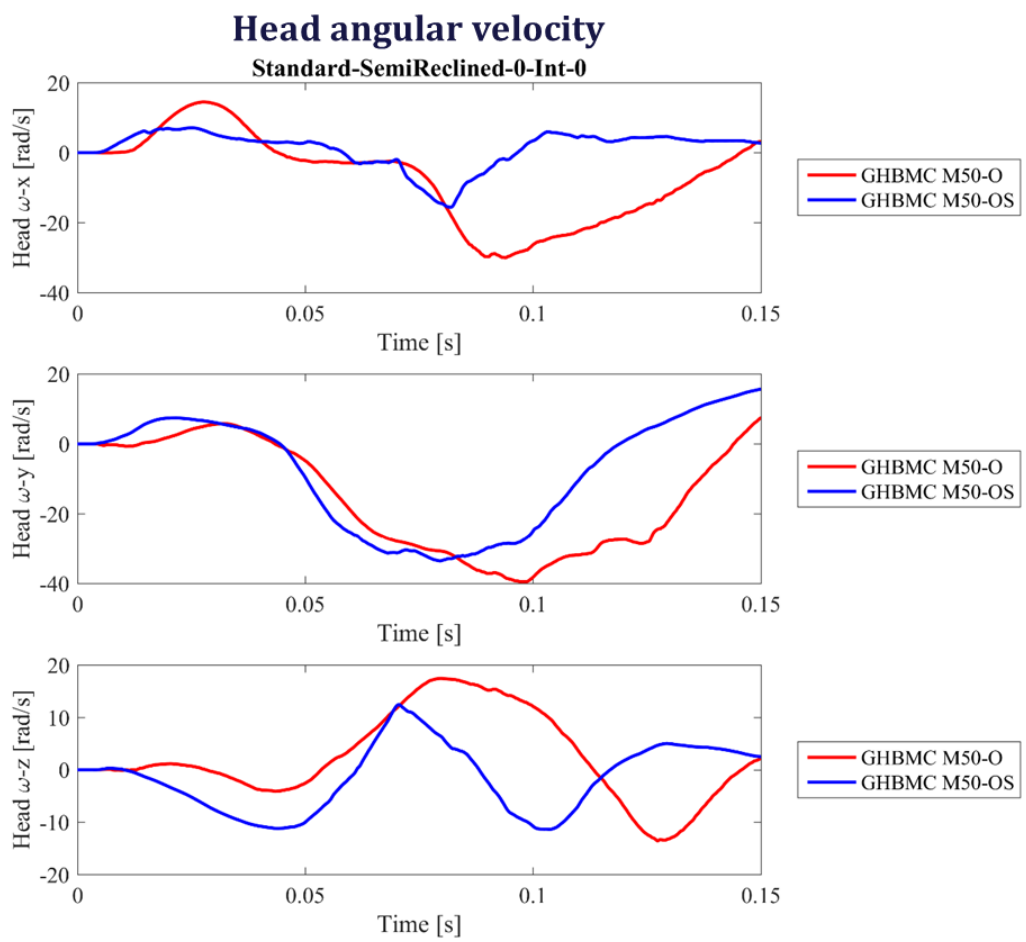

Figure 120. Head angular velocity.

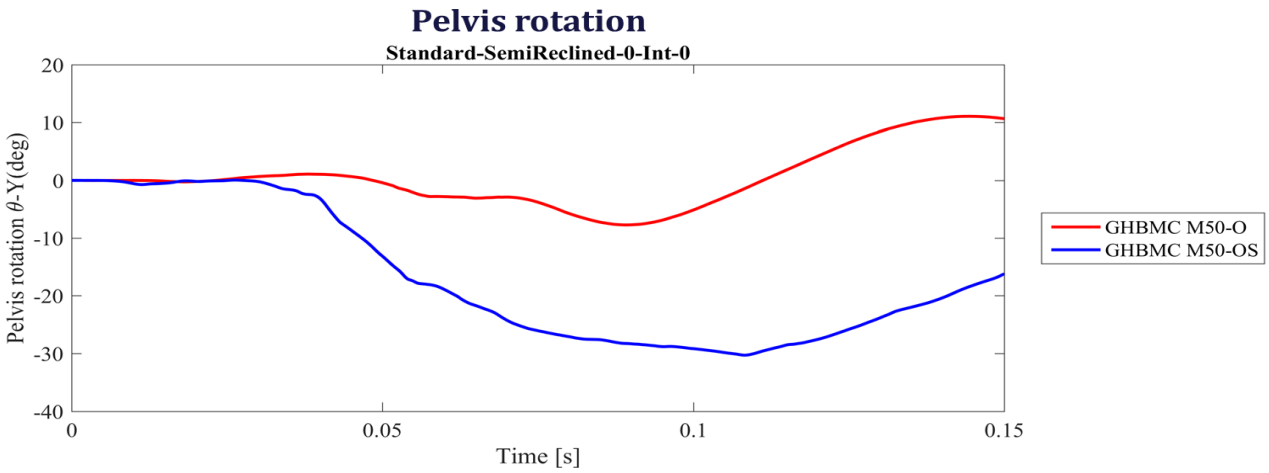

Figure 121. Pelvis rotational about Y axis.

7.2.7 Reclined seated, front-facing, integrated seat belt (M50-O vs M50-OS)

At first, a comparison between reclined M50-OS and M50-O in 60° recline position with integrated seat belt under frontal impact was made (**Figure122**).

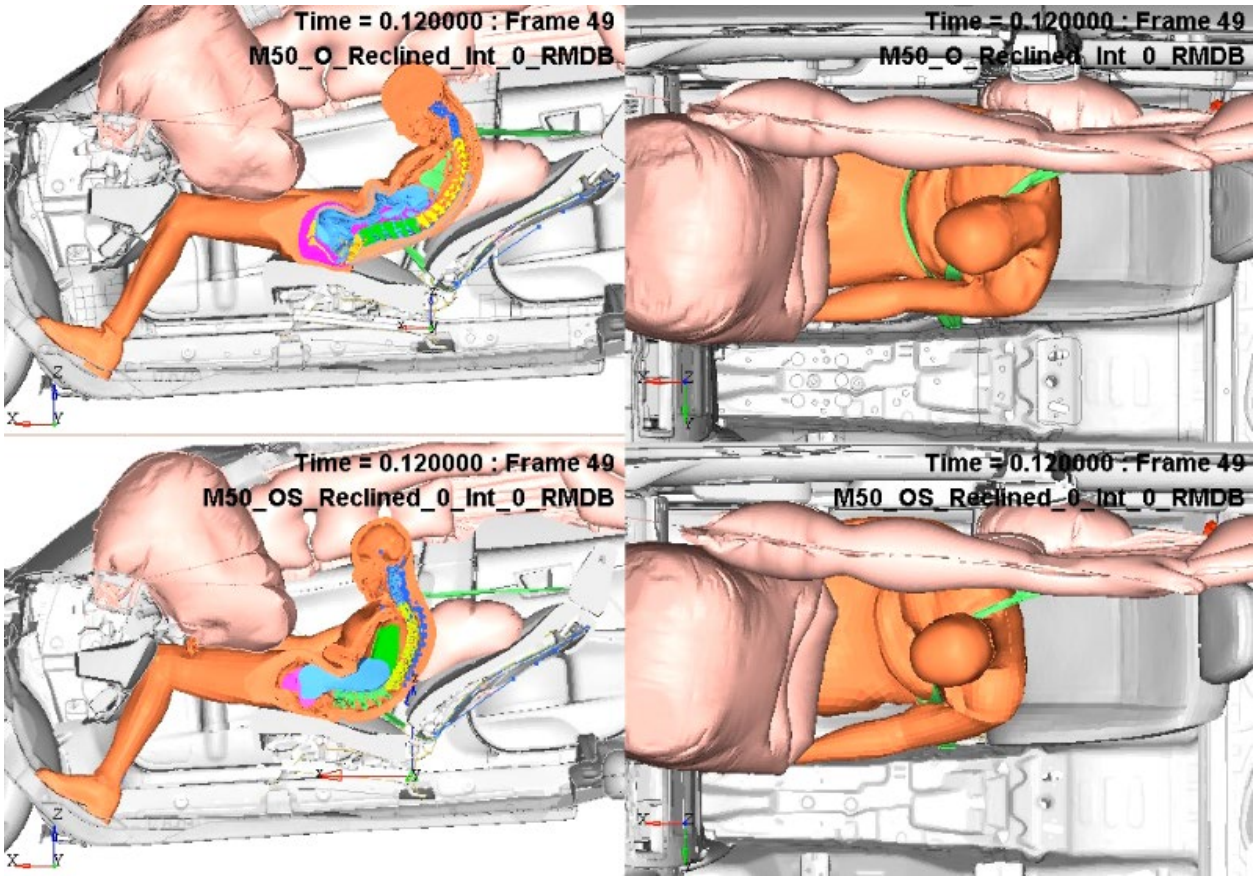

Figure 122. Reclined_0_Int_0_RMDB for M50-OS/M50-O.

Considering the lap and shoulder belt forces for these two simulations, both types of seat belts provide good belt fit for the reclined occupants, and their results were expected to be similar (**Figure 123** and **Figure 124**). For the interaction force between PAB and occupant, the force to M50-OS is pretty close to M50-O because occupants in reclined postures are located further from the PAB (**Figure 125**).

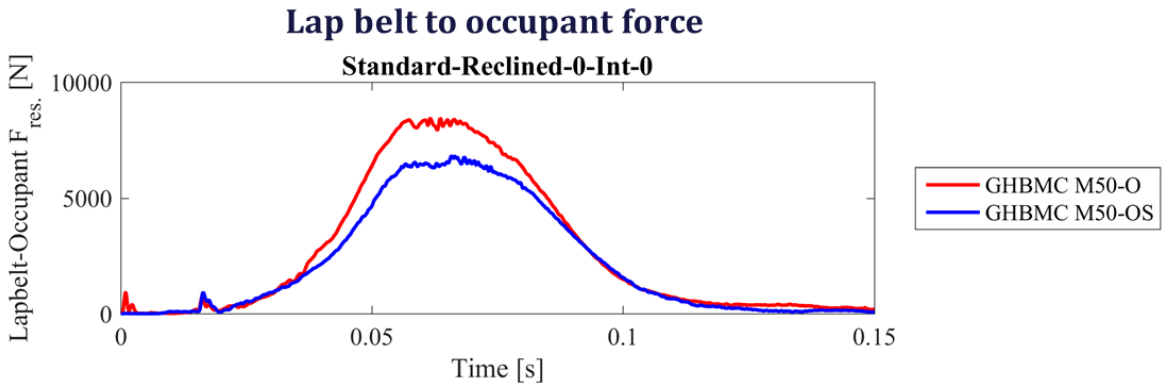

Figure 123. Lap belt to occupant force.

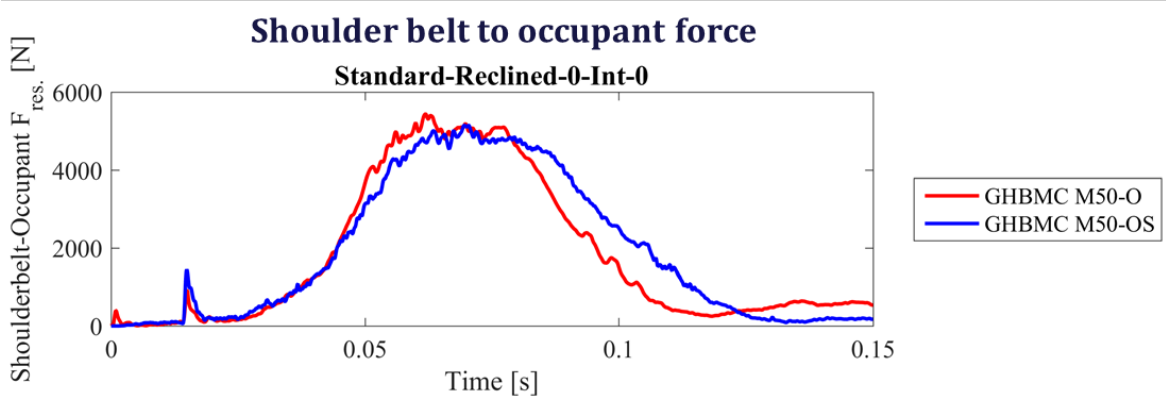

Figure 124. Shoulder belt to occupant force.

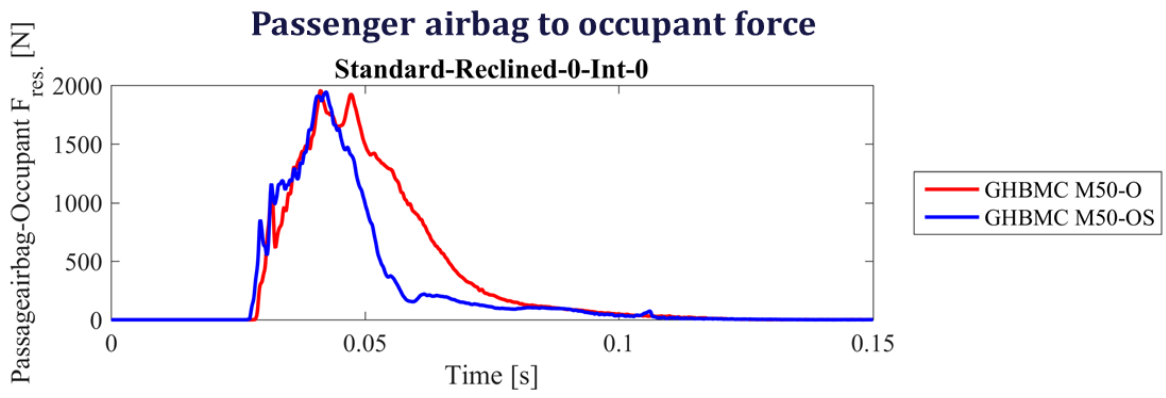

Figure 125. Passenger air bag to occupant force.

Figure 126 displays the occupant to seat cushion force and shows that the seat cushion force recorded for M50-O was higher than that recorded for M50-OS. From a detailed analysis of the simulation video, the knees of M50-O moved further into the knee bolster that helped explain why the seat cushion force to M50-O is higher than that to M50-OS.

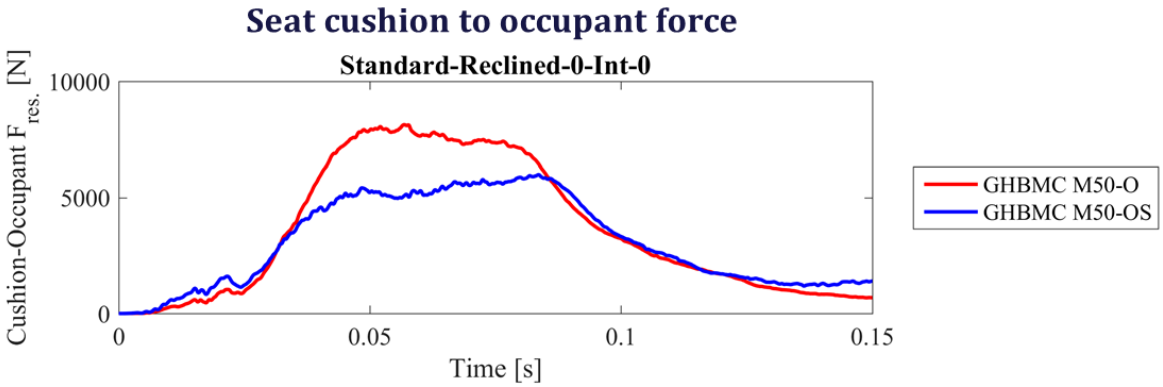

Figure 126. Cushion to occupant force.

For the recorded head angular velocity, both signals about Y and Z axis remain comparable until 70ms of the recorded event. A detailed review of the simulation video revealed that M50-O's lumbar spine remained extended throughout the event that resulted in a larger neck flexion about Y axis. The X and Z measurements of M50-O are much higher than those of M50-OS due to more severe shoulder interaction with M50-O (**Figure 127)**.

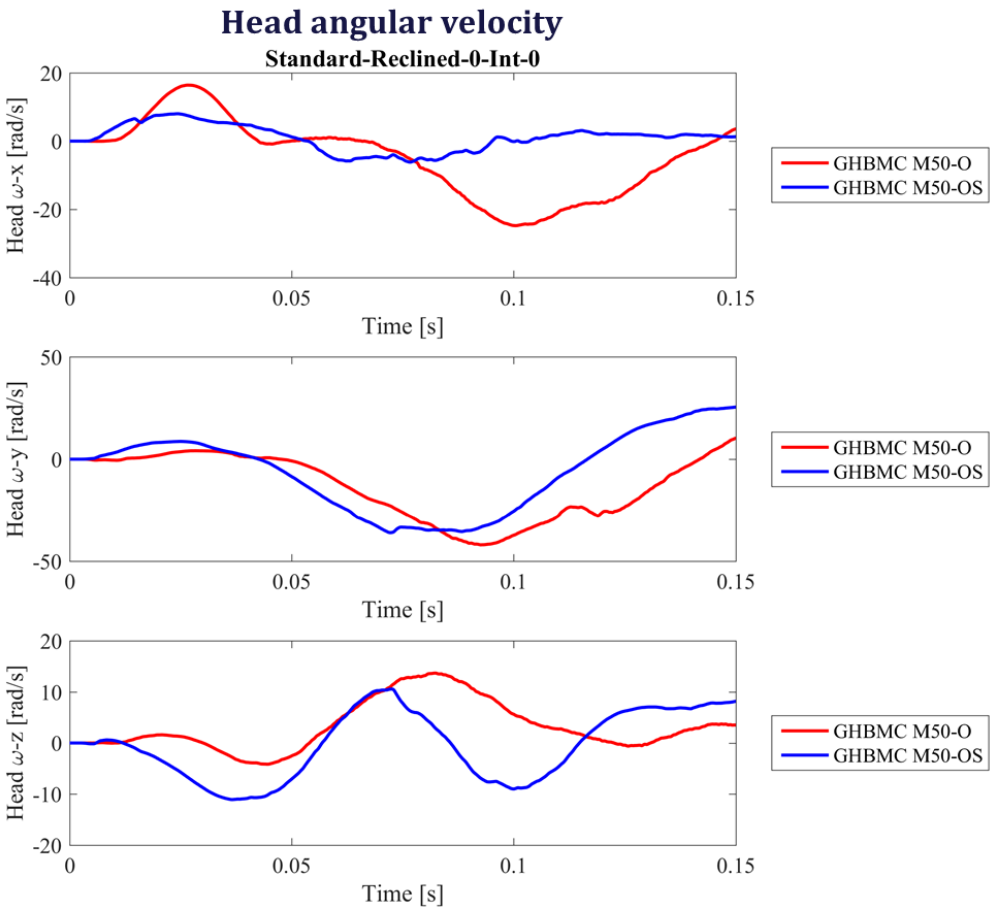

Figure 127. Head angular velocity.

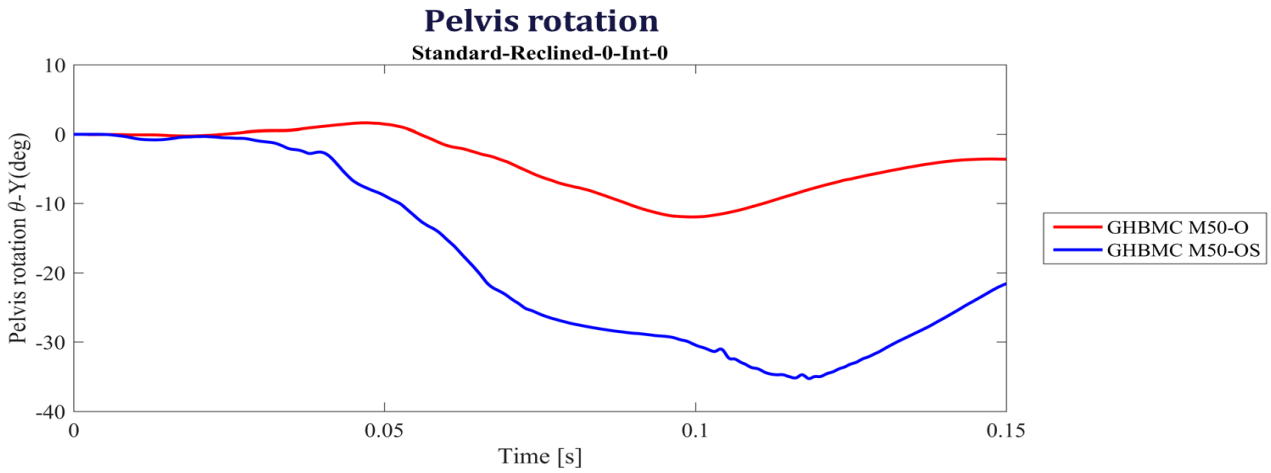

Figure 128. Pelvis rotational about Y axis.

7.3 Select Rear Impact Cases

7.3.1 Upright seated, rear-facing, standard seat belt (THOR versus M50-OS)

Figure 129 shows a comparison between M50-OS and THOR with standard seat belt under rear impact condition. In both cases, the seat support frames were damaged due to occupant inertial load during the impact. As a result, the seatbacks folded back and the occupants slid up the seat.

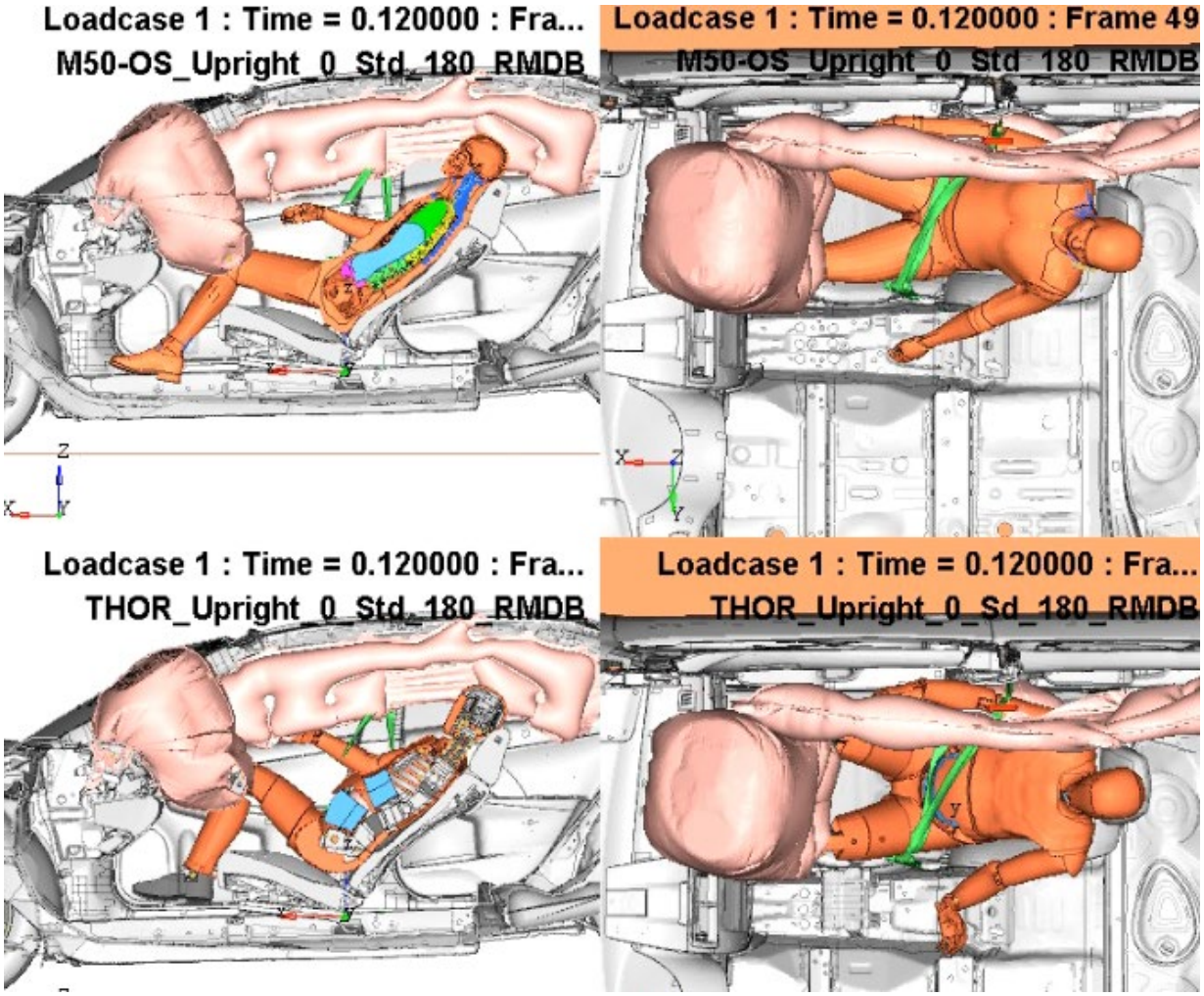

Figure 129. Upright_0_Std_180_RMDB for M50-OS/THOR.

Figure 130 and **Figure 131** show the belt forces recorded in both simulations. The lap belt shows around 800N load late in the simulation for both occupants. This load is due to the occupant motion up the seatback, and its thighs engaging with the lap belt late in the simulation. Since this was a simulation of a rear impact condition, no substantial shoulder belt loads were observed.

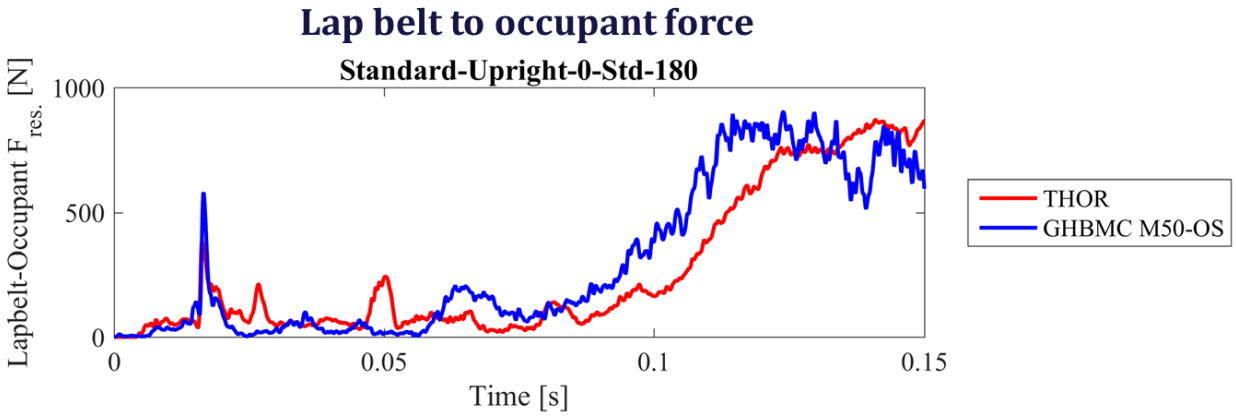

Figure 130. Lap belt to occupant force.

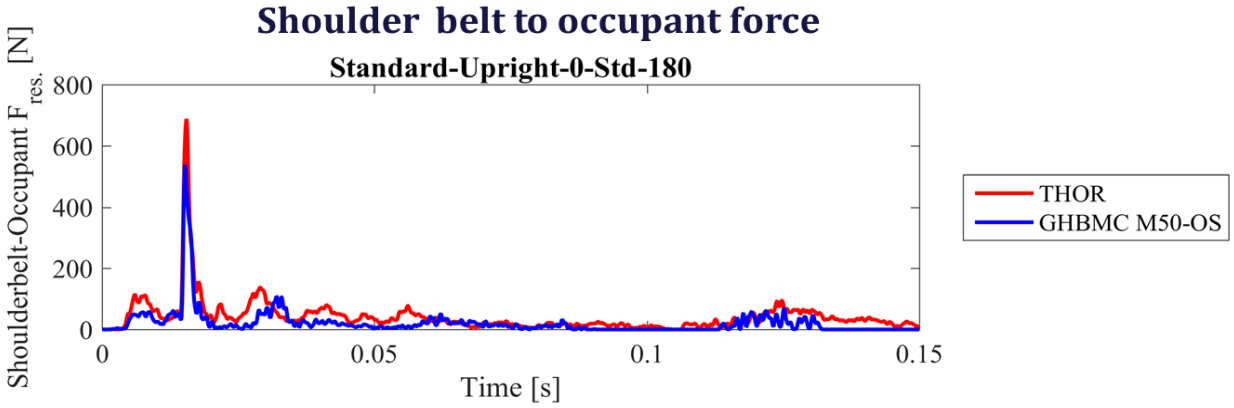

Figure 131. Shoulder belt to occupant force.

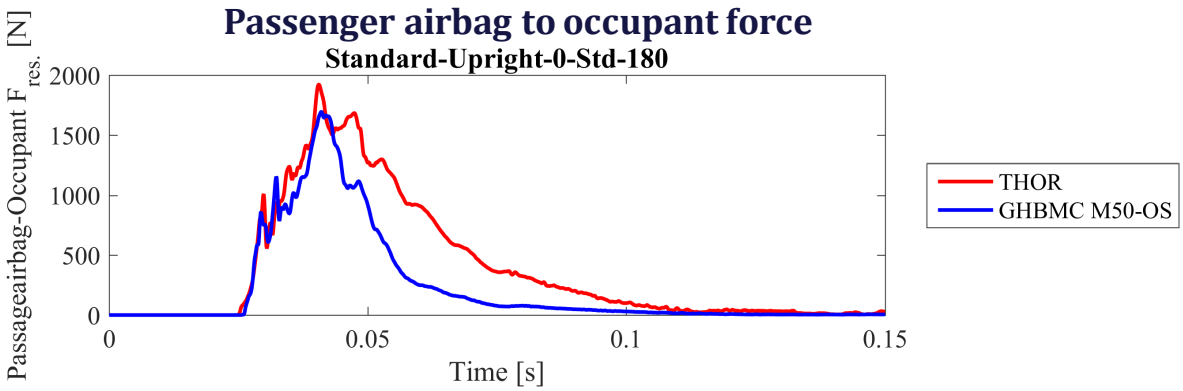

Figure 132. Passenger air bag to occupant force.

Figure 133 displays seat back force to occupant. THOR FE reached to an earlier and higher peak force around 0.04s than M50-OS due to the stiffer lumbar spine. Additionally, the internal organs and spine of M50-OS slid along the seatback instead of directly compressing the seatback at the beginning that is helpful to explain the relatively late peak force. For THOR, the interaction between upper thoracic block and seat back explained the increase of the force after first decrease.

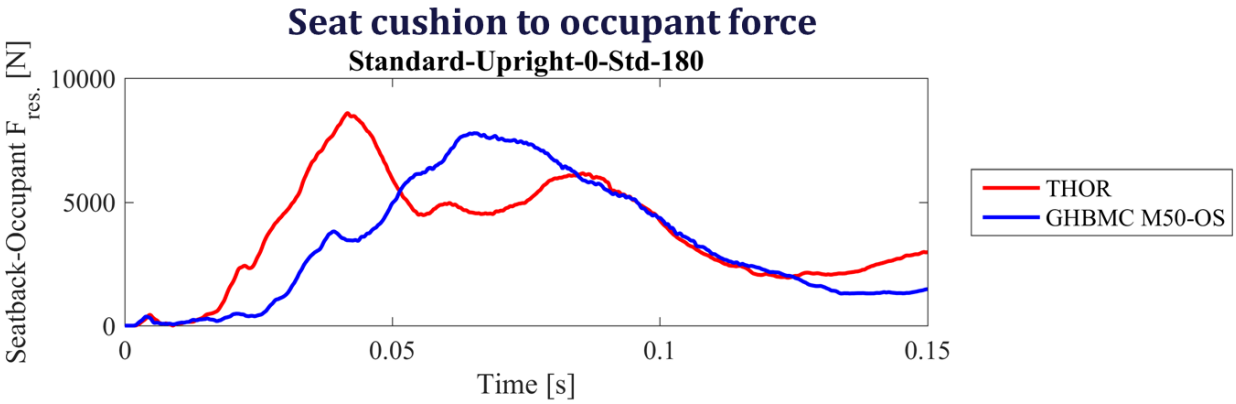

Figure 133. Seat back to occupant force.

Figure 135 shows the occupant pelvis motion in the sagittal plane. The pelvis of the THOR FE rotated monotonically backwards throughout the entire simulation. On the other hand, the pelvis of the M50-OS first rotated forward, then after the knee to seat cushion impact changed direction and rotated backward. The discrepancy in the response between the two models is again explained by a larger flexibility of the lumbar spine in the M50-OS model.

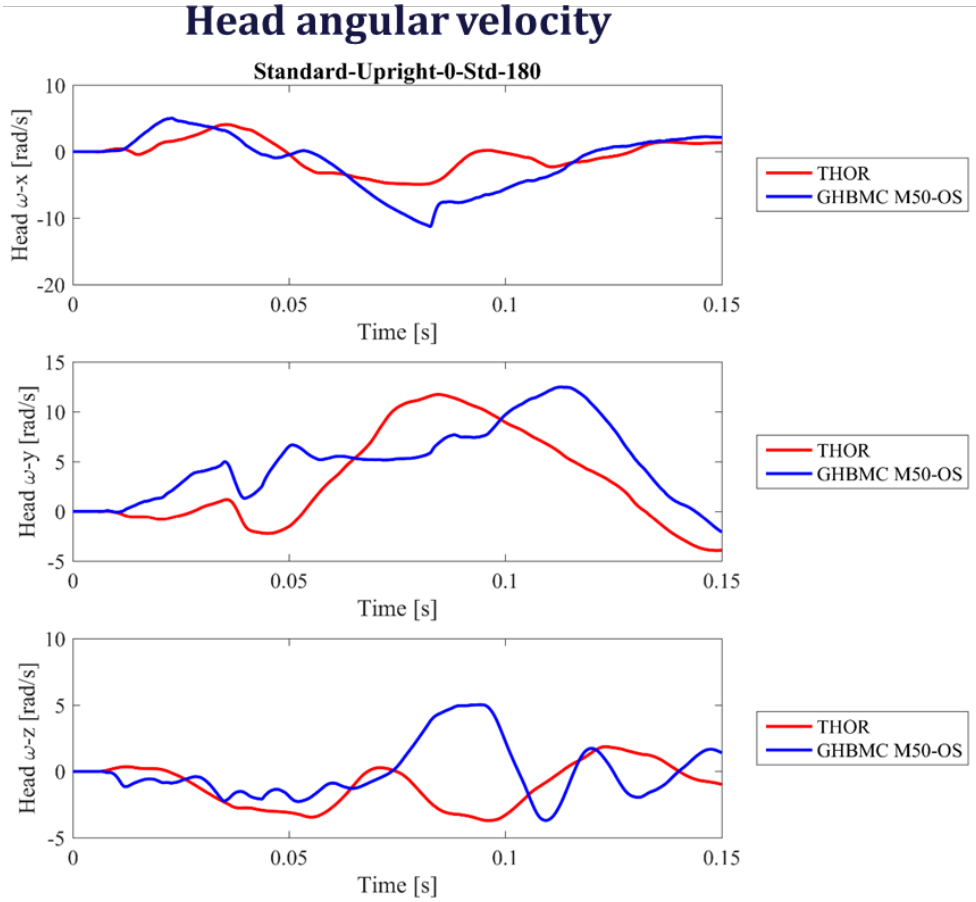

Figure 134. Head angular velocity.

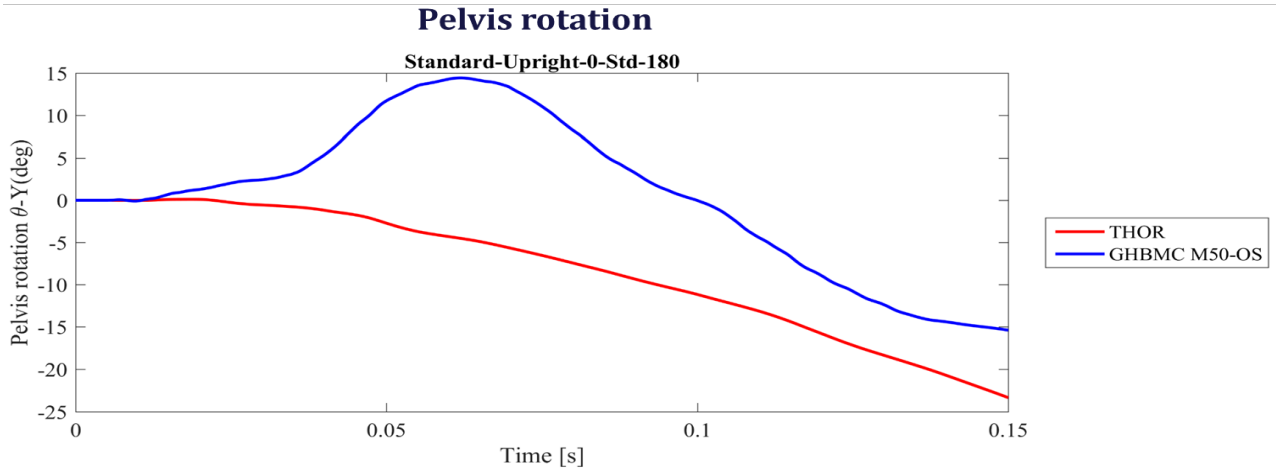

Figure 135. Pelvis rotational about Y axis.

7.3.2 Upright seated, rear-facing, integrated seat belt (THOR vs M50-OS)

Figure 136 shows a comparison between M50-OS and THOR with integrated seat belt under rear impact condition. Contrary to the standard seat, the integrated seat was implemented along with the seat reinforcement structure to satisfy FMVSS 210 requirements. The reinforced seat withheld the inertial load of the occupant during the rear impact conditions.

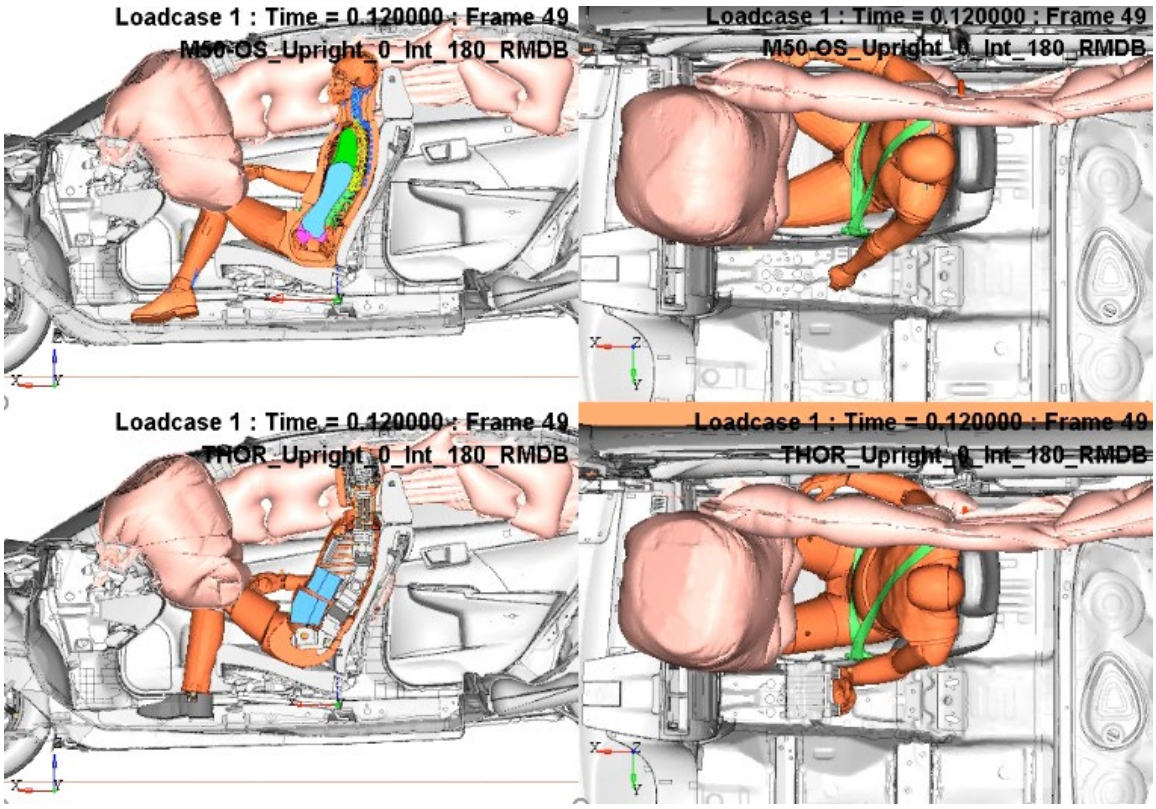

Figure 136. Upright_0_Int_180_RMDB for M50-OS/THOR.

Figure 137 and **Figure 138** show the belt forces recorded in both simulations. Lap belt forces are low for both occupants. Since the seatback supports the occupant throughout the impact no lap belt force increase is seen at the end of the simulation. This is different for the cases with standard belt discussed above. Since this was a simulation of a rear impact condition, no substantial shoulder belt loads were observed.

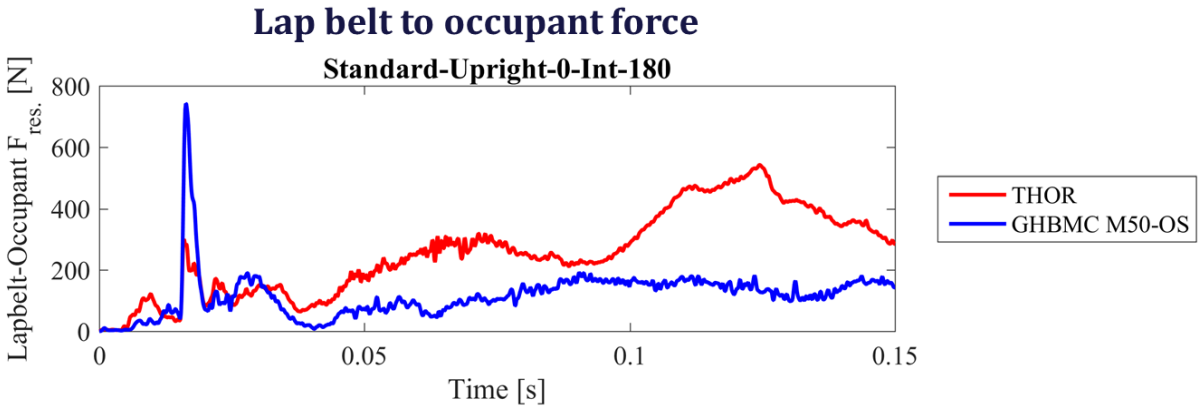

Figure 137. Lap belt to occupant force.

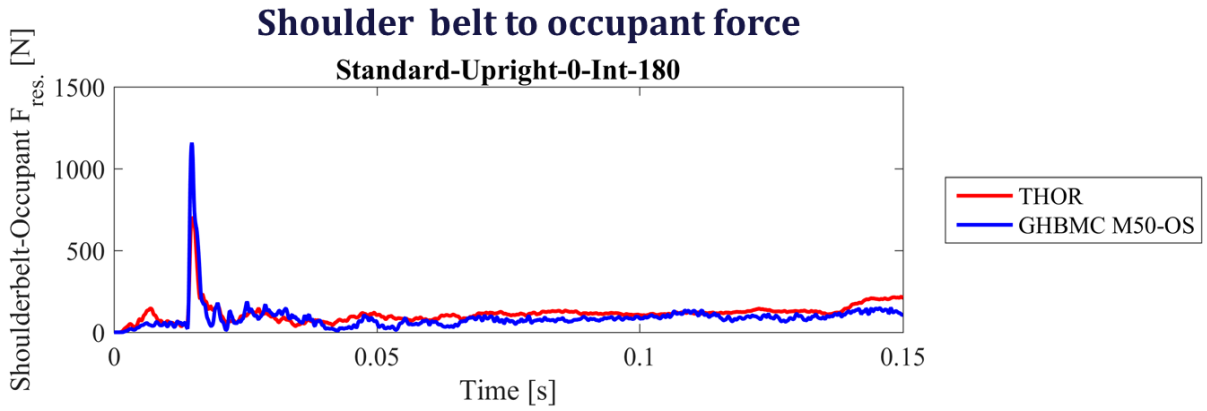

Figure 138. Shoulder belt to occupant force.

Comparing the seatback to occupant forces recorded for M50-OS and THOR, an earlier and slightly higher peak force to THOR was observed due to the stiffer lumbar and thoracic spine. Additionally, from the detailed simulation videos, THOR FE bounced back from the seat back twice that could also explain why the force to THOR increased again after the first decrease (**Figure 140**).

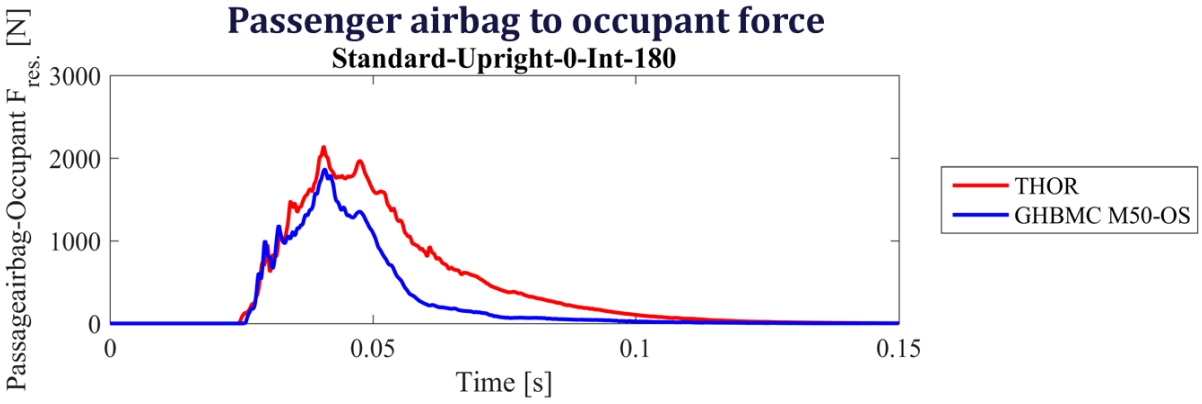

Figure 139. Passenger airbag to occupant force.

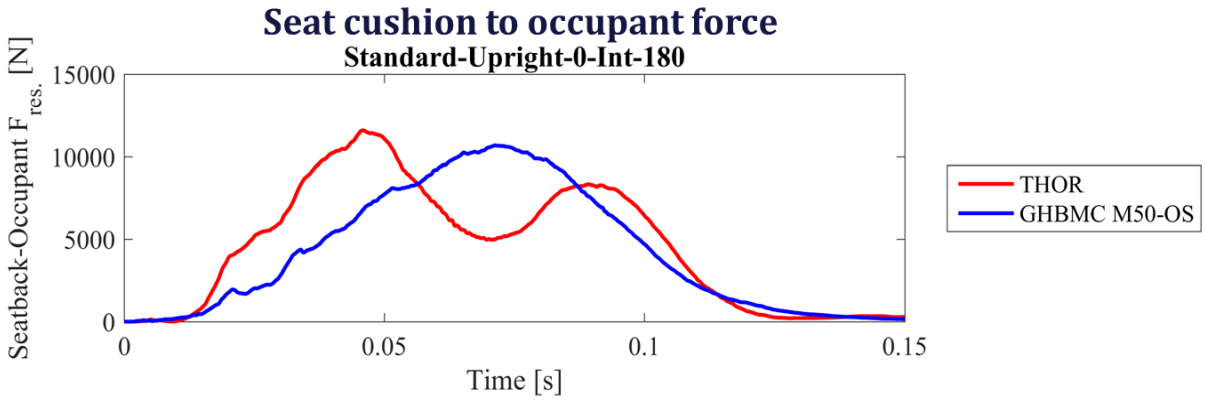

Figure 140. Seat back to occupant force.

Figure 142 shows the occupant pelvis motion in the sagittal plane. The pelvis of the THOR FE showed no substantial rotation throughout the entire simulation. On the other hand, the pelvis of the M50-OS first rotated forward, then after the knee to seat cushion impact changed direction and rotated backward. The discrepancy in the response between the two models is again explained by a larger flexibility of the lumbar spine in the M50-OS model.

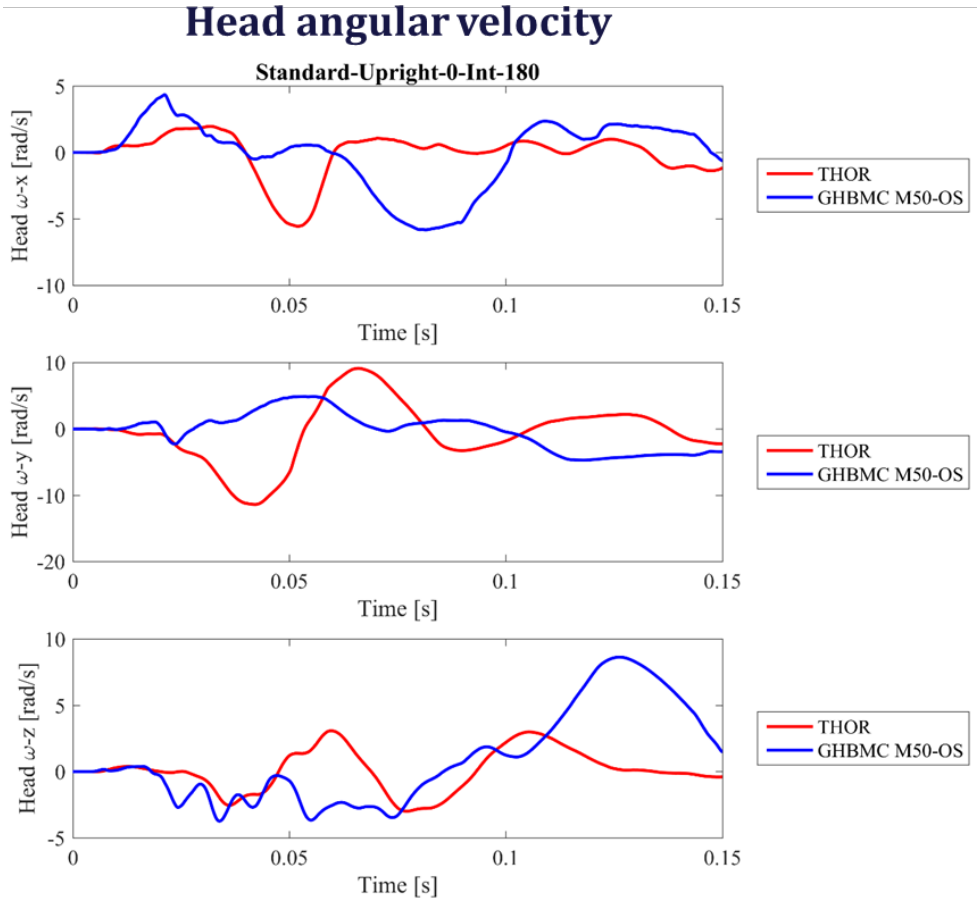

Figure 141. Head angular velocity.

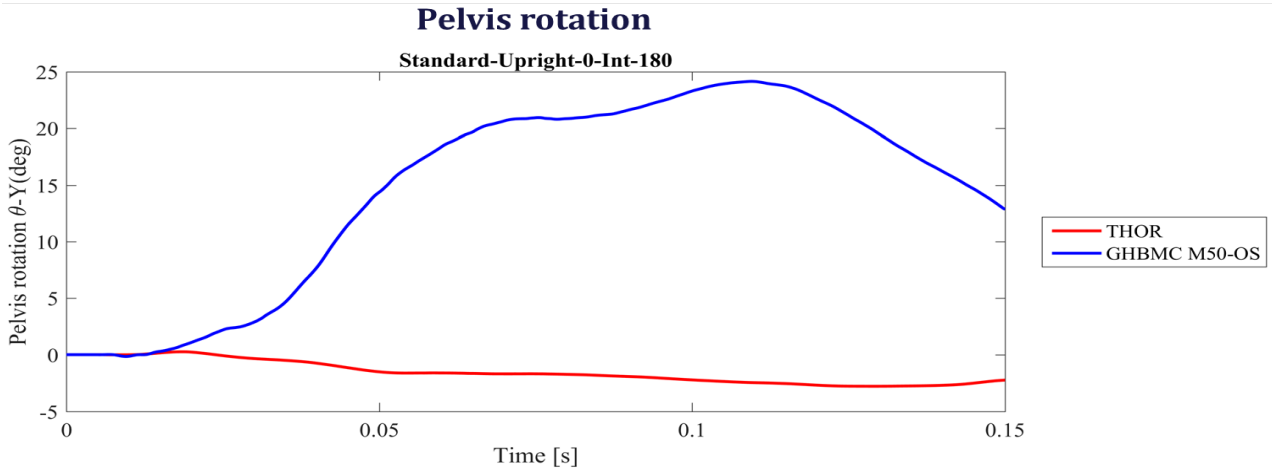

Figure 142. Pelvis rotational about Y axis.

8 Lessons Learned

In this section we discuss the primary lessons learned about the usability and potential utility of the occupant models in the postures and collision scenarios studied.

8.1 NHTSA THOR FE Model

8.1.1 THOR cannot fully recline

The degree to which the THOR FE model may be reclined is limited by the design of the pelvis. Specifically, the range of motion afforded by the pelvis flesh limits the degree to which the hip joints may be extended. This limits how much the lumbar spine and pelvis may be rotated backwards without artificially lifting the feet off of the floor. With seat pan and floor geometry studied here, the maximum degree of recline that could be achieved with the THOR FE model was approximately 40˚, prior to lifting the feet off of the floor. Note that this could potentially be addressed by modifying the dummy pelvis flesh to allow a greater degree of extension at the hip, or by allowing the feet to raise off of the floor (for example, with an elevated foot rest or leg rest).

8.1.2 THOR instability issues

Several modeling artifacts were observed with the THOR model. For example, in some cases, the THOR face flesh deforms substantially during the simulation (**Figure 143**) during contact with the restraints. These types of artifacts may be addressed in future refinements of the THOR model.

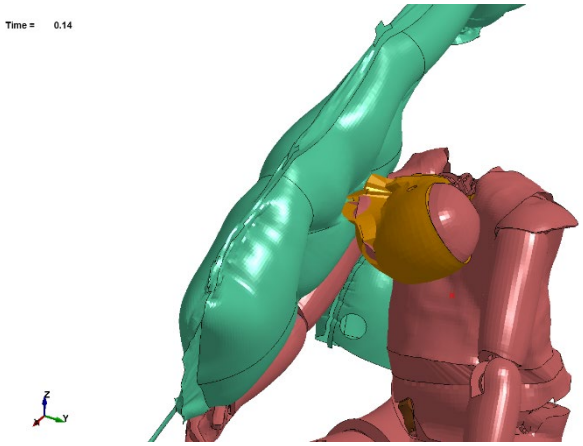

Figure 143. Deformation of THOR face flesh.

8.2 GHBMC M50-OS Model

8.2.1 GHBMC M50-OS cannot settle

The spine or thoracic region of the GHBMC M50-OS is too stiff to allow natural gravity settling into reclined positions. When gravity is applied, the pelvis of the model settles into the seat cushion, but the rest of the model remains in an upright posture. As a result, to achieve a reclined position, multiple pre-simulation steps are needed to force the model back into the seat. First,

normal gravity settling was applied. Then, a force was applied to the upper thoracic spine to force the back and shoulders into the seatback. Then, a force was applied to the head to force it into the headrest. Future work should include exploring other options for position in pre-processing, potentially using tools such as PIPER.

8.2.2 GHBMC M50-OS stability issues

Regarding model stability, the primary issues observed concerned negative volume artifacts in the abdomen during penetration by the lap belt. This was rectified by adding null shell elements around the hexahedral elements and applying a CONTACT_AUTOMATIC_SINGLE_ SURFACE contact definition to those shell elements (**Figure 144** and **Figure 145**). This prevented internal penetration and associated negative volume errors, and is a robust alterative to CONTACT_INTERIOR.

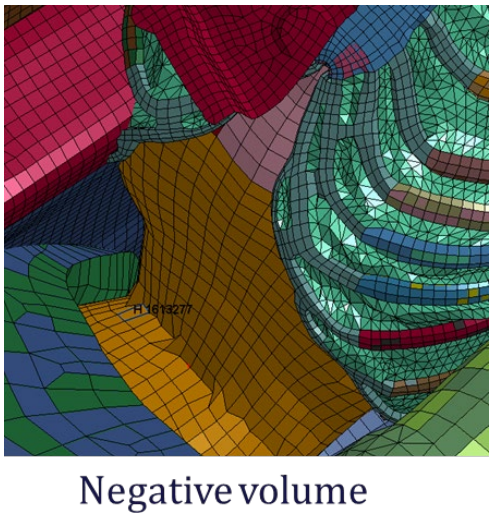

Figure 144. GHBMC M50-OS abdomen negative volume.

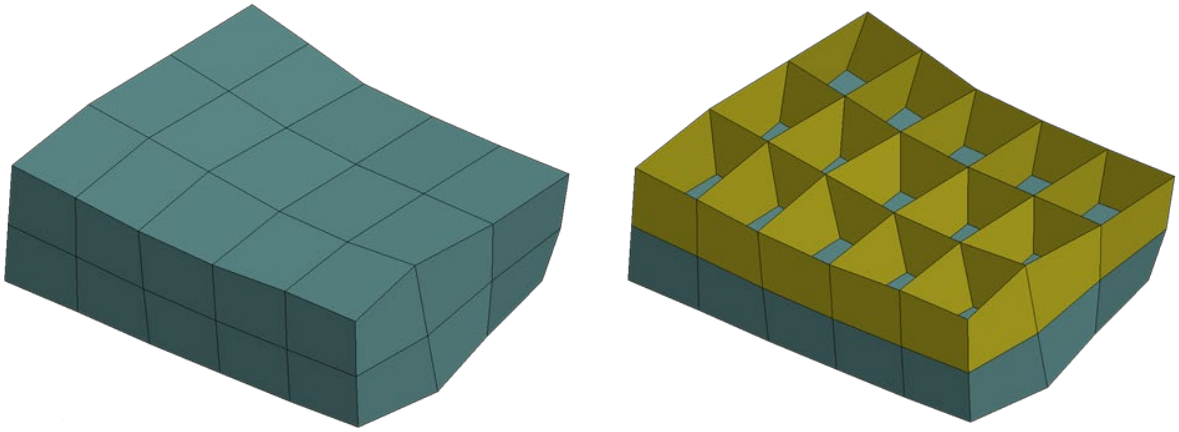

Figure 145. Countermeasure for GHBMC M50-OS abdomen negative volume.

8.2.3 GHBMC internal biofidelity issues

In our observation, the GHBMC M50-OS model lacks a continuity definition (beyond normal compressive contact) between the superficial flesh, the skeleton, and the underlying organs. As a result, the flesh is able to slide across the skeleton easily (**Figure 147** and **Figure 149**). This issue was not noticeable in simulations in a traditional upright seated posture in a frontal impact, as the restraint systems tended to apply compressive forces to the flesh pressing it into the skeleton. The effect is certainly noticeable in non-traditional postures, or in impact directions other than frontal. For example, in frontal impact simulations with the reclined posture, the flesh around the pelvis underwent a substantial shear force as the pelvis slides under the lap belt, and slides over the seat cushion. This shearing action results in the flesh sliding over and around the pelvis. This likely contributes to the resistance to submarining and potentially the restraining forces applied to the pelvis during submarining. Similarly, in the rear impact simulations the flesh on the posterior surface of the pelvis tended to slide over the pelvis. In other words, the friction between the seat and the flesh was greater than the friction between the flesh and the pelvis. As with the submarining example, this will affect how shear-type forces (friction, etc.) are transferred from the seat to the flesh to the skeleton, thus affecting overall body kinematics.

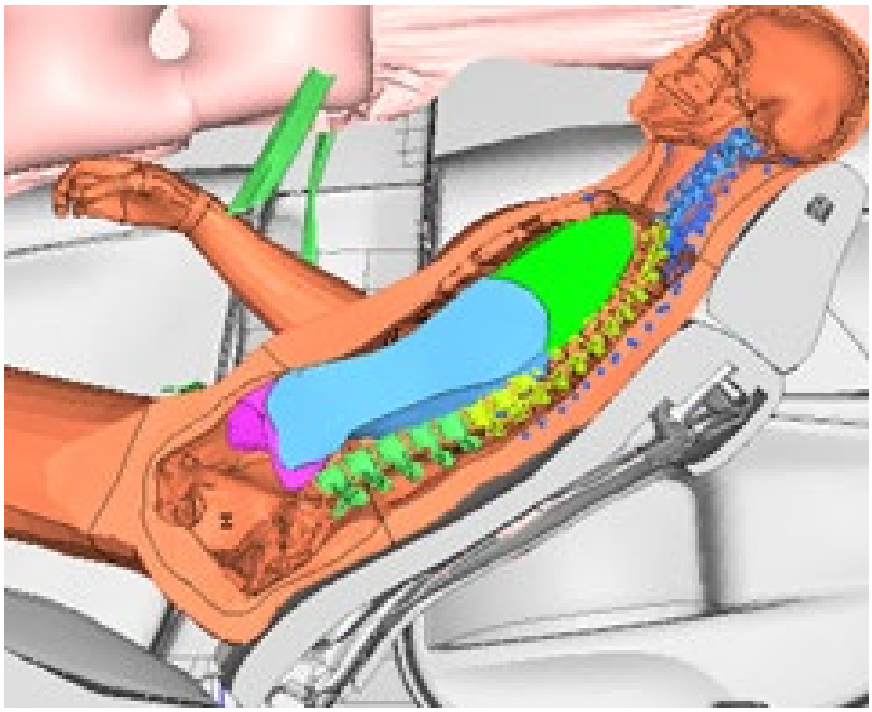

Figure 146. Unrealistic internal organs' connections.

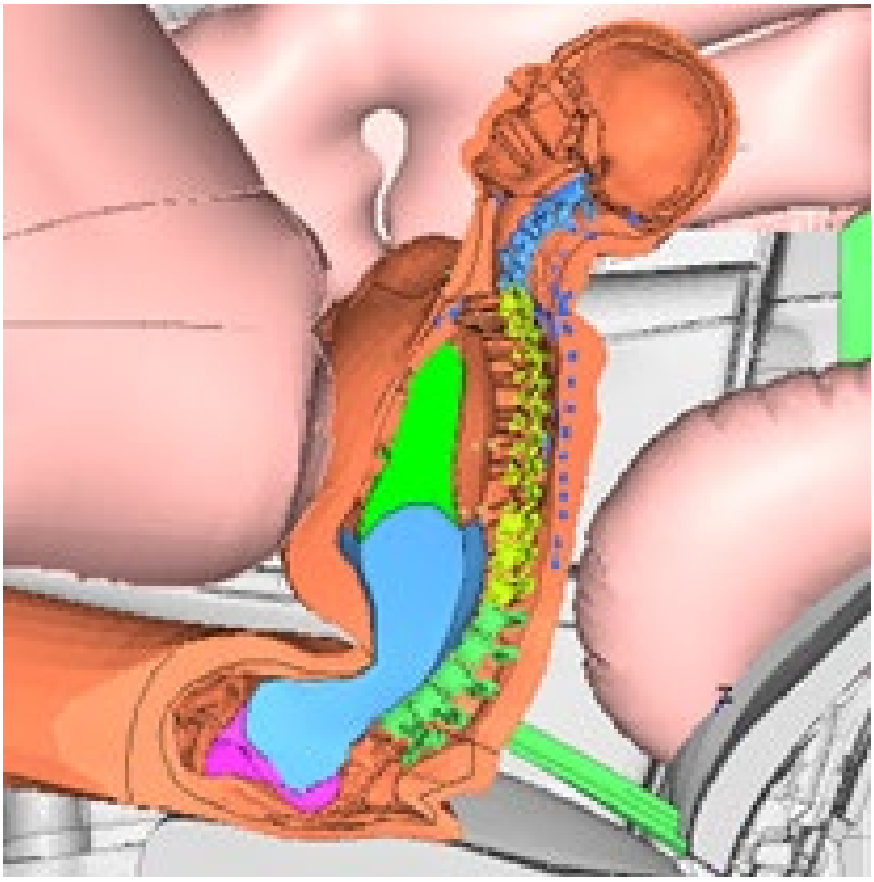

Figure 147. Unrealistic flesh sliding off of the pelvis.

It is currently unknown, however, how to best model the interaction between the flesh and the skeleton. In reality, superficial tissue exhibits a relatively low shear stiffness. Thus, a direct tie between the flesh material and the skeleton may result in a response that is too stiff. However, allowing the flesh to slide freely over the skeleton is likely too soft. The true response likely lies somewhere between. Given the potential importance in recreating the occurrence of submarining, we recommend that future work should include generating new biofidelity reference data on the multi-directional material behavior of the flesh, as well as exploring methods to implement that behavior in the GHBMC model.

In addition, there does not appear to be any continuity constraints (aside from compressive contact) between the skeleton and the internal organs (**Figure 148**). As with the shearing discussion above, consequences of this are not as apparent in frontal simulations with an upright occupant since the restraint systems apply an early and direct compression to the thorax. In other condition types that display less compression and more complex inertial motions, however, the internal organs can be observed to move relative to each other within the chest cavity, causing large voids to form. We do not believe these voids to be biofidelic — in reality you have an array of connective tissues that constrain the organs to each other and to the skeleton. For organs with less connective tissue constraint (e.g., the lungs) the shape and position of the organ within the chest cavity is maintained by pressure differential mechanisms facilitated by a series of impermeable membranes (e.g., the pleura surrounding the lungs and lining the internal chest

cavity). Under static circumstances, these types of voids cannot form between the organs without some sort of disruption of these membranes (e.g., via a pneumothorax). It is theoretically possible for some voids to develop between the organs during dynamic loading, however such voids would indicate the presence of negative pressure or cavitation. The work required to achieve negative pressure or cavitation is not included in the mechanics of the FE model - so even if this phenomenon does occur to some limited extent in real life, they are not being modeled properly in the GHBMC.

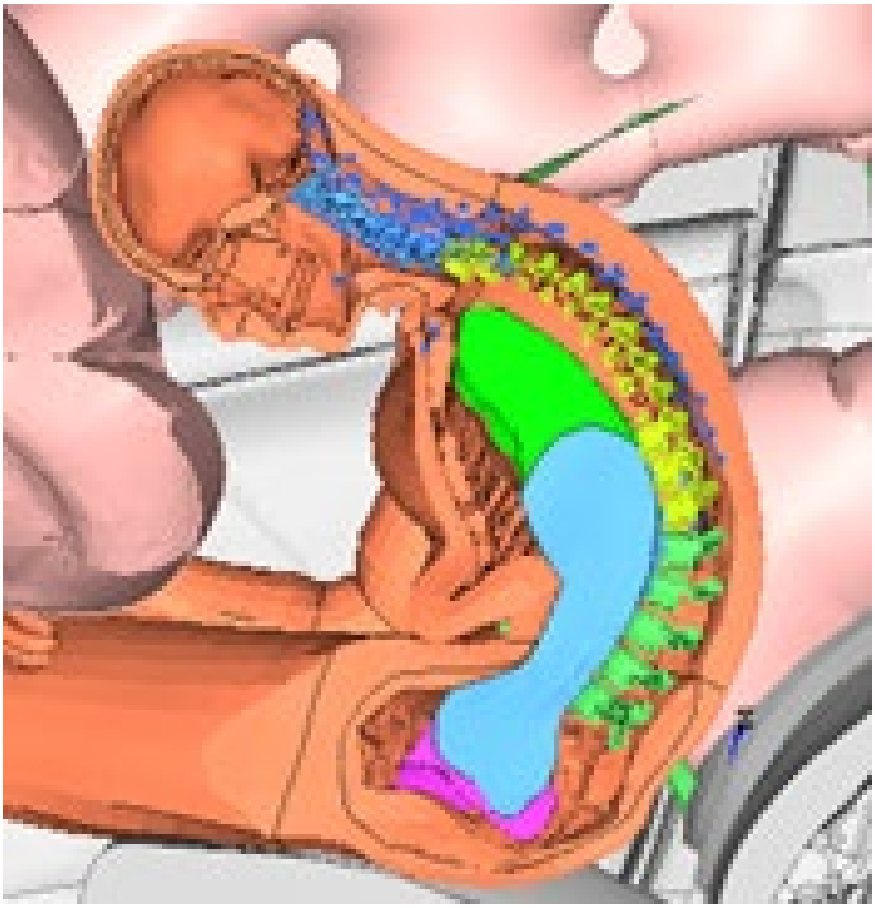

Figure 148. Failure to maintain internal cavity's volume.

It is currently unknown the extent to which these internal cavity issues influence the performance of the models or their utility for injury prediction. At a minimum, the lack of continuity modeling suggests that the organs are not being loaded in a realistic manner, limiting our ability to use local organ-specific measures (strain, etc.) to predict injury risk in those organs. The injury risk predicted in other structures (e.g., the ribs) is likely less affected.

8.3 GHBMC M50-O Model

8.3.1 GHBMC M50-O cannot settle

The spine of the GHBMC-M50-O is too stiff to allow natural gravity settling into reclined positions similar to M50-OS. Additionally, the M50-O thorax was observed to be stiffer than the M50-OS during the gravity settling phase of the seating process. The upright (25°) seated M50-O was not able to be directly positioned on the seatback without pulling back to the seatback (**Figure 36**). Future work should include exploring other options for position in pre-processing, potentially using tools such as PIPER.

8.3.2 GHBMC M50-O is time-consuming to get into the correct position

Compared to settling the M50-OS, the M50-O requires an extra 6 simulations using the cable discrete beams to pull components of the M50-O in place to match M50-OS. This process took around 120 hours for each seating configuration (**Figure 40**).

8.3.3 GHBMC M50-O instability issues

Several modeling artifacts were observed with the GHBMC M50-O model. For example, in some cases, the neck muscle deforms substantially during the simulation during contact with the shoulder belt (**Figure 64** and **Figure 78**). These types of artifacts should be addressed in future refinements of the model.

8.4 Occupant Model Comparisons

Though it was not the intention of this study, some preliminary observations may be made in comparing the restraint interactions and kinematics of the occupant models. In particular, the GHBMC M50-OS tended to exhibit substantially different motions of the pelvis and lower body compared to the THOR FE model. The GHBMC model exhibited substantially greater forward pelvis motion with the lap belt slipping up and over the pelvis in most (if not all) frontal impact simulations. This was especially apparent in the reclined posture. The GHBMC also tended to exhibit a backwards rotation of the pelvis as it slid underneath of the lap belt. This backwards rotation of the pelvis tended to be accompanied by a forward flexion of the lumbar spine. In contrast, the THOR model tended to exhibit less forward motion of the pelvis (despite having a greater initial distance between the knees and the IP), and greater apparent engagement between the seat structure and the underside of the pelvis and thighs. The THOR also tended to exhibit pelvis rotation in the opposite direction compared to the GHBMC — instead of rotation backwards during submarining, the THOR pelvis tended to pitch forward as the underside engaged with the seat structure and the inertia of the upper body carried the lumbar spine forward. The lumbar spine of the THOR did exhibit some forward flexion, but it is currently unclear how that flexion compares to the GHBMC results (in magnitude and stiffness) — additional work could include further analysis of these model results to compare spinal kinematics, and/or a sensitivity study to determine the effects of local spinal stiffness on kinematics and restraint interaction.

Unfortunately, to our knowledge there does not currently exist a reference biofidelity response dataset for submarining occupants in semi-reclined seating postures. Thus, it is difficult to assess which model (if either) is more representative of the pelvis motions and submarining responses expected to occur in the field. As pelvis motion, lumbar spine flexion, and seat interaction are

likely to have an effect on whole-body kinematics and potential countermeasure design, we recommend that future work include generation of bio-fidelity reference data (through PMHS tests or similar) for the following:

- Whole-body response in semi-reclined and reclined positions
- Lumbar spine functional stiffness under combined flexion and compression
- Material response of superficial tissues under combined compression and shear

9 References

Battaglia, S., Kietlinski, K., Unger, M., van der Made, R., & Bours, R. (2013, May 27–30). Occupant behavior during a one-lane change maneuver resulting from autonomous emergency steering (Paper 13-0383). *Proceedings of the 23rd International Technical Conference on the Enhanced Safety of Vehicles* (ESV), Seoul, Korea.

Crandall, J. (2013, September). *Injury Criteria Development: THOR Metric SD–3 Shoulder Advanced Frontal Crash Test Dummy* (NHTSA Biomechanics Database, Report b11117–1). National Highway Traffic Safety Administration.

Dissanaike, S., Kaufman, R., Mack, CD., Mock, C., & Bulger, E. (2008). The effect of reclined seats on mortality in motor vehicle collisions. *Journal of Trauma, 64*(3): 614–619.

Fagnant, D., & Kockelman, K. M. (2013). *Preparing a nation for autonomous vehicles: Opportunities, barriers and policy recommendations.* Eno Center for Transportation.

Forman, J., Michaelson, J., Kent, R., Kuppa, S., & Bostrom, O. (2008, October). Occupant restraint in the rear seat: ATD responses to standard and pre-tensioning, force-limiting belt restraints. *Annals of Advances in Automotive Medicine, 52*:141–54.

Hayes, B. (2011). Leave the Driving to It. *American Scientist, 99*: 362–366.

Kuppa, S., Wang, J., Haffner, M., & Eppinger, R. (2001, June 4–7). *Lower extremity injuries and associated injury criteria* (Paper No. 457). 17th International Technical Conference for the Enhanced Safety of Vehicles, Amsterdam.

Levinson, D. (2015). Climbing Mount Next: The effects of autonomous vehicles on society. *Minnesota Journal of Law, Science & Technology, 16*(2): 787–810.

Litman, T. (2016, January 11–15). *Autonomous vehicle implementation predictions: Implications for transport planning*. Transportation Research Board 94th Annual Meeting, Washington, DC.

Martin, P. G., & Scarboro, M. (2011, June 13–16). *THOR–NT: Hip Injury Potential in Narrow Offset and Oblique Frontal Crashes* (Paper No. 11-0234). 22nd International Technical Conference for the Enhanced Safety of Vehicles, Washington, DC.

Panzer, M.B., Giudice, J.S., & Parent D. (2015, January). THOR 50th Male Finite Element Model User Manual: Model Version 2.1 for LS-Dyna. Petitjean, A., Trosseille, X., Petit, P., Irwin, A., Hassan, J., & Praxl, N. (2009). Injury risk curves for the WorldSID 50th percentile male dummy. *Stapp Car Crash Journal, 53*: 443–476.

Reichert, R., Mohan, P., Marzougui, D., Kan, C., & Brown, D. (2016, April 12–14). *Validation of a Toyota Camry finite element model for multiple impact configurations* (SAE Technical Paper 2016-01-1534). Detroit, MI. https://doi.org/10.4271/2016-01-1534.

Saunders, J., Craig, M. J., & Suway, J. (2011, June 13–16). *NHTSA's test procedure evaluations for small overlap/oblique crashes* (Paper No. 11-0343). 22nd International Technical Conference on the Enhanced Safety of Vehicles, Washington, DC.

Saunders, J., Parent, D., & Ames, E. (2015, June 8–11). *NHTSA oblique crash test results: Vehicle performance and occupant injury risk assessment in vehicles with small overlap countermeasures* (Paper No. 15–0108). 24th International Technical Conference for the Enhanced Safety of Vehicles, Gothenburg, Sweden.

Sivak, M., & Schoettle, B. (2015, January). *Road safety with self-driving vehicles: General limitations and road sharing with conventional vehicles* (Report No. UMTRI-2015-2). University of Michigan Transportation Research Institute.

Versace, J. (1971, November 17–19). A review of the severity index. *Proceedings of the 15th Stapp Car Crash Conference,* Coronado, CA.

Zhang, Q., Kindig, M., Li, Z., Crandall, J. R., &Kerrigan, J. R. (2014). Development of structural and material clavicle response corridors under axial compression and three-point bending loading for clavicle finite element model validation. *Journal of Biomechanics, 47*, no. 11: 2563–2570.

10 Appendix

10.1 Post-Processing Script Manual

10.1.1 Post-processing process

For details, “Post-Processing Script Manual.ppt” could be referenced.

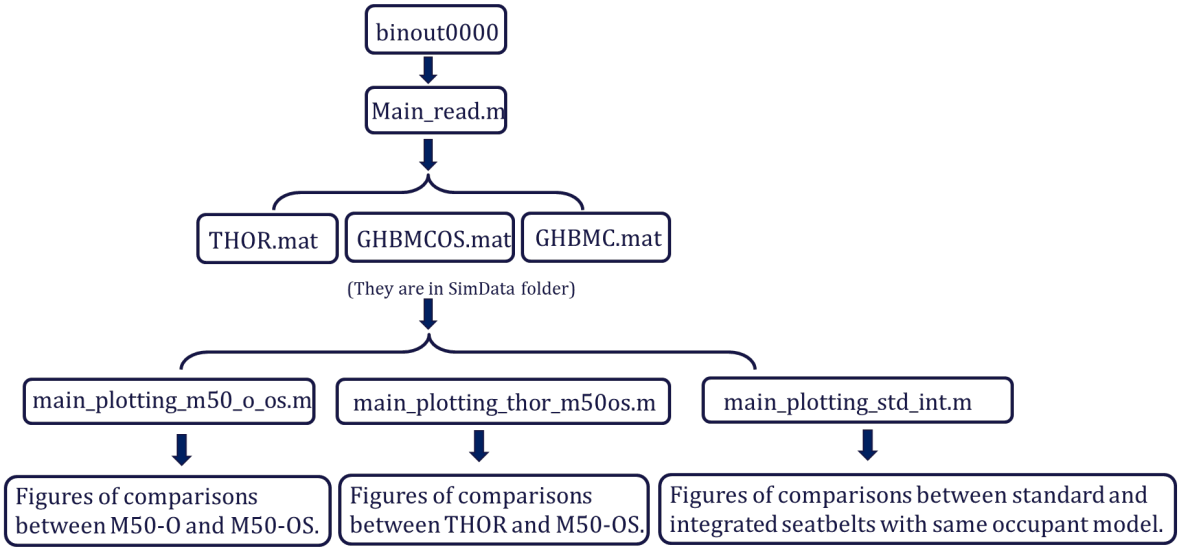

Figure149. Post-processing structure.

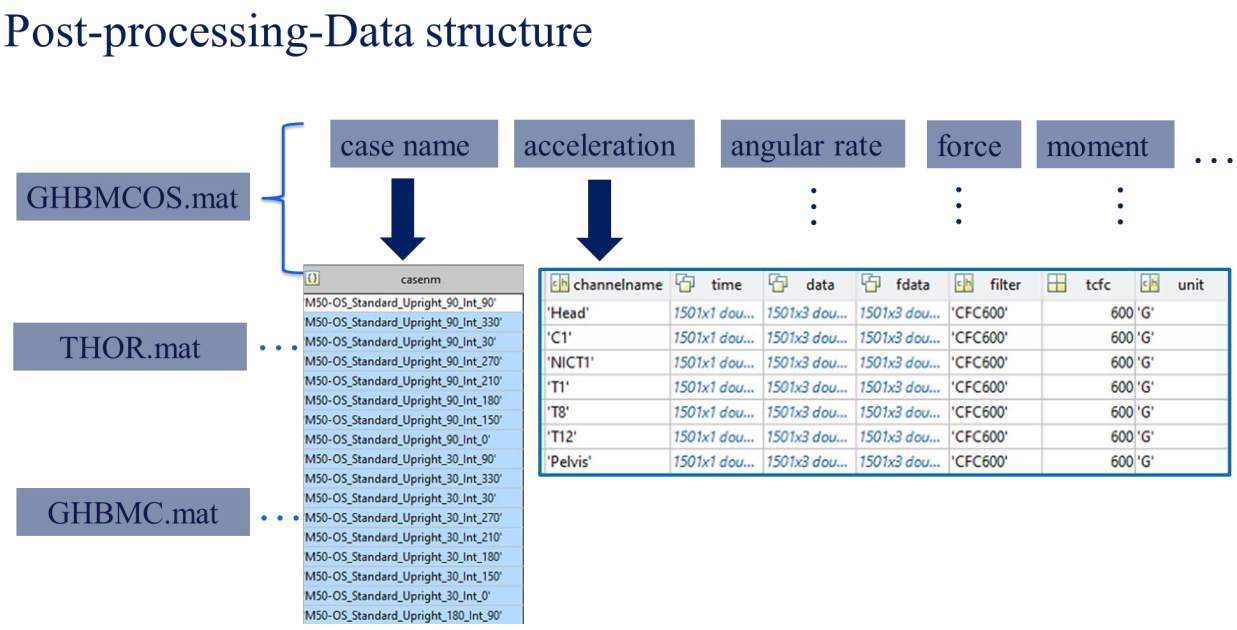

Figure 150. Data structure.

DOT HS 812 904
November 2020 (revised)

U.S. Department
of Transportation

**National Highway
Traffic Safety
Administration**

14611-110520-v5a